Eur. Phys. J. C (2024) 84:955
https://doi.org/10.1140/epjc/s10052-024-13077-x

THE EUROPEAN PHYSICAL JOURNAL C

Regular Article - Experimental Physics

Measurement of the background in the CMS muon detector in pp-collisions at $\sqrt{s} = 13$ TeV

CMS Muon Group*

CERN, 1211 Geneva 23, Switzerland

Received: 19 April 2024 / Accepted: 1 July 2024 / Published online: 27 September 2024

Abstract The CMS detector, including its muon system, has been operating at the CERN LHC in increasingly challenging conditions for about 15 years. The muon detector was designed to provide excellent triggering and track reconstruction for muons produced in proton–proton collisons at an instantaneous luminosity ($\mathcal{L}$) of $1 \times 10^{34}\,\mathrm{cm}^{-2}\mathrm{s}^{-1}$. During the Run 2 data-taking period (2015–2018), the LHC achieved an instantaneous luminosity of twice its design value, resulting in larger background rates and making the efficient detection of muons more difficult. While some backgrounds result from natural radioactivity, cosmic rays, and interactions of the circulating protons with residual gas in the beam pipe, the dominant source of background hits in the muon system arises from proton–proton interactions themselves. Charged hadrons leaving the calorimeters produce energy deposits in the muon chambers. In addition, high-energy particles interacting in the hadron calorimeter and forward shielding elements generate thermal neutrons, which leak out of the calorimeter and shielding structures, filling the CMS cavern. We describe the method used to measure the background rates in the various muon subsystems. These rates, in conjunction with simulations, can be used to estimate the expected backgrounds in the High-Luminosity LHC. This machine will run for at least 10 years starting in 2029 reaching an instantaneous luminosity of $\mathcal{L} = 5 \times 10^{34}\,\mathrm{cm}^{-2}\,\mathrm{s}^{-1}$ and increasing ultimately to $\mathcal{L} = 7.5 \times 10^{34}\,\mathrm{cm}^{-2}\,\mathrm{s}^{-1}$. These background estimates have been a key ingredient for the planning and design of the muon detector upgrade.

1 Introduction

The Compact Muon Solenoid (CMS) [1] is a general purpose experiment to explore the physics of the TeV scale in proton–proton (pp) collisions provided by the CERN Large Hadron Collider (LHC). The detection, triggering, reconstruction and identification of muons is essential to the CMS physics program. Previously published studies of the performance of the CMS muon detector [2] and muon reconstruction [3] were based on pp-collision data at centre-of-mass energy $\sqrt{s} = 7$ TeV during LHC Run 1 (2010–2012). To deal with higher collision energy and luminosity during LHC Run 2 (2015–2018), improvements were made to the muon detector during the long shutdown period (LS1) between Run 1 and Run 2 [4]. The reconstruction of high-momentum muons was studied [5] and trigger algorithms were refined for running at high instantaneous luminosity [6]. These improvements ensured good muon detection, triggering and reconstruction in the higher background environment of Run 2, both in pp and in heavy-ion collisions [7]. Further enhancements of the muon system for Run 3 are documented in [8].

The present paper describes the various methods used to measure these backgrounds in the muon detector, and reports the observed hit and particle rates. It is based on data collected by CMS during pp-collisions at $\sqrt{s} = 13$ TeV in 2018, with an instantaneous luminosity ($\mathcal{L}$) provided by the LHC up to $2.2 \times 10^{34}\,\mathrm{cm}^{-2}\mathrm{s}^{-1}$. The measured backgrounds are reported at a reference $\mathcal{L} = 10^{34}\,\mathrm{cm}^{-2}\,\mathrm{s}^{-1}$. A thorough understanding of these rates can provide the basis for predicting expected rates in the CMS muon detector at the future High-Luminosity LHC (HL-LHC) operation, where the instantaneous luminosity will reach ultimately $\mathcal{L} = 7.5 \times 10^{34}\,\mathrm{cm}^{-2}\,\mathrm{s}^{-1}$, corresponding to 200 overlapping pp-collisions.

A description of the detectors forming the CMS muon detector is given in Sect. 2, considering in particular their principles of detection and operation. The operation of the LHC during Run 2 is briefly described in Sect. 3. Section 4 discusses the origin and characteristics of the background produced by the pp-collisions. Section 5 presents the response of the various detectors, introduces the definitions of the particle rate and the single hit rate that will be used when specifying background measurements, and illustrates the dependence of the background on the LHC instantaneous luminosity and configuration. The hit rates in the muon detector are presented in Sect. 6, while Sect. 7 analyses the dependence of the rates on the specific LHC fill scheme, allow-

* e-mail: piet.verwilligen@cern.ch (corresponding author)

ing the separation of promptly-induced backgrounds from long-lived backgrounds. The results and findings are summarised in Sect. 8, while Appendix A provides more information about the simulated geometry of the CMS experiment and experimental cavern.

2 The CMS experiment and the muon detector

2.1 The CMS experiment

The CMS detector has a cylindrical geometry with azimuthal (ϕ) symmetry with respect to the beamline and features a superconducting solenoid of 6 m internal diameter, providing a magnetic field of 3.8 T. Within the solenoid volume, a silicon pixel and strip tracker measure the momentum of charged particles in the pseudorapidity range $|\eta| < 2.5$, while a lead tungstate crystal electromangetic calorimeter (ECAL), and a brass and scintillator hadron calorimeter (HCAL) measure the energy of photons, electrons and neutral and charged hadrons up to $|\eta| < 3.0$. Forward calorimeters (HF), made of steel and quartz fibers, extend the pseudorapidity coverage provided by the barrel and endcap detectors up to $|\eta| < 5.2$. The calorimeters and solenoid constitute ≥ 10 nuclear interaction lengths (λ_L) for particles created at the interaction point (IP) to reach the muon detector. Muons are measured in gas-ionization detectors embedded in the steel flux-return yoke outside the solenoid in a pseudorapidity range $|\eta| < 2.4$. The steel yoke serves as hadron absorber. It confines the magnetic field and aids the identification of muons.

Events of interest are selected using a two-tiered trigger system. The first level (L1), composed of custom hardware processors, uses information from the calorimeters and muon detectors to select events at a rate of around 100 kHz within a fixed latency of about 4 μs [9]. The second level, known as the high-level trigger (HLT), consists of a farm of processors running a version of the full event reconstruction software optimised for fast processing, and reduces the event rate to around 1 kHz before data storage [10]. Several subdetectors, such as Pixel detector and HF are used for the luminosity measurement. Furthermore the Pixel Luminosity Telescope (PLT) and the Fast Beam Conditions Monitor (BCM1F) are dedicated systems that use a separate data acquisition system, such that the luminosity measurements are obtained independently of the current operating status of CMS [11]. The Beam Pick-up and Timing for eXperiments (BPTX) detectors [12], located at $z = \pm 175$ m of the interaction point, register the presence of a proton bunch and are used to collect an unbiased dataset of pp-collision events (*"Zero Bias"* events), while HF is used to collect a set of pp-collision events with minimal activity in CMS (*"Minimum Bias"* events). A more detailed description of the CMS detector, together with a definition of the coordinate system used and the relevant kinematic variables, can be found in Ref. [1].

2.2 Muon detector

The CMS muon detector is made up of three types of gas ionization chambers: drift tube chambers (DTs), cathode strip chambers (CSCs) and resistive plate chambers (RPCs); a detailed description of these chambers can be found in reference Ref. [2]. A schematic diagram of the CMS detector where the various subdetectors are highlighted is shown in Fig. 1.

A minimum ionising particle passing through the gas layer of a detector ionises the gas along its trajectory, liberating electrons. Signals are picked up after Townsend multiplication of these electrons in an intense electric field, either close to the wires for DTs and CSCs, or in the entire thin gas gap for RPCs. DT chambers consist of drift tube cells where the position of a particle is determined by measuring the drift time of the ionisation electrons. CSCs are multi-wire proportional chambers with finely segmented cathodes that yield a precise measurement in the bending plane (R-ϕ). RPCs are double-gap chambers with resistive electrodes that are operated in avalanche mode and provide a fast signal used for triggering. DTs are installed in the barrel ($|\eta| < 1.2$) where backgrounds are small and the magnetic field is low since it is mostly concentrated in the steel yoke. CSCs are installed in the endcap ($0.9 < |\eta| < 2.4$) where both magnetic field and backgrounds are higher. RPCs are installed both in the barrel as in the endcap and cover $|\eta| < 1.9$.

In the barrel, a set of chambers at the same radius R from the IP is called a station. There are four DT and four RPC stations in the barrel, named MB1 to MB4 (DT) and RB1-RB4 (RPC). DT and RPC stations are arranged in 5 *wheels* along the z coordinate, named W-2 to W+2, and are subdivided in 12 ϕ sectors, named S01 to S12. The location of a chamber is fully given by information on the wheel, sector and station: e.g. W-2/S01/MB1 or W+2/S12/RB4. Each DT chamber consists of three *superlayers* that are each made of four staggered layers of drift tube cells. Two superlayers measure precisely the bending of the muon trajectory in the $R-\phi$ plane, while one superlayer measures the position in the longitudinal plane ($R-\theta$). The chambers in the 4th station (MB4) have only two superlayers and measures the muon only in the bending plane ($R-\phi$). In the barrel, the RPCs are attached to the DT chamber. In the innermost RPC stations (RB1 and RB2), two RPC chambers are installed, one on each side of the DT chamber, named RB$x$in and RB$x$out ($x = 1, 2$). In the outermost RPC stations (RB3 and RB4), only a single RPC chamber is installed on the innermost surface of the DT chamber, facing the IP. An RPC chamber consists of a double gap structure with a central strip plane that picks up signals created in each of the gaps. RPCs have

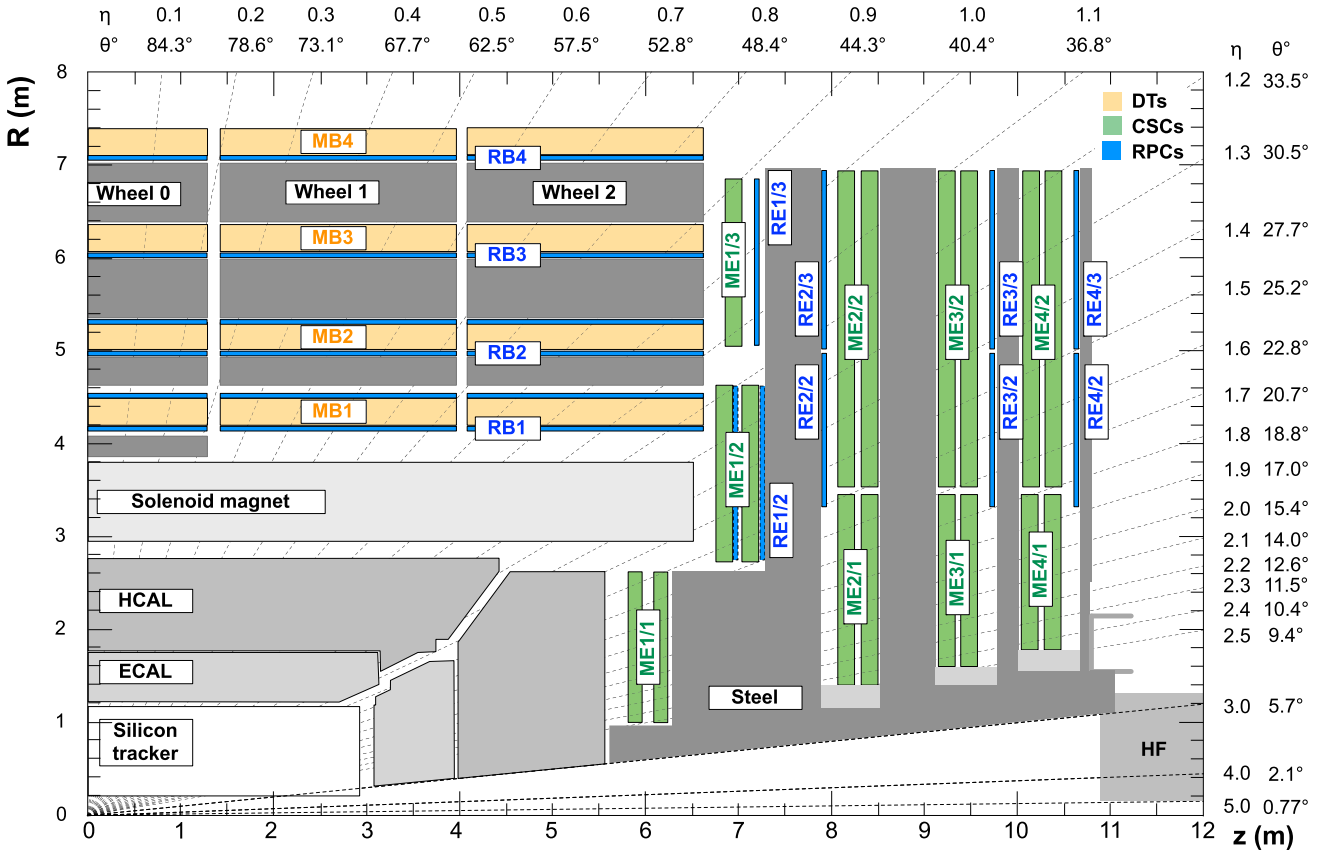

Fig. 1 An $R - z$ cross section of a quadrant of the CMS detector with the beam parallel to the z axis and the IP at the lower left corner. The location of the various muon stations and the steel flux-return yoke are shown: DTs are labeled MB (Muon Barrel), CSCs are labeled ME (Muon Endcap), RPCs are labeled RB (RPC Barrel) and RE (RPC Endcap)

strips parallel to the beamline to measure the muon in the bending plane ($R - \phi$); the strip plane is divided in two or three so-called η-partitions.

In the endcap, a set of chambers at the same distance z from the IP is called a station. There are four CSC and four RPC stations in each endcap, named ME1-ME4 (CSC) and RE1-RE4 (RPC). The first station consists of three concentric rings of CSC chambers ME1/1, ME1/2 and ME1/3, and two concentric rings of RPC chambers RE1/2 and RE1/3. The inner ring RPC chamber was descoped as the particle rates were estimated to be too high for the RPC technology at the time of construction. The second to fourth station consists each of two rings of CSC chambers: MEx/1 and MEx/2, where $x = 2, 3, 4$, and two rings of RPC chambers: REx/2 and REx/3, with the inner RPC rings (REx/1) descoped. For the *Phase 2* upgrade of the muon detector [13], Gas Electron Multipliers (GEMs) and improved RPCs (iRPCs) will be installed in respectively the first two stations and the last two stations, to deal with the high particle rates expected at the HL-LHC. A CSC chamber consists of six independent sensitive layers with staggered cathode strips in adjacent layers. Each layer measures the position of the muon in two coordinates: radially oriented cathode strips measure the bending angle in the $R - \phi$ plane, while anode wires, grouped in *wire groups* (WG) provide a coarse measurement in R. RPC chambers consist of double gaps that sandwhich a strip plane that picks up signals from both gas gaps and have strips oriented radially. The RPC strip plane is divided in three so-called η-partitions.

The flux-return yoke is composed of 5 barrel wheels and 8 endcap disks, with a weight of approximately 10,000 t. Each of the barrel wheels consist of three concentric steel rings that separate the muon stations and have a thickness of respectively 30 cm, 60 cm, and 60 cm corresponding to roughly 2, 4, and 4 interaction lengths. In the endcap the first and the second disk have a thickness of 60 cm ($\sim 4\,\lambda_L$), while the third disk has a thickness of 23.5 cm ($\sim 1.5\,\lambda_L$). During LS 1 (2013–2014), a fourth disk was installed to shield the outermost endcap stations ME4 and RE4 from radiation background in the cavern. As this fourth disk is not needed for magnetic flux return, it was constructed as a 12.5 cm hollow steel casing filled with borated concrete (2.5 cm steel walls

and 7.5 cm concrete), resulting in a total weight of ∼6.8 t each [14].

2.3 The experimental cavern, forward environment and beampipe

The CMS experiment is installed in a 53 m long, 27 m wide, and 24 m high experimental cavern with concrete walls, located 100 m underground, and connected to the surface through two shafts. To protect the beam focusing quadrupoles of LHC from high-energetic collision debris, a 3.2 t and 2.1 m long copper collimator (Target Absorber Secondaries, TAS [15]) with 18 mm inner radius and 25 cm outer radius is installed at both sides of the IP at a distance of $z = 19$ m. As the TAS is a major source of background in the experimental cavern, it is properly shielded with steel and borated concrete, to reduce the radiation by three orders of magnitude. Figure 2 shows the layout of the shielding in the forward region. Upstream of the HF there is a 20 cm thick shielding of borated polyethylene to supress neutron albedo from the HF back into the $\eta \leq 3$ cone. The HF is covered by 30 cm of steel, followed by 30 cm of borated concrete. At the back of the HF there is a borated polyethylene covered steel plug to protect the HF electronics and to reduce the leakage of neutrons into the cavern. The TAS collimator is embedded into a steel cone and surrounded by the rotating forward shielding which extends from the back of the HF to the blockhouse in the cavern wall. This shielding can be opened to allow the movement of the endcap yoke elements to provide access to the various detectors installed in the barrel. The forward shielding consists of an inner steel shell followed by borated concrete. During the 2016–2017 end-of-year technical stop, additional shielding was installed to cover cracks or openings in the forward shielding and the shielding of the HF: the opening under the blockhouse and vertical gaps in the forward shielding. The beampipe spans 18 m from both sides of the IP up to the vacuum pumps in front of the TAS and consists of a central section of 6.2 m and four sections on each end. The central section is made of a 0.8 mm thick beryllium cylinder with 45 mm outer diameter, followed by a stainless steel conical endcap section of 7.2 m that runs under the endcap yoke. Further elements are pumping stations located behind the HF and in front of the TAS collimator.

3 LHC operation during Run 2

The LHC operated during Run 2 (2015–2018) at 6.5 TeV beam energy with a peak luminosity that exceeded the design parameters by a factor of two. The collision rate is given by $dN/dt = \sigma\mathcal{L}$ with σ the pp-collisions cross-section and $\mathcal{L}$ the instantaneous luminosity, which can be expressed in function of machine and beam parameters:

$$\mathcal{L} = \frac{kN^2 f_{\text{rev}}\gamma}{4\pi\beta^*\varepsilon}F, \tag{1}$$

where k is the number of colliding proton bunches, N is the number of protons in each bunch, $f_{\text{rev}} = 11{,}245.5$ Hz is the LHC beam revolution frequency, $\gamma \approx 6927$ is the Lorentz factor for 6.5 TeV protons, β^* is the beta function at the interaction point, ε is the normalised emittance and F (∼0.60) is a reduction factor due to the crossing angle (θ_c). Table 1 summarises the beam parameters [16].

The LHC radio-frequency system divides the beam orbit into 35640 buckets of 2.495 ns each. One RF bucket out of ten nominally hosts a proton bunch, resulting in 3564 available buckets, each spaced 25 ns apart. As the bunch crossings (BX) are expected to happen every 25 ns, in the filling scheme those buckets are enumerated with the relevant BX number. Since (as shown in the table) each bucket is filled with O 10^{11} protons, a number of individual pp-collisions happen at each bunch crossing: this number is called pileup. During Run 1 (2010–2012), protons were collided with 50 ns spacing to reduce instabilities due to beam induced electron-clouds, while in Run 2 protons were injected and collided with 25 ns bunch spacing. Given the additional challenges for the LHC to operate in this regime, 2015 was a year mostly devoted to preparing the machine for full luminosity production in 2016–2018 [16]. In 2016 the Batch Compression Merging and Splitting (BCMS) scheme in a combination with a reduction of the half crossing angle from 185 to 140 μrad [17] was commissioned for high brightness beams, resulting in record peak luminosity of $1.4 \times 10^{34}\,\text{cm}^{-2}\text{s}^{-1}$.

In 2017 abnormal sudden beam losses in the LHC were observed and a different injection scheme, '8b4e' (8 bunches with 25 ns spacing, followed by 4 empty bunch positions), was adopted to suppress electron-cloud production [16,18]. A high brightness version '8b4e-BCS' (Bunch Compression and Splitting) was developed and used during fall 2017 for luminosity production. The β^* was reduced to 30 cm, leading to a peak instantaneous luminosity of $2.06 \times 10^{34}\,\text{cm}^{-2}\text{s}^{-1}$, resulting in nearly 80 overlapping pp-collisions. To reduce the mean pileup to ∼55, the luminosity was levelled by separating the beams to $1.5 \times 10^{34}\,\text{cm}^{-2}\text{s}^{-1}$ at the beginning of the fill. In 2018 the problem with the sudden beam losses was improved, and adopting the BCMS fill scheme, a peak instantaneous luminosity of $2 \times 10^{34}\,\text{cm}^{-2}\text{s}^{-1}$ was reached, running at a higher number of colliding bunches with a lower pile-up per bunch.

Figure 3 shows the bunch structure of an injection scheme with 1866 colliding bunches (8b4e-BCS) used in 2017 (top) and an injection scheme with 2544 colliding bunches (BCMS) adopted in 2018 (bottom). This structure reflects the design of the injection of proton bunches from the Proton Synchrotron (PS) in the Super Proton Synchrotron (SPS),

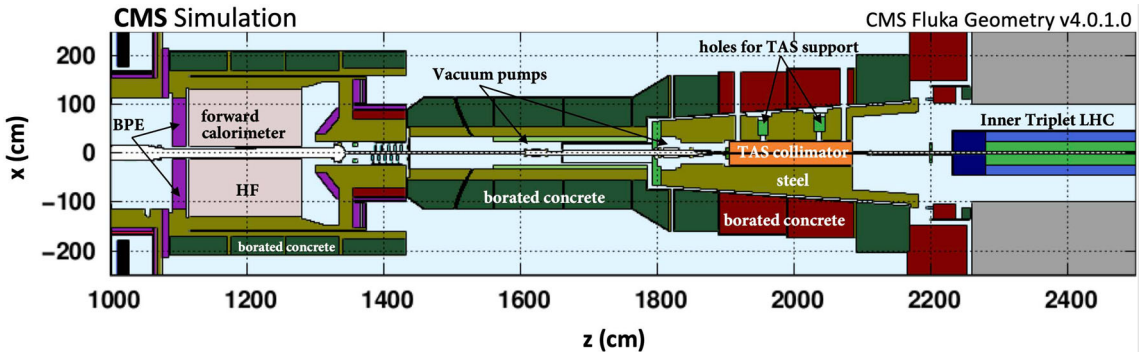

Fig. 2 Side view of the beampipe and the machine-detector interface, illustrating the steel and borated concrete shielding around HF, and the rotating shielding around the TAS

Table 1 Overview of LHC Machine and Beam parameters during Run 2, from Ref. [16]

Parameter beam type	Design std	2015 std	2016 BCMS	2017 8b4e-BCS	2018 BCMS
Total number of bunches	2808	2244	2076	1868	2556
Number of colliding bunches (k)	2808	2232	2064	1866	2544
Protons per bunch (N) [10^{11}]	1.15	1.15	1.20	1.25	1.10
Normalised emittance (ε) [μm·rad]	3.75	3.5	3.5/2.1	1.8	2
Value of β-function at IP (β^*) [m]	0.55	0.8	0.4	0.3	0.3/0.25
Half crossing angle ($\theta_c/2$) [μrad]	142.5	145	185/140	150/120	160/130
Peak luminosity ($\mathcal{L}$) [$10^{34}\,\mathrm{cm}^{-2}\mathrm{s}^{-1}$]	1	0.55	1.4	2.06/1.50	2.2
Peak pileup (PU)	20	15	20/35	80/60	60
Integrated luminosity [fb^{-1}]		4.2	39.7	50.6	66
Time in stable beams [%]		33%	49%	49%	49%

where the PS beam has 84 available bunch slots; only 32 or 48 were used up to now.[1] The 7 bunch crossings (BX) gap between batches of 32–48 bunches is required by the rise-time of the SPS injection kicker magnet. The SPS can contain up to 11 injections from PS, and the 31 BX gap between three or four batches of 32–48 bunches is due to the rise-time of the LHC injection kicker magnet. At the end of the fill, long gaps of 120–150 BX ($\geq 3\,\mu$s) allows for the LHC beamdump kicker magnet rise-time.

To reduce the average pile-up to a condition that ensured good event reconstruction, at the end of 2017 running, the peak luminosity was leveled by separating the two beams at the interaction point, with a negligible loss of integrated luminosity. Figure 4 shows the rate of pile-up events during data taking in 2017, with the leveled 8b4e-BCS scheme and in 2018 without leveling adopting the BCMS 25 ns fill scheme. Note the very high pile-up (78 overlapping pp-collisions) at the very beginning of Fill 6298 shown in Fig. 4 (top) before the beams were separated to level to a fixed instantaneous luminosity of $1.5 \times 10^{34}\,\mathrm{cm}^{-2}\mathrm{s}^{-1}$. The specific filling scheme, the fraction and position of empty buckets in the LHC orbit, and the amount of protons in each bucket lead to different instantaneous luminosity per bunch, and, as a consequence, to different background conditions that must be considered when evaluating the hit rate in the detectors.

The curve of the instantaneous luminosity as a function of the time during a fill, shows an exponential decay, which is caused by the beam losses. These losses are either due to burn-up (reduction of protons in the bunches due to collisions) or to emittance losses (protons leaving the beam envelope and cleaned by the LHC collimation system) [19,20]. During Run 2, CMS decided to monitor the calibration of the luminosity detectors through fast luminosity scans, so-called emittance scans, which were performed at the beginning and the end of each physics fill. These fast luminosity scans are similar to 'Van der Meer' scans, but last only few minutes and are performed during stable beams [11]. These scans lead to fast drops in the instantaneous luminosity. During the fill, the beam crossing is optimised every few (∼2) hours to increase the instantaneous luminosity. In 2018 the luminosity was increased (so-called 'anti-levelling') by reducing the crossing-angle in small steps from 320 to 260 μrad, during the first 6–8 h of the fill, followed near the end of the fill by

[1] LHC was designed for a fill scheme with 2808 colliding bunches, based on 72 bunches injection from PS to SPS.

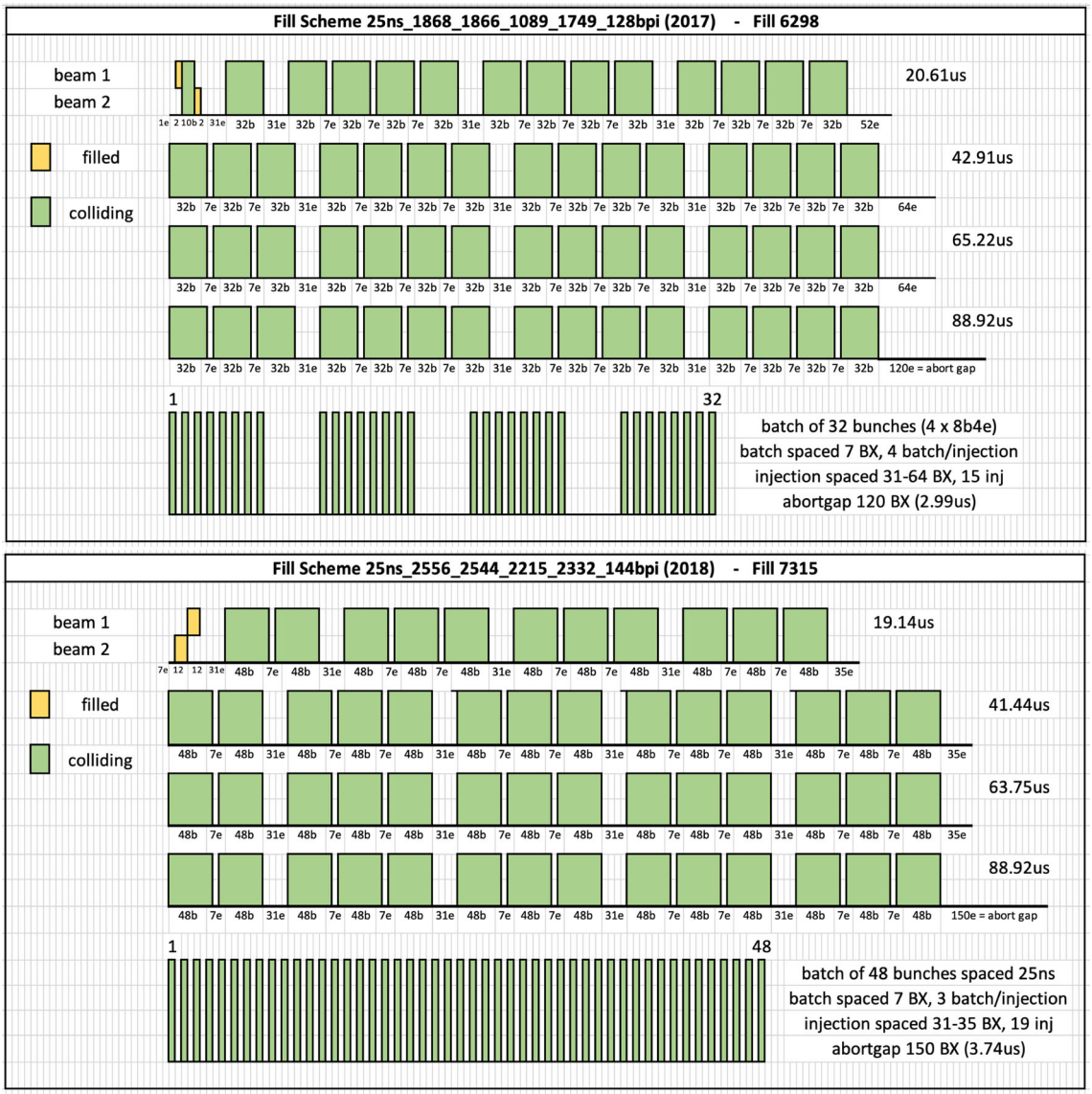

Fig. 3 Commonly used fill schemes during 2017 ('8b4e-BCS' scheme, top) and 2018 ('BCMS'-scheme, bottom)

a reduction of β^* from 30 cm to 27 cm and finally to 25 cm [21]. The reduction of β^* results in an step-like increase of the instantaneous luminosity, visible in Fig. 4 (bottom).

Figure 5 shows the instantaneous luminosity for each bunch along the orbit for LHC fill 7315 and also shows the evolution of the instantaneous luminosity in time. Two distinct features are visible:

- within bunch trains of 48 consecutive bunches, spaced 25 ns apart, the luminosity is highest at the first bunch and falls off expontially;
- within the orbit, the first bunch trains have lower luminosity with respect to the later bunch trains.

The first effect is caused by the build-up of the electron cloud induced by the first bunches in the bunch train that affect the brightness of the bunches that follow. The electron cloud interacts with the proton bunches such that the emittance for those bunches increases, and as a consequence the luminosity of those bunches decreases (see Eq. 1). The reason for the second effect is that the first bunch trains being injected earlier in the LHC are kept circulating until the injection is completed. Beam losses (emittance blow up) are larger when circulating at injection energy (450 GeV) with respect to circulation at collision energy (6.5 TeV). Injection takes typically ∼30 min. Therefore, the first bunches have higher emittance, and hence lower luminosity, with respect to the later bunches that are injected just before acceleration.

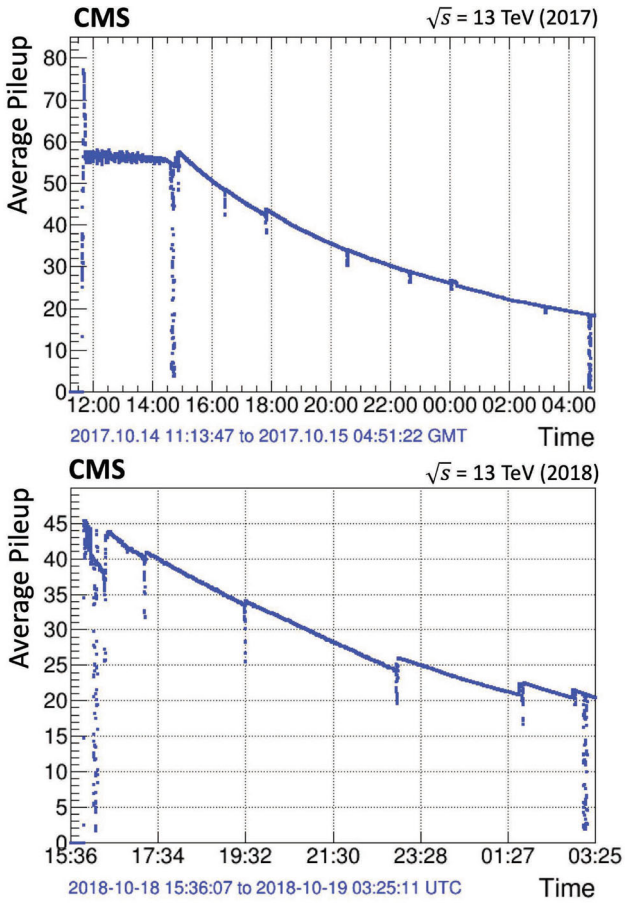

Fig. 4 Average pile-up as estimated by the CMS online luminosity monitoring during a 2017 fill with leveled '8b4e' BCS scheme (top) and during a 2018 fill with the BCMS scheme (bottom)

4 Background in the muon detector

Since the early stages of design of the CMS experiment and the muon detector it was understood that the high nominal luminosity of the LHC ($10^{34}\,\mathrm{cm}^{-2}\mathrm{s}^{-1}$) combined with the 7 TeV beam energy would have lead to a very hostile radiation environment [22–24]. The main observables to describe the radiation environment are the particle fluxes and the radiation dose. The particle flux is defined as the number of particles per unit surface and per unit time, and has the unit of $\mathrm{cm}^{-2}\mathrm{s}^{-1}$. The radiation dose is the absorbed energy per unit of mass and is expressed in Gy. Other often encountered variables are the fluence which is the time integral of flux (cm^{-2}), used to describe the accumulated radiation during an extended period (e.g. a multi-year run), and the dose rate, which is the dose per unit of time (Gy/s). The particle flux can be used to describe the detector occupancy and estimate the background hit rates, while the dose is relevant to describe radiation damage in detectors and electronics. In this section we first discuss the general features of the radiation environment and the main sources of background, thereafter we introduce simulation techniques and the background expected in the muon detector.

4.1 General features of the radiation environment

The radiation background inside the CMS detector extends to the entire experimental cavern and originates from inelastic pp-collisions without relevant physics signature: soft low-p_T scatter events, also named 'minimum-bias' events. One can distinguish three regions with different radiation characteristics [23]: (i) the main detector ($|\eta| < 3.0$); (ii) the forward region ($3.0 < |\eta| < 5.2$), which is covered by the HF; and (iii) the very forward region ($5.2 < |\eta| < 7.8$)

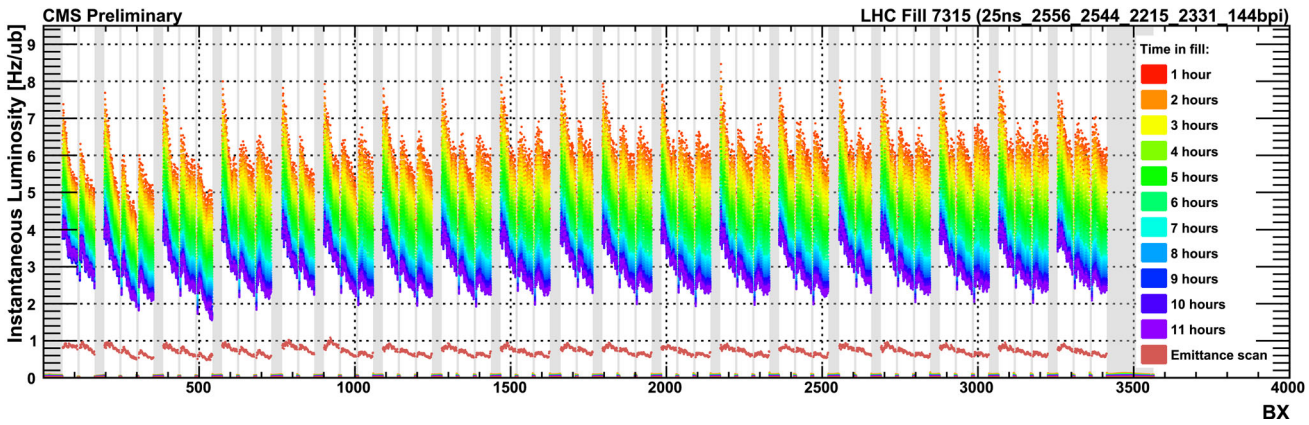

Fig. 5 Evolution of the instantaneous luminosity (Hz/μb - or equivalently $\times 10^{30}\,\mathrm{cm}^{-2}\mathrm{s}^{-1}$) per bunch along the orbit during Fill 7315. The instantaneous luminosity is averaged over different periods of about 1 h, indicated with the colour code on the right. The curve at the bottom with ≤ 1 Hz/μb luminosity is measured during the emittance scan at the beginning of the fill

that consists of the TAS collimator and its shielding. Simulations [25] indicate that on average 100 GeV of energy per event is carried by the particles emitted in the main detector ($|\eta| < 3.0$) and 750 GeV is carried by particles emitted in the forward region ($|\eta| < 5.2$). The average energy per event rises up to 4 TeV for particles emitted in the collimator region [23]. Particles emitted at $|\eta| > 7.8$ carry most of the collision energy but will pass the aperture of the collimator and leave the experimental area; therefore, do not contribute to the radiation background in the cavern.

Hadronic showers created by particles emitted in the main detector (i) might not entirely be confined in the CMS calorimeters and penetrate the muon detector, where charged particles might induce a signal. The timing of these backgrounds corresponds roughly with the collision time and is therefore referred to as *"prompt"* background. Hadronic showers also give rise to an intense neutron flux, which, because of the low neutron interaction cross-section, can easily traverse meters of steel, thermalize, and fill the cavern with a neutron gas. The timescale of this process (10–100 μs) causes the neutron background to be asynchronous and is referred to as a *"secondary"*, or *"delayed"* background. Particles emitted in the forward (ii) or very forward (iii) regions will interact in the HF, the beampipe, or in the TAS, creating intense hadronic cascades. Particles from these hadronic showers can leak out of the shielding or can be back-scattered (scattered at large angles), contributing mostly to the secondary background in the CMS cavern. The secondary background is held responsible for about 50% of the background observed in the innermost muon chambers of the endcap [23]. It is is in general largely suppressed in the innermost barrel muon chambers because of the the effect of massive shielding (solenoid and iron yoke), but it affects the weakly shielded outermost muon chambers. The most abundant particles in the cavern background are low energy neutrons, photons, and electrons and positrons.

In addition to the dominant background, produced by particles originated from pp-collisions and described above, a smaller contribution arises from beam-halo muons created by protons outside the beam envelope interacting with the beam-cleaning infrastructure, and from beam-gas interactions between beam particles and residual gas in the beampipe. These backgrounds are classified as machine induced background (MIB), and their contribution was estimated to be 3–5 orders of magnitude lower than the pp-collision induced background in the forward muon chambers, while at large radii the muon flux can be of the same order of magnitude [26]. In the most exposed regions of the muon system the MIB was predicted to remain at least two orders of magnitude below the pp-background [26]. Measurements performed during Run 1 showed that inelastic beam-gas interactions constitute the dominant source of MIB [27].

During Run 2 the inelastic beam-gas background of 1–10 Hz/cm^2/10^{11} protons per beam was measured close to the beam pipe [28], which results in a 2.5–25 kHz/cm^2 for a typical beam intensity in 2018 of 2.5×10^{14} protons. Dedicated beam loss measurements (so called *loss maps*) were performed by LHC, and combined with background measurements performed by ATLAS [29,30], to estimate the backgrounds due to losses on the collimators [31]. The fraction of background originating from beam halo was estimated at the percent level of the total MIB, confirming the dominance of the inelastic beam-gas interactions. In the muon system we estimate the beam halo background to be few hundred Hz in the barrel up to few kHz in the endcap. These beam halos might loose a substantial amount of energy in the calorimeters, leading to missing transverse energy when overlaid with a collision event. Beam halo filters have been developed to filter out efficiently these effects [32]. Phase-2 operations simulations [33] predict similar negligible rates when compared to other sources of background, therefore in this paper we will not further discuss machine induced background.

Figure 6 shows the neutron flux around and inside CMS due to pp-interactions at an instantaneous luminosity of 10^{34} cm^{-2}s^{-1}. Clearly visible are hot areas in the HF calorimeter at a distance of 11 m from the IP and in the environment of TAS at 19 m from the IP. The conical beampipe decreases in radius in front of HF, leading to high energy particles scattering on the beampipe and interacting in HF. The radiation dose is reduced thanks to the careful and optimally designed forward shielding; however radiation leaking out of the shielding is the main background for the outer muon chambers.

4.2 Background simulation

4.2.1 Simulations with GEANT4

Using the CMS simulation framework, pp-collisions are generated with Pythia [34,35], and their reaction products are tracked through the material of the CMS detector with the GEANT4 toolkit [36–38]. The simulation is extensively validated and tuned with experimental data from testbeam and pp-collision measurements [39]. The GEANT4 toolkit in the CMS software framework is optimised for CPU and memory consumption and is targeted towards the simulation of interesting physics signatures. In order to study neutron backgrounds, the tracking time of all particles has been extended to 10 s (500 ns default), and the description of geometry and materials of the CMS detector, the beampipe, the forward shielding and the cavern have been improved. Furthermore the GEANT4 routine for thermal neutron scattering was activated to model nuclei at room temperature (0 K default), leading to a peak in the low-energy neutron spectrum at 0.025 eV

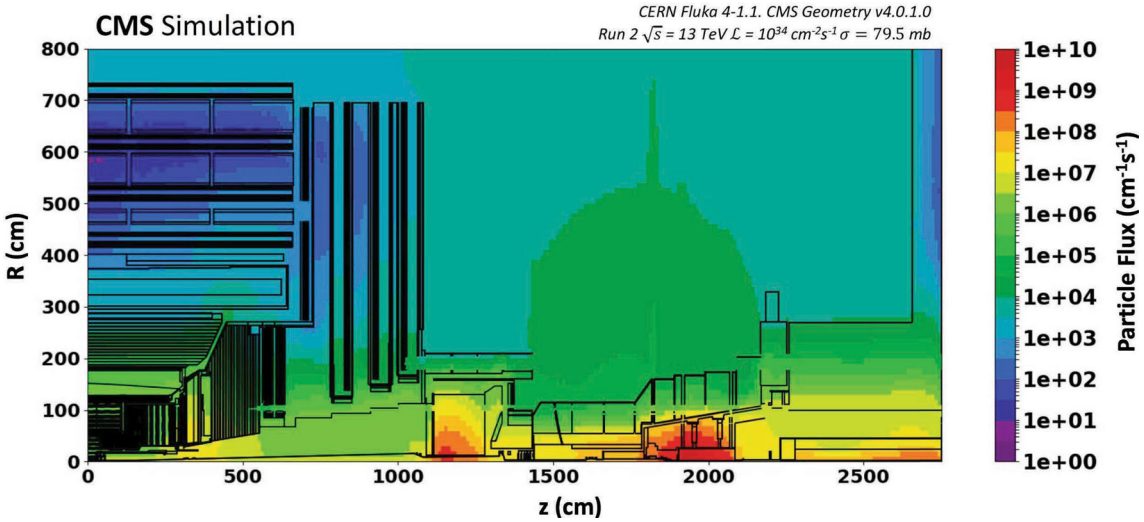

Fig. 6 Neutron flux in CMS due to $\sqrt{s} = 13\,\text{TeV}$ pp-collisions at $\mathcal{L} = 10^{34}\,\text{cm}^{-2}\text{s}^{-1}$ simulated with FLUKA. Results are averaged over 360 degrees in φ, the geometry of the CMS detector is overlaid as a cut in the Z–Y plane

[40,41]. Two packages were evaluated for the simulation of neutrons in GEANT4: HP (*high precision*), that parametrizes the existing experimental data for neutron interaction cross sections; and XS (*cross section*) which is optimised for CPU time and is derived from HP.

The simulation of neutrons in the CMS detector with GEANT4 highlights some features of neutron-induced hits. For example, Fig. 7 shows the final kinetic energy of neutrons before their interaction in the CSC versus the time of flight (TOF) referred to the primary simulated pp-collision they originated from. Neutron-induced hits can be categorised as follows: (i) hits resulting from interactions occurring less than few hundred ns after a bunch crossing, induced by "*fast*" (MeV – GeV) neutrons. These neutrons interact inelastically with nuclei, giving rise to ionizing protons and nuclear fragments, and nuclear de-excitation photons creating electrons that ionize the gas (indicated with blue markers); (ii) hits originating on the time scale of several μs, induced by ∼keV neutrons that are resonantly captured on various nuclei and also result in nuclear de-excitation photons (red markers); (iii) hits on the timescale of several ms or longer, induced by neutrons that have been cooled to thermal energies and are captured on nuclei, again resulting in nuclear de-excitation photons, giving rise to ionizing electrons (red markers). Figure 7 (top) shows the neutron energy vs time for hits created through nuclear de-excitation photons only, while Fig. 7 (bottom) overlays also the hits from knocked-out protons (magenta) and knocked-out ions (green). This illustrates the long lifetime of neutrons, giving rise to background hits in the muon detectors, arriving several ms after their original pp-collision, and that are uniformly distributed in time within the bunch-crossing of the pp-collision that triggered the event readout.

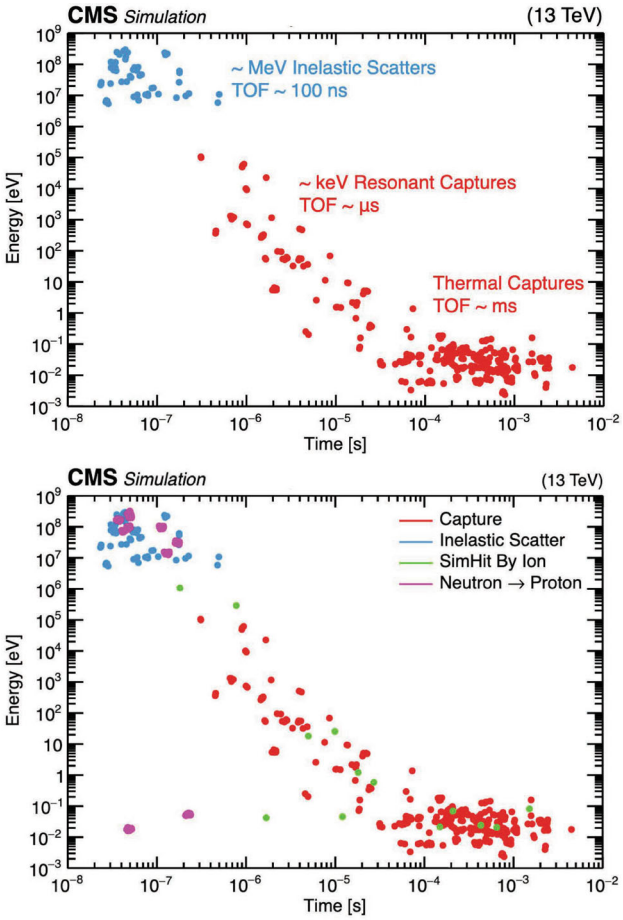

Fig. 7 Kinetic energy of neutrons before their interaction in the CSCs versus time of flight (TOF), simulated with GEANT4. Top: hits induced by electrons from photons created in inelastic scattering (blue markers), resonant and thermal neutron captures (red markers). Bottom: same as left plot, adding hits due to knocked-out protons (magenta markers) and ions (green markers) [40,41]

4.2.2 *Simulations with* FLUKA

Radiation simulations for CMS are performed centrally by the Beam Radiation Instrumentation and Luminosity (BRIL) group with the FLUKA [42,43] Monte Carlo program for the interaction and transport of hadrons, leptons, and photons. Single pp-collisions are first generated with DPMJET-III [44], and then the particles are transported through the CMS geometry with FLUKA until they decay or are below predefined energy thresholds: for hadrons 1 keV; neutrons 0.01 meV; photons 3 keV; electrons 30 keV. Significantly higher cuts-offs were used for photons and electrons in some volumes with high-Z or high-density material.

The CMS Run 2 geometry (tagged as CMS FLUKA geometry v4.0.1.0) consists of the CMS detector and the experimental cavern. The geometry is simplified to maintain reasonable computing time, while care has been taken to implement correct material composition and density. A more detailed description of the simulated geometry along with figures illustrating various details can be found in Appendix A. An in-depth discussion of CMS radiation simulation using FLUKA can be found in [45–47].

The output of the simulation is averaged over many simulated events, and is typically a set of fluences or doses. Particle fluences or doses are scored in a cylindrical $R-\phi-z$ grid covering the full cavern volume, with $\Delta R = 10$ cm, $\Delta z = 10$ cm and $\Delta\phi = 22.5°$. The fluence is calculated using the pre-defined 'USRBIN' scoring [48], which is based on the track length estimation: The contribution of a simulated particle to the total fluence in a volume element is equal to the path length of the particle inside that volume element divided by the size of the volume, and has the unit cm^{-2}. The particle flux ($\mathrm{Hz/cm}^2$) is obtained dividing the fluence by the number of pp-collisions per second. Uncertainties in the particle fluxes in the cavern are driven by imperfections in the modeling of the forward shielding [45]. FLUKA simulations of the radiation dose inside the CMS experimental cavern have been compared with radiation dose measurements and have been found to agree within a factor of 2 [47,49].

CERN FLUKA 4−1.1 was used to simulate a sample of 3×10^5 pp-collisions at $\sqrt{s} = 13$ TeV in the CMS Run 2 geometry (v4.0.1.0) described above. The results have been normalised to an instantaneous luminosity of $\mathcal{L} = 10^{34}\,\mathrm{cm}^{-2}\mathrm{s}^{-1}$ using the inelastic proton–proton cross section of $\sigma_{pp}^{inel} = 79.5$ mb. Results were recorded in a cylindrical grid of $\Delta R \times \Delta z \times \Delta\phi = 10\,\mathrm{cm} \times 10\,\mathrm{cm} \times 22.5°$, but were averaged over ϕ. Figure 8 shows the energy spectra of the particles observed in four locations of the muon detector: the innermost and the outermost stations of an external wheel for the DT and RPC detectors, the inner CSC ring of the first station, and the outer CSC and RPC rings of the fourth station.

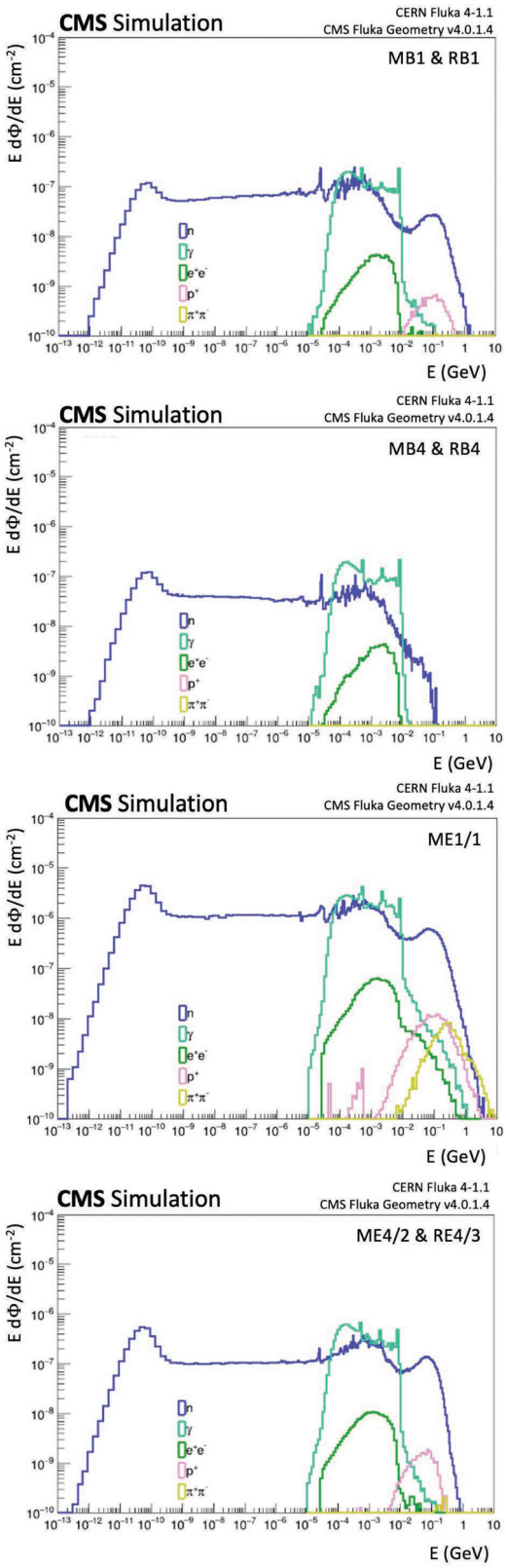

Fig. 8 Simulation (CERN FLUKA 4−1.1) of the energy spectra of the particles in the volumes covered by the MB1 and RB1 chambers of Wheel-2 (top), the MB4 and RB4 chambers of Wheel-2 (2nd plot), the ME1/1 chambers (3rd plot) and the ME4/2 and RE4/3 chambers (bottom). Fluxes are normalised to a single pp-collision

The neutron spectrum ranges from ∼1 GeV down to 1 meV and is characterised by three peaks and a rather flat plateau between the second and third peak. Starting at the high energy end of the spectrum, the first peak, around 70 MeV, corresponds to the minimum in neutron-nucleus cross section, where the neutron absorption in the calorimeters and iron yoke is lowest, we will call these the *fast* neutrons. The second peak is broad and consists of several resonances, it ranges from ∼10 keV to 1 MeV and is likely due to resonances in the scattering cross section. The third peak is located at 0.03−0.050 eV, which corresponds to the thermal limit (293 K = 0.025 eV). The nearly flat plateau towards the thermal limit is due to very slow energy loss of non-thermal neutrons since they only scatter elastically. It is interesting to note that the spectra of the neutron, photon, and electron/positron species are very similar in the four different locations in the muon spectrometer, except for the MB4 and RB4 chambers (Fig. 8, 2nd plot), where the peak of fast neutrons (10–100 MeV) is absent. This prediction from simulation indicates that, although very few neutrons are created at this location, the detectors are still within a gas of low-energy neutrons created elsewhere. In the inner station detectors, MB1 & RB1 (Fig. 8, top) and ME11 (Fig. 8, 3rd plot) the fast neutrons are leaking directly out of the nearby calorimeters, while for the outer station detectors in the endcap (Fig. 8 bottom) fast neutrons are leaking out of the forward shielding. In the detector locations where there are fast neutrons, one can observe a corresponding peak (magenta) of knocked-out protons with an amplitude that is lower by a factor of 50–100. The neutrons can also generate photons which arise from nuclear de-excitation, both after capture and inelastic scattering processes, and these photons are then the drivers of the flux of electrons and positrons, created through Compton scattering and pair production. The photon and electron/positron spectra are nearly identical in the four detector locations and are mostly concentrated in 10 keV to 10 MeV energy range. A significant fraction of pions is observed only in ME11, because they have only ∼11 λ_I of material in front, while the MB1s in the external wheel of the barrel have 13–15 λ_I of material in front because particles have to travel at an angle through the barrel calorimeters to reach them.

Figures 9 and 10 show the fluxes of all relevant particle species in the barrel and endcap muon stations for: neutrons, photons, electrons and positrons, charged hadrons, and muons. In both barrel and endcap one can observe that the photon and electron/positron flux have the same shape as the neutron flux that is driving it.

In the inner station chambers of the barrel (MB1, Fig. 9 left) one can see that the flux increases with z (and $|\eta|$) and there is a peak at $z \approx 550$ cm, which corresponds to the gap between the barrel and endcap calorimeters (see Fig. 1) that is filled with services and readout cables and has hence a lower density of material. The flux of neutrons then reduces with a factor of ∼5 going from the first to the second (MB2) station and from the second to the third (MB3) station. Peaks are seen in the photon and neutron flux in MB2 and MB3 that correspond to the gap between the heavy steel yoke elements of the barrel, where less material again results in local increases in the flux. The fourth station (MB4) has a uniform high flux of neutrons, going slightly up towards the endcap. The flux of charged hadrons and muons is of about 0.1—few Hz/cm^2 in MB1, and decreased for charged hadrons in the subsequent stations, while for muons—that can easily penetrate the iron return yoke—the flux is uniform across the detector stations.

In the endcap (Fig. 10), one can also observe the similarities between the photon and electron/positron flux on the one hand and the neutron flux that drives it on the other hand. The highest neutron flux is observed at lowest radius of the first station (ME11), and this flux drops exponentially to lower radius, until $R = 600$ cm, after which it increases because of the neutrons arriving from the cavern. The fluxes decrease going from the first station to the fourth station. The flux of charged hadrons and muons is of the order of few 100 Hz/cm^2 at the lowest radius of the innermost station and falls of to 0.1–1 Hz/cm^2 at highest radius. In subsequent stations the peak of charged hadrons and muons is few 10 to 1 Hz/cm^2 at lowest radius and reaches few 0.1 Hz/cm^2 at highest radius.

The fluxes presented in Figs. 9 and 10 can be compared to simulations performed at the time of the design of the CMS muon detector, more than 25 years ago [22,23], one can notice that the shapes and characteristic features are unchanged, the magnitude differs however between a factor two to up to a factor ten. This difference is not unexpected since back then computational power was limited, resulting in higher transport cut-off thresholds and simplified detector geometries. Idealised shielding scenarios were employed, which lacked cracks and holes introduced in the final design. The fluxes presented cannot be translated easily into expected detector rates, because the probability for a particle to create a hit in either of the detectors depends on the material used in these detectors, and depends on the energy of the particle. Furthermore the scoring of the particles with FLUKA was performed in a grid with cells of the size of 10 cm × 10 cm × 22.5°, which are much larger than the typical few mm to few cm thick sensitive gas layers. Average sensitivities can be estimated, but these cannot provide precise estimates. Therefore, in this work we will limit ourselfs to present the general characteristics of the radiation field obtained with simulations, as an illustration to understand the various features we measure in the data that will be presented in the next sections.

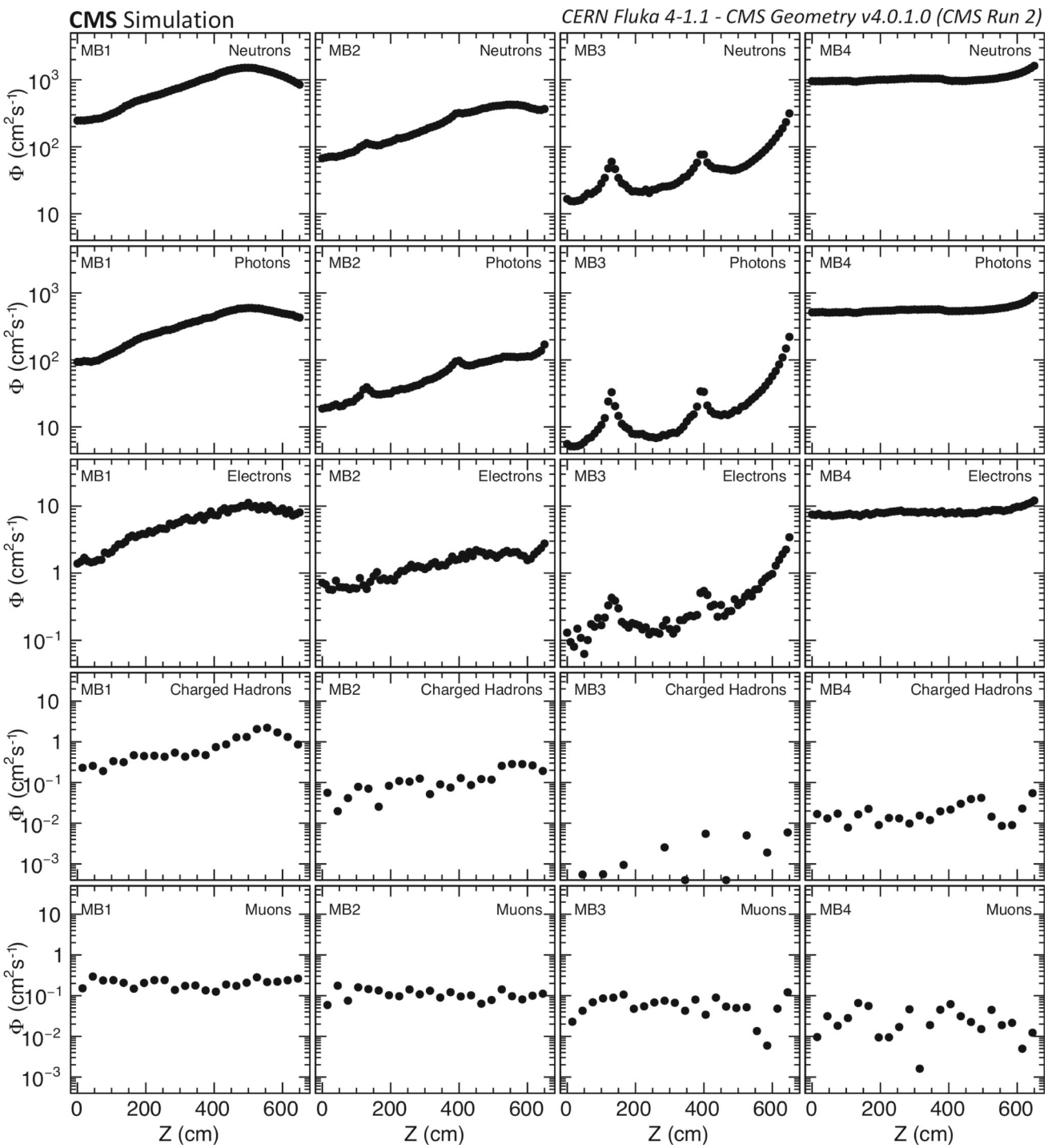

Fig. 9 Simulation (CERN FLUKA 4−1.1) of the various particle flux in the barrel muon stations (MB) of CMS. Shown are the neutron (1st row), photon (2nd row), electron and positron (3rd row), charged hadrons (4th row) and muons (5th row) particle flux. *pp*-collisions were simulated with an energy of 6.5TeV per beam ($\sigma_{pp}^{inel} = 79.5$ mb) at nominal instantaneous luminosity, ($\mathcal{L} = 10^{34}\,\mathrm{cm}^{-2}\,\mathrm{s}^{-1}$). For the simulation the CMS Run 2 geometry (v4.0.1.0) was implemented. The particle flux is shown in the four muon stations in the barrel (MB1-MB4) as function of the distance (z) along the beamline from the interaction point

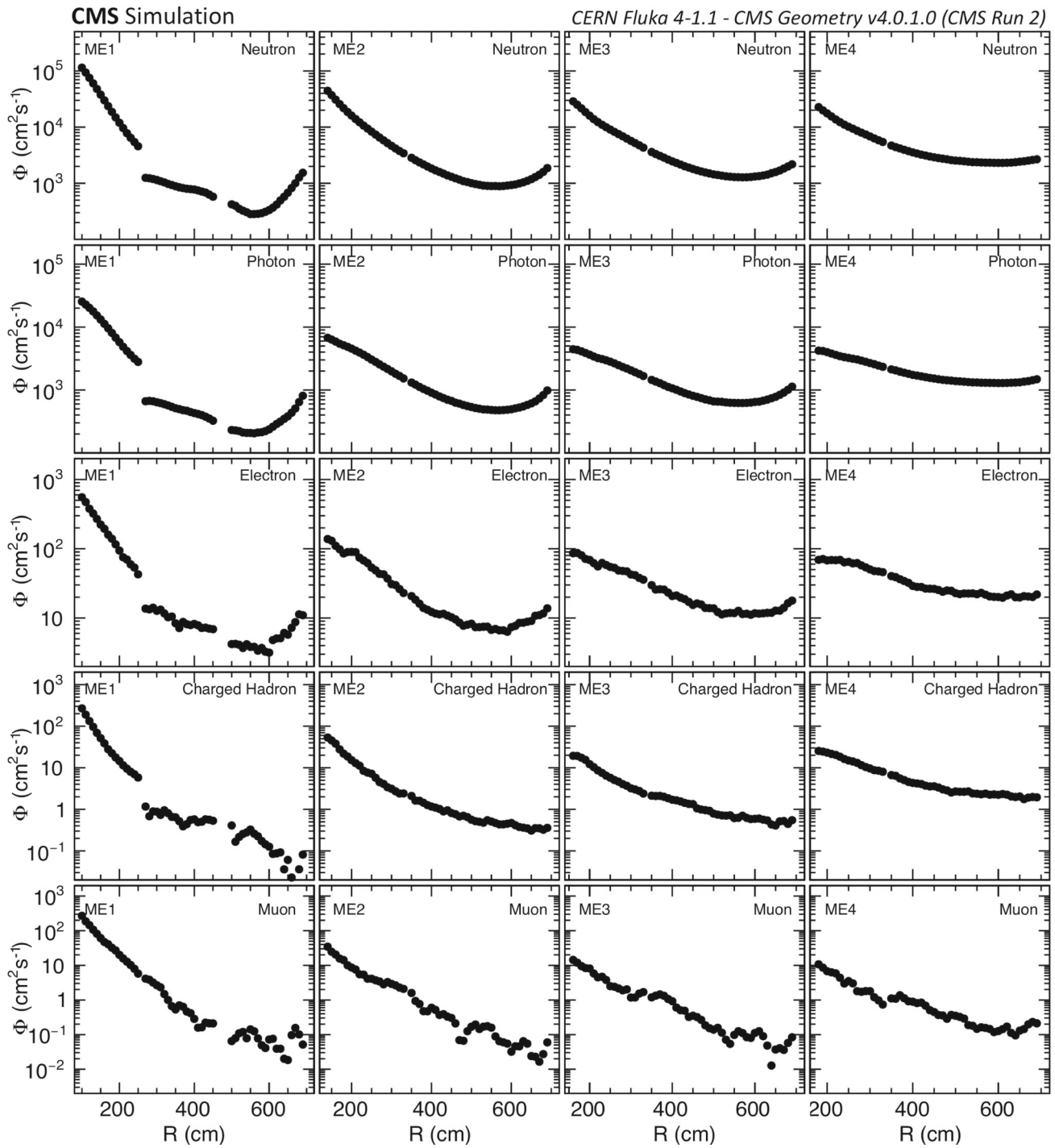

Fig. 10 Simulation (CERN FLUKA 4−1.1) of the various particle flux in the endcap muon stations (ME) of CMS. Shown are the neutron (1^{st} row), photon (2^{nd} row), electron and positron (3^{rd} row), charged hadrons (4^{th} row) and muons (5^{th} row) particle flux. pp-collisions were simulated with an energy of 6.5TeV per beam ($\sigma_{pp}^{inel} = 79.5$ mb) at nominal instantaneous luminosity, ($\mathcal{L} = 10^{34}\,\mathrm{cm}^{-2}\mathrm{s}^{-1}$). For the simulation the CMS Run 2 geometry (v4.0.1.0) was used. The particle flux is shown in the four muon stations in the endcap (ME1-ME4) as function of the distance (R) to the beampipe

5 Detector response and event selection

The CMS muon detector uses different types of gas ionization detectors: DT and CSCs for precision coordinate measurements and triggering, RPC for precision time measurements and triggering. The DTs are well suited for the low background and low magnetic field region in the barrel, while the CSCs are well suited for operation in magnetic field and higher background environment in the endcap. Because of the different technologies adopted and the different paradigms for data reduction, each subdetector therefore, measures the hit rate in a different manner. While DT and RPC read out all chambers and digitize all hits upon the acceptance of a Level 1 accept (L1A) signal, CSC requires an additional local trigger in order to record data from these chambers. In this section we will detail first the event selection and then discuss the measurement of the background rate in each muon subdetector.

5.1 Data selection

For the measurement of the background hit rates we analysed runs taken from Oct 1st to Oct 23rd in 2018. In this last period of 2018 *pp*-collisions, the LHC was configured for luminosity production using the 2544 colliding bunch scheme. The instantaneous luminosity during these fills, varied from 0.6 to $1.9 \times 10^{34}\,\mathrm{cm}^{-2}\mathrm{s}^{-1}$. For the analysis of the background rate in the CSC detectors, up to 95 fills were selected for a total integrated luminosity of $33\,\mathrm{fb}^{-1}$. For the analysis of DT and RPC data, less events were required to obtain similar statistical precision on the hit rates and only a few good long fills were analyzed for in total $1.5\,\mathrm{fb}^{-1}$ for the DT and $2.3\,\mathrm{fb}^{-1}$ for the RPC system. Data were selected with a set of zero-bias triggers that requires the crossing of proton bunches, detected by the coincidence of two simultaneous signals in the beam pick-up monitors installed along the beamline at opposite sides of CMS. Some triggers were used to trigger on a crossing of filled and non-filled bunches as well as on empty-empty crossings. These triggers are typically used for monitoring and have large prescales in order to collect data at rates of less than a Hz, resulting in low statistics. On the other hand, they provide detector read-out during bunch crossings without *pp*-collisions, allowing the monitoring of the hit rate in the detectors along the entire LHC orbit. In 2018, the zero-bias triggers accounted for approximately 35 Hz to be confronted to nearly 1 kHz of triggers dedicated to selection of interesting events for analysis.

5.2 Hit rate definition

DT and CSC are multi-layered chambers (8–12 layers for DT; 6 layers for CSC), while the RPC chambers have a double gap structure, they have only a single strip layer that is reading out the hits. Particles passing through the detector can leave hits in multiple layers. E.g. a muon crossing a CSC chamber will typically result in six hits. Background particles can have also different hit patterns: e.g. a high energy punch through pion or proton in a CSC will give rise to six hits, whereas neutrons typically result in hits in a single or few layers. Therefore, we can distinguish two different rate definitions:

- The *single-layer hit rate* counting the hit rate in a single layer by making an average over all the layers of the chamber. This hit rate is closely related to the electronics counts of the chamber and is often used in online measurements of the hit rates where scalers count channels over threshold. This hit rate definition is useful for future comparisons to Monte-Carlo simulations with GEANT4 where particles passing through sensitive volumes result in an electronics hit.
- The *particle rate* where close-by hits, likely induced by the same particle, are clustered. This particle rate is a good estimate for particle flux in the muon detector, and is useful to compare to background simulations performed with FLUKA simulations that have as observable not single hits in a chamber, but a particle flux in a certain volume element of the muon detector.

Hit patterns in the DT or CSC system with hits in three or more layers are clustered into segments. To maximise the muon reconstruction efficiency, in the DT system all possible segments are reconstructed for a given set of hits, leading to multiple use of the same hits. This causes non-linear effects in the rate of reconstructed background segments as the number of combinations increases with hit multiplicity at high instantaneous luminosities.

5.3 Drift Tubes

Ionising particles passing through a drift tube cell will create primary electrons along its trail in the gas. Depending on their position inside the cell, the drift distance can be up to 21 mm, with a $54.6\,\mu\mathrm{m/ns}$ drift velocity that results in a maximum drift time of $\sim$385 ns. The staggering of the drift tube cells within the superlayer leads to different drift times in the various cells crossed by a track. The staggered geometry was designed to implement the *Mean Timer* algorithm [50] on which the local trigger logic is based. With a maximum drift time of 16 BX, the readout window needs to be large enough to fully contain the signal and to allow for shifts related to time-of-flight, cable length differences and trigger latency. All these shifts are eventually corrected for by the calibration process. The DT readout window is set to be 1250 ns, this means that it collects both signal and background hits produced in those 50 BX window around the L1A signal.

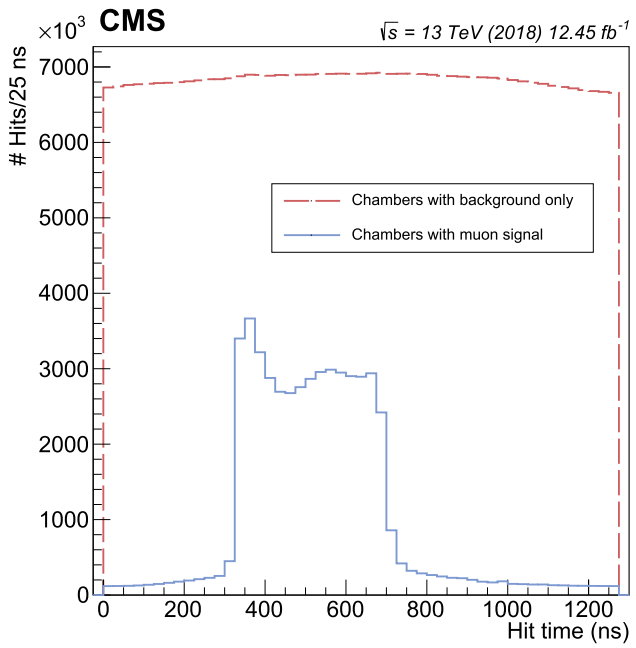

Fig. 11 Time distribution of *signal* (full blue line) and *background* (dashed red line) hits, respectively found in chambers crossed or not crossed by reconstructed muons. Signal hits are mainly recorded within the time range corresponding to the maximum DT drift time (385 ns), while background hits show a flat time distribution within the full DT readout window of 1250 ns. The two distributions were obtained using a sample of candidate $Z \rightarrow \mu\mu$ events

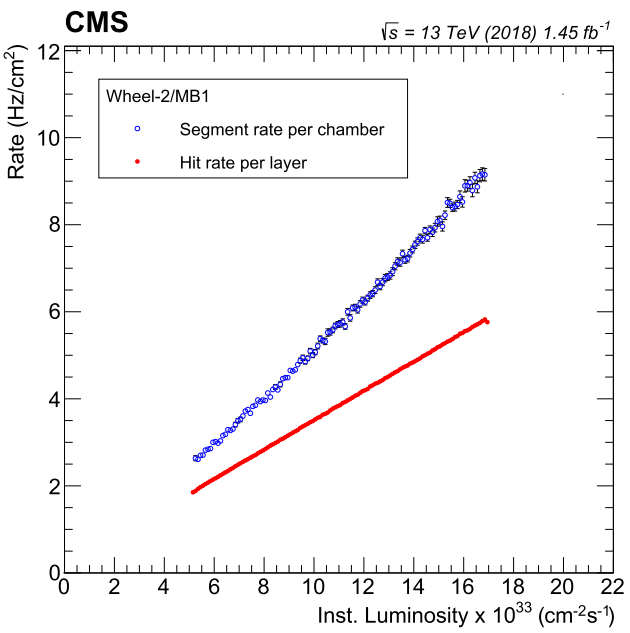

Fig. 12 Rates of background hits per layer (full red markers) and rate of background track segments per chamber (open blue markers), versus the instantaneous luminosity in DT chambers of the first station of Wheel-2 (W-2/MB1)

Figure 11 shows the distributions of the uncorrected TDC counts for signal hits compared to background hits in a muon enriched sample of 2018 pp-collisions with at least two well identified muons (candidate $Z \rightarrow \mu\mu$ events). Hits in the DT chambers crossed by muons are indicated with the full blue histogram, showing the time distribution of signal hits with a small contribution of background hits found in the same chamber. Hits registered in chambers not crossed by any muon are shown with the red dashed histogram and they are pure background hits. The background populates uniformly the 50 BX readout window while the signal hits are all concentrated in the approximately 400 ns interval corresponding to the maximum drift time. The rising (left) edge of the histogram corresponds to 0 ns drift time (set at 0 ns during the calibration), i.e. to hits created by muons crossing the DT cell very close to the anode wire; the falling (right) edge corresponds to the maximum drift time, i.e. hits created by muons crossing the DT cell very close to the position of the cathode strips.

For the readout of the DT system, no chamber-level pretrigger is required. Upon a L1A signal, all channels are read out. The background in the DT chambers can therefore be addressed, by selecting, on event-by-event basis, those chambers that were not crossed by any reconstructed muon. Since the muon reconstruction is highly efficient also for cosmic muons, that are asynchronous respect to the LHC clock and typically do not cross the interaction point, this selection rejects contamination from nearly all non-collision muons.

To estimate the hit rate normalised to the surface of a chamber, the total amount of background hits are counted, event by event and chamber by chamber, and divided by the total readout time window (1250 ns) and by the total surface of all layers inside each chamber. The track segment rate normalised to the surface of a chamber is estimated by counting the locally reconstructed background segments, event by event and chamber by chamber, and by dividing them by the time window that is taken into account by the local reconstruction, which corresponds to the maximum drift time, and by the chamber surface. As mentioned above, the 50 BX wide readout window collects hits originating from many collisions before and after the triggered event, and in particular also collects background hits produced in time intervals where, depending on the LHC filling scheme, no pp-collisions took place.

Figure 12 shows the hit rate per layer for all chambers of the first station of Wheel-2 (W-2/MB1) as a function of the instantaneous luminosity, which is computed with the granularity of 1 *lumi section*[2] (LS), lasting about 23.3 s. The plot shows also the rate of track segments in the same subset of chambers. Since track segments can be made up with a minimum of 3 hits per chamber (i.e. a track segment can have

[2] In CMS the length of a luminosity section or lumi section is defined as 2^{18} LHC orbits.

missing hits in some layers), the segment rate can easily be higher than the single hit rate per layer. Single hit rate shows a linear dependence with instantaneous luminosity for all chambers and has negligible intercepts, ranging from 0.005 to 0.1 Hz/cm^2, that can be related to spurious hits due to noise, and residual hits due to cosmic ray and beam halo muons passing the selection criteria.

5.4 Cathode strip chambers

To reduce the CSC event size, a CSC chamber is required to have a local trigger in order to send its data to the data acquisition. As a consequence, data recorded from any CSC chamber will include at least a track segment, which will bias the measurement of the background if not properly removed. The readout window of the CSC chambers is 400 ns (16 BX) and most of the collision muon signals are within the 3 central BX. The time resolution of the CSC anode signals is about 8 ns; therefore a small (∼10%) fraction of signal hits are assigned to the neighbouring BX = ±1. Using time information of CSC signals from all six layers improves the time resolution for a track segment to be ∼3 ns. Two methods have been developed to remove the bias due to the local trigger, one based on excluding hits in the area of the chamber where the local trigger was generated, another on excluding hits within the five central BXs in which prompt charged particles create hits in the chamber. Results of both methods are in good agreement. For the analysis of the background we will use hits produced by the anode wire groups (hereafter referred to as WG hits), as they provide fine granularity information in η. Cathode strip hits are not suited for the analysis as not all the strips of a chamber are read out, but only the strips close to the passage of a charged particle. The use of combined wire group and cathode strip information (so-called 2D hits) is also problematic because of the creation of ghost hits[3] in case two or more real hits are present. Noisy wire groups have been identified and discarded for this analysis.

Since the local trigger requirement for readout significantly reduces the amount of available data per event, adequate statistics were collected by analysing a large sample of 94 fills with the same 2544 colliding bunch structure, for a total of 33 fb^{-1} of certified pp-collisions. The data are selected in the following way: only WG hits inside CSC chambers not associated with any reconstructed muon are selected. The read-out CSCs have at least one Anode Local Charged Trigger (ALCT). To remove the local trigger bias, the chamber is divided in two areas, based on the key wire group (key-WG, wire group of the ALCT in layer 3), so-called *lower* (smaller η) or *upper* (higher η) part. If the key-WG associated with the highest quality ALCT is in the lower/upper part of the CSC, then only the upper/lower part of this chamber is used in the analysis. This division in upper and lower parts on the one hand eases the computation as they have a fixed area, on the other hand eliminates also hits due to delta-rays originating from the charged particle firing the ALCT. Figure 13 shows the WG hits in an event in a single CSC chamber. In total 12 individual hits are registered in this event, that can be clustered in 5 particle hits, used for the calculation of particle rate. The grey shaded area indicates the CSC wire groups containing the ALCT, that are discarded for the analysis of the background rate in this chamber.

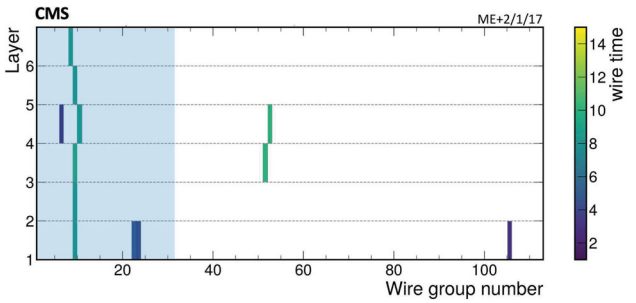

Fig. 13 The event display of CSC ME+2/1/17 wire group signals recorded in one of pp-collisions event. One can see WG hits in six layers that make up a straight pattern, which have lead to an ALCT resulting in the readout of the chamber. For this specific event this part of the chamber is excluded for the analysis of the background and is shown as a grey shaded area

The background rate is then calculated both for the upper as the lower part and an area-weighted average defines the background rate for the entire chamber. The rate in the upper/lower part is defined as follows:

$$R_{\text{upper|lower}} = \frac{\sum_{i=1}^{n} \text{nHits}(\Delta t)}{n \cdot \Delta t \cdot A_{\text{upper|lower}}} \quad (2)$$

with n being the number of times a certain chamber has sent data to readout (i.e. a counting experiment with n counts); nHits(Δt) the number of background hits in some time interval Δt in the upper/lower part; and $A_{\text{upper|lower}}$ the area of the upper/lower part of the CSC chamber under study. After removal of the ALCT the WG hit, timing is found uniform and Δt was tuned to remove electronics bias in the first time bin. The number of hits nHits can be defined in two different ways:

1. One can consider all single WG hits as an individual hit, and by this way we can define the *single layer hit rate* which equals the electronics counts. As the single layer hit rate is calculated as the average of the hit rate in the six layers, the total chamber rate is six times the single layer hit rate.
2. As one can observe in Fig. 13, the single hits are often clustered because of a particle giving rise to hits in subsequent layers or in adjacent wire groups. Therefore, a

[3] Additional 2D hit positions at the intersection of cathode strips and anode wires where no real particle has passed.

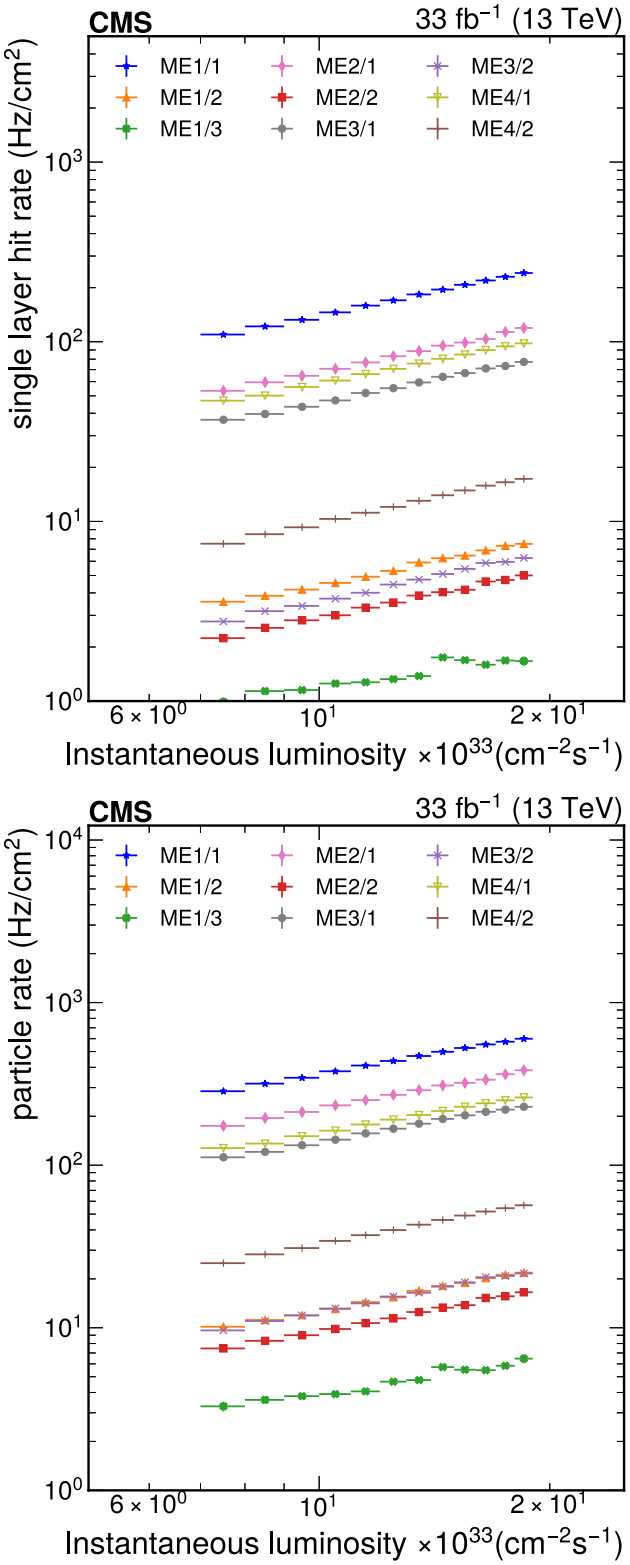

Fig. 14 Single layer hit rate (top) and particle rate (bottom) for the different CSC chamber types as function of instantaneous luminosity, measured in the Zero-Bias dataset of *pp*-collisions collected during the 2544 colliding bunch fills of LHC in 2018

clustering algorithm was implemented and we define *particle rate* as the rate measured when counting clusters as hits. A set of WG hits is considered a cluster if it satisfies one of the following criteria:

- Δ(WG #) + Δ(layer #) $\leq$ 2 and Δ(time) $\leq$ 2;
- Δ(WG #) = 0;
- Δ(layer #) > 0 and Δ(WG #)/Δ(layer #) $\leq$ 1.

The cluster size follows an exponentially falling distribution with an average that varies from 2.6 to 3.3 depending on the stripwidth of the different chamber types.

Figure 14 shows both the *single layer hit rate* (top) as the *particle rate* (bottom) for the ten different CSC chamber types as function of the instantaneous luminosity. Good linearity is observed of both the single layer hit rate and the particle hit rate versus the instantaneous luminosity, few fluctuations are observed in ME1/3 chambers that suffer from low statistics. The highest background is observed in the ME1/1 chambers, and within each station inner ring chambers (MEx/1) see higher rates than the outer ring chambers (MEx/2, ME1/3). The highest background in the outer ring chambers is observed in ME4/2, which is most exposed to cavern background. Fits performed to the hit rate show negligible intercepts for outer ring chambers (0.5–1 Hz/cm^2), which can be attributed to detector noise or hits due to cosmic muons failing to be removed from the analysis. Inner ring chambers have significant intercept ranging from 30 Hz/cm^2 for ME4/1 to about 70 Hz/cm^2 for ME1/1. This rate at zero instantaneous luminosity can be attributed to detector noise, residual hits from cosmic and beam halo muons after selection, and possibly also due to the activation of the CMS detector structural material (mostly steel) in the area with highest particle fluxes.

5.5 Resistive plate chambers

The RPCs have a time resolution of ~1.5–2 ns. Therefore, their hits are assigned the correct bunch crossing with more than 99.9 % probability. The RPCs have an intrinsic rate due to noise of the order of 0.1 Hz/cm^2. Most noisy strips and noisy chambers were identified and removed from the analysis, although so far no satisfactory method has been developed to clean the noise completely. The RPCs are read out in a 150 ns wide readout window (BX in [− 3,+2]). In muon-enriched event samples, the hits are sharply peaked at BX = 0 that contains all prompt signal hits as well as background, while the bins with BX $\neq$ 0 are uniformly populated by background hits only. Analysing Zero bias triggered events, the contribution of hits originating from collision muons was found very small with respect to the background hits. The

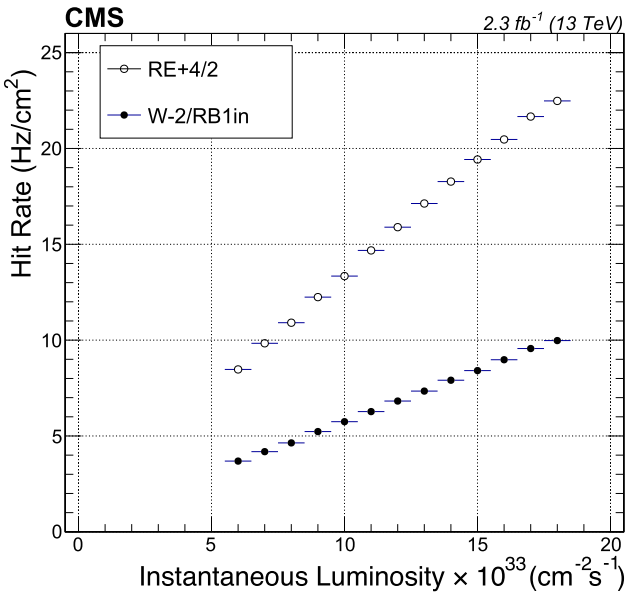

Fig. 15 Hit rate versus the instantaneous luminosity in RPC chambers of the first station of Wheel-2 (W-2/RB1in) and in RPC chambers of the inner ring of the 4th station

rate in the RPC chambers is calculated as follows:

$$R = \frac{\sum_{i=1}^{n} \text{nHits}(\Delta t)}{n \cdot \Delta t \cdot A} \tag{3}$$

with nHits the number of hits (clustered strips) in the time interval Δt, n the number of events and A the effective area of the RPC chamber, excluding noisy or dead strips. The hit rate can then be plotted as function of the instantaneous luminosity, as shown in Fig. 15 for a set of chambers in the inner most station of an external wheel in the barrel (W-2/RB1in), and for one set of chambers in the inner ring of the 4th station in the endcap (RE+4/2). The hit rate in all chambers is linear with respect to the instantaneous luminosity. Small intercepts of $< 0.5\,\text{Hz/cm}^2$ are measured for most chambers (with about 5% of the chambers with intercept up to 1.5–2 Hz/cm^2) and they are compatible with the hit rate measured in cosmic ray data taking, which gives an estimate for the intrinsic rate of hits due to noise and cosmic muons. A linear fit is used to extract the hit rate and uncertainty on the hit rate is derived from the fitted parameters:

$$R(x) = p_0 + x \cdot p_1 \tag{4}$$

$$\sigma_R(x) = \sqrt{\sigma_{p_0}^2 + x^2 \cdot \sigma_{p_1}^2 + 2 \cdot x \cdot \text{cov}(p_0, p_1)} \tag{5}$$

with x the instantaneous luminosity in units of $10^{34}\,\text{cm}^{-2}s^{-1}$. In reality, the correlation between the two fit parameters is typically $< 10^{-4}$ and can be neglected.

6 Hit rate in the muon spectrometer

In this section, a global picture of the background in the muon detector will be presented. The hit rate observed in the muon detectors depends on the detection technology as well as on the location of the detector within CMS. The hit rate will be lower at larger distance from the interaction point because of those detectors being shielded better (due to the iron yoke) as well as due to the reduced solid angle covered for the same unit surface. Muon detectors that are installed closest to the interaction point will see mostly prompt background and we expect this background to be distributed uniformly in ϕ. The outermost detectors will be more affected by the background originating from the neutron gas in the cavern and their rates should reflect the neutron gas density distribution in the cavern. We will first show the rates as function of η in the muon detector, thereafter discuss the rate as function of ϕ. All measurements show the hit rate in the detectors at an instantaneous luminosity of $\mathcal{L} = 10^{34}\,\text{cm}^{-2}\,\text{s}^{-1}$, an average value for the instantaneous luminosity during detector operation in Run 2.

6.1 Hit rate as function of pseudorapidity

The multiplicity of charged particles emitted from pp-collisions as function of pseudorapidity shows a slight increase from $|\eta| = 0$ to $|\eta| = 2.5$ [51,52] after which it drops significantly [25] for $|\eta| \geq 2.5$, which is also the reason why this region is not covered by the LHC general purpose detectors tracking systems. The definition of the pseudorapidity as the negative natural logarithm of the tangens of half the polar angle θ implies an exponentially rising number of charged particles per unit area. This increased charged particle flux results in an increase of the background in the muon detector (expressed in Hz/cm^2) towards higher $|\eta|$. While the number of charged particles drops significantly beyond $|\eta| = 2.5$, the energy of those particles is more energetic as they carry larger fraction of the momentum of the colliding constituents, peaking between $5 < |\eta| < 10$. The interaction of these particles in the forward shielding ($5.2 < |\eta| < 7.7$) and in the Target Secondary Absorber ($7.7 < |\eta| < 7.8$) protecting the LHC focusing quadrupole magnets leads to creation of a large flux of background particles at high pseudorapidity that spreads in the entire cavern and affects mostly the outer muon chambers. Generally we expect an increase of the measured background in the muon system with increasing pseudorapdity, which is highest for the innermost chambers of both barrel and endcap (i.e. the first muon station), and reduces in the subsequent muon stations, with exception for the outermost muon station that is affected by the cavern background.

Figure 16 (top) shows the single layer hit rate in the muon barrel detectors. The hit rate in the barrel (DT,RPC) system

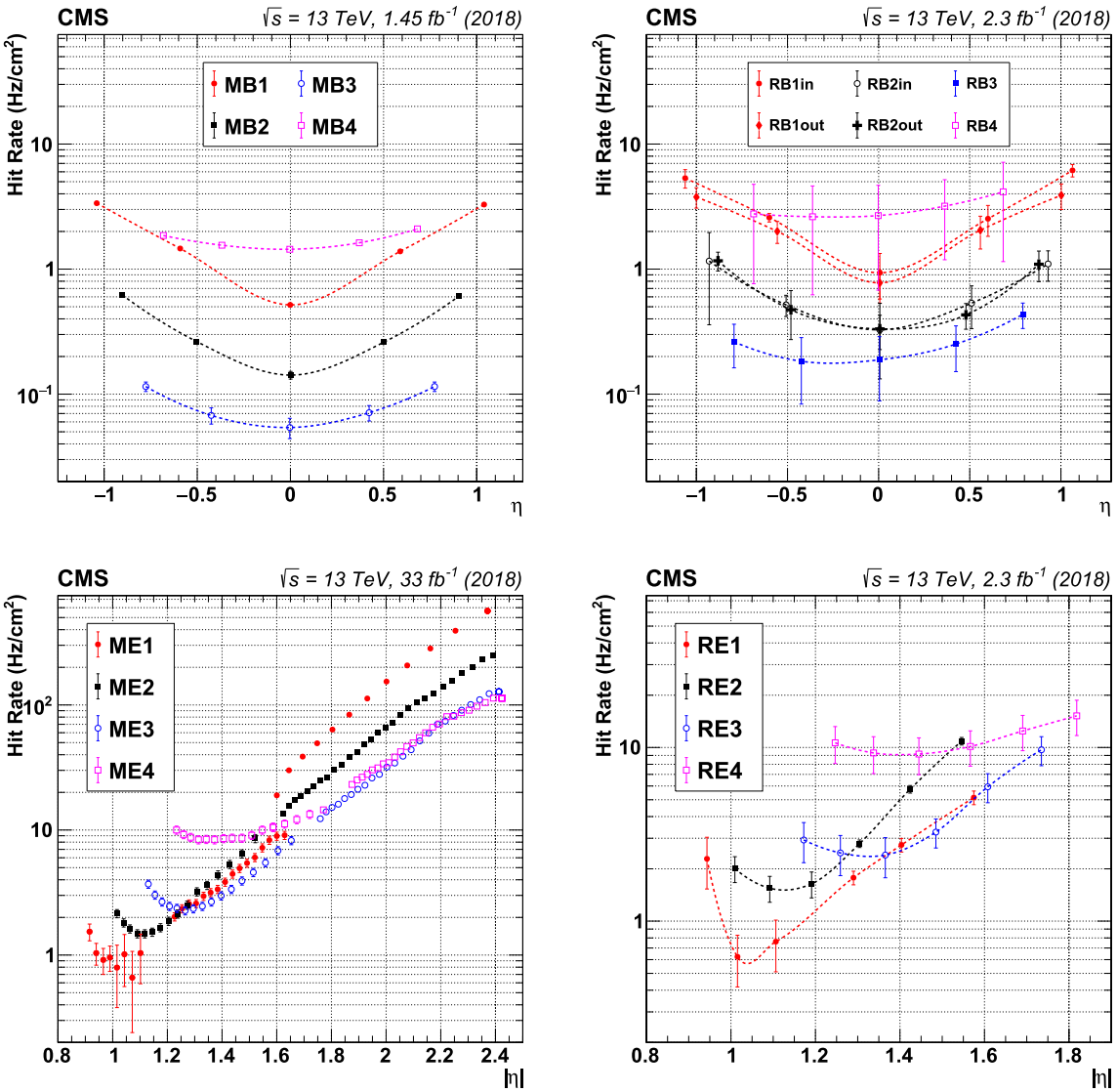

Fig. 16 Single layer hit rate as function of pseudorapidity for the different muon stations in the barrel for the DTs (top left) and RPCs (top right), and in the endcap for the CSCs (bottom left) and RPCs (bottom right) at an instantaneous luminosity of $10^{34}\,\mathrm{cm}^{-2}\mathrm{s}^{-1}$

is symmetric, with the exception of the hit rate in the outermost station (MB4,RB4) where slightly higher background was measured in the positive wheels. This asymmetric neutron flux is caused by the access shaft to the underground cavern, located at the negative side, which reduces the back scattering of neutrons in the concrete of the cavern and results in a slightly lower neutron flux. With the exception of the outermost station, the background drops with an order of magnitude going from the first muon station (MB1, RB1in and RB1out) to the second muon station, and drops again significantly in the third muon station, which is the most shielded station and has overall lowest background. The backgrounds in all stations increase with increasing pseudorapidity. Backgrounds are slightly higher in the RPC system with respect to the DT system which can be attributed to the different materials used in the construction of these detectors, leading to a different sensitivity of these detectors to detect background hits.

The hit rate in the endcap (CSC,RPC) system is shown in Fig. 16 (bottom). The rate increases exponentially with the pseudorapidity and the highest rate is measured in the innermost chambers which cover $1.6 < |\eta| < 2.4$. The rate in the innermost chambers is highest in the first station, followed by the 2nd station and with the 3rd and 4th stations having roughly equal rate. The rates in the outermost chambers ($|\eta| < 1.6$) are highest in the outermost station, and are lowest for the first station because of the increased amount of material (additional λ_I due to barrel yoke, see Fig. 1) that has to be traversed. An increase of rate is visible in all stations for the lowest pseudorapidity values because of the exposure to

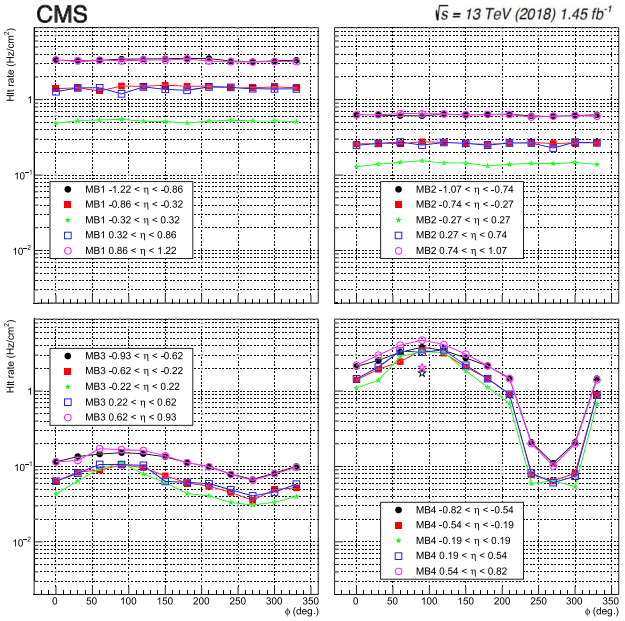

Fig. 17 Hit rate in the DT chambers as a function of the azimuthal angle ϕ for the 4 stations: MB1 (left top), MB2 (right top), MB3 (left bottom), MB4 (right bottom) at an instantaneous luminosity of $\mathcal{L} = 10^{34}\,\mathrm{cm}^{-2}\,\mathrm{s}^{-1}$. The rates measured with shielding installed on top of the outermost MB4 chambers of Wheel ±2 sector 04 are indicated with star markers

the neutron background in the cavern that penetrates inside the muon detectors. The first station of the endcap RPC system has no chambers installed beyond $|\eta| > 1.6$ and the highest rates are hence observed in the outermost chambers of the 4th station.

These values can be compared to the estimates made nearly 25 years ago, based on FLUKA simulations [53]. While the estimates made back then were about right for the muon detectors in the Barrel (1–4 Hz/cm^2), the maximum rates for the muon detectors in the endcap were underestimated by a factor two for ME1/1 (estimated 300 Hz/cm^2 – measured 600 Hz/cm^2) to a factor five for ME2/1, ME3/1 and ME4/1 (estimated respectively 50 Hz/cm^2, 30 Hz/cm^2 and 50 Hz/cm^2 – measured 250 Hz/cm^2, 150 Hz/cm^2, and 250 Hz/cm^2). While the detectors were designed with sufficient safety margin, these measurements support the past and currently ongoing efforts to improve the shielding in the forward region of CMS.

6.2 Hit rate as function of azimuthal angle

Figure 17 shows the single layer hit rate in the DT chambers as function of the azimuthal angle ϕ. Since CMS is cylindrically symmetric, we expect a uniform distribution of the rate. The highest rate is observed in the innermost station MB1 (Fig. 17 top left), followed by MB2 (top right) and MB3 (bottom left). The hit rate in MB1 and MB2 are uniform in ϕ which indicates that the background in the first two stations (MB1 and MB2) is dominated by background originating from pp-collisions and reflects the good ϕ symmetry of the material budget of the barrel inner detectors and calorimeters. The rate is also very symmetric between positive and negative wheels in the first three stations (nearly perfect overlap of black and magenta markers for Wheel ±2, and of the red and blue markers for Wheel ±1), while a slight deviation is observed for the MB4 top chambers, both in Wheel ± 2 as in Wheel ±1.

The highest rate in MB1, ∼3.5 Hz/cm^2, is observed in the external wheels of the Barrel that cover $0.86 < |\eta| < 1.22$, while rates in the intermediate wheels are about ∼1.5 Hz/cm^2, and in the central wheel the rate is ∼0.5 Hz/cm^2, which is explained by the pseudorapidity distribution of charged tracks and the reduced surface area covered by a fixed $\Delta\eta$ as $|\eta|$ increases (see Fig. 1). The hit rate in MB2 are a factor 5.4 lower with respect to the rates measured in MB1 (with exception of Wheel 0 where the ratio is merely 3.7), which is due to the 30 cm (nearly $2\lambda_I$) thick iron ring of the flux return yoke separating MB1 and MB2.

The hit rates in the third and fourth stations (MB3 and MB4) deviate from the uniform distribution observed in the first two stations, indicating that the background is coming mostly from the cavern and not from prompt collision products. A higher background rate is measured in the top sector chambers ($45° < \phi < 135°$) with respect to the bottom sector chambers ($225° < \phi < 315°$) which are more protected from penetrating neutrons due to the limited distance of ∼1.5 m between the iron floor and the bottom chambers, while the distance between the top chambers and the cavern wall is about 7.5 m. There is about 60 cm of the return yoke iron between MB2 and MB3, and the reduction factor of the rate varies from 5 for the outer wheels, over 3.7 for Wheel ±1 to 2.3 for the central wheel. Another 60 cm of iron separates the MB3 chambers from MB4 that are exposed to the cavern background. The rate in the MB4 stations is at its maximum at 90° (sector 4), being 3 to 4 Hz/cm^2 and is minimal at 270° (sector 10): 0.06 Hz/cm^2 of the inner wheels and 0.1 Hz/cm^2 for the external wheels.

Large hit rates could lead to reduced lifetime of the detectors which is governed by the integrated charge on the wires. Therefore, prototype shields were installed on the top MB4 chambers of Wheel ±2 during technical stops in 2016 and 2017: All shields consist of 7 mm of lead combined with different thickness of borated polyethylene (BPE). On Wheel +2: 7 mm Pb + 90 mm BPE; On Wheel -2, half of a chamber was covered with 7 mm Pb, 30 mm BPE and 10 mm stainless steel and another half was covered with 7 mm Pb and 50 mm BPE. The shielding on Wheel +2 lead to a reduction of nearly 60% of the background (Rate in 2018: 2 Hz/cm^2), while the shielding on Wheel-2 lead to a reduction by about 50% (1.7 Hz/cm^2). The shielding on Wheel +2 was found to be slightly more effective due to the increased thickness of the borated

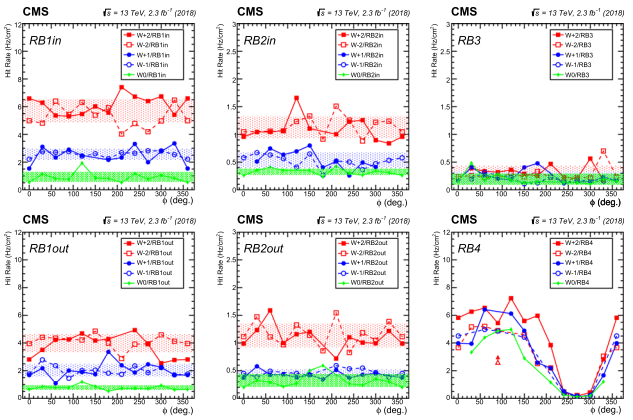

Fig. 18 Hit rate in the barrel RPC as a function of the azimuthal angle ϕ at an instantaneous luminosity of $\mathcal{L} = 10^{34}\,\mathrm{cm}^{-2}\,\mathrm{s}^{-1}$: RB1in (top left), RB1out (bottom right), RB2in (top middle), RB2out (bottom middle), RB3 (top right) and RB4 (bottom right). Excursions from the expected uniform hit rate in ϕ are due to chamber-by-chamber fluctuations in the noise rate and for these stations an uncertainty band (RMS value) around the mean value is drawn. The rates measured with the shielding installed in the outermost RB4 chambers of Wheel ±2 sector 04 are indicated with open (W-2) and filled (W+2) triangles

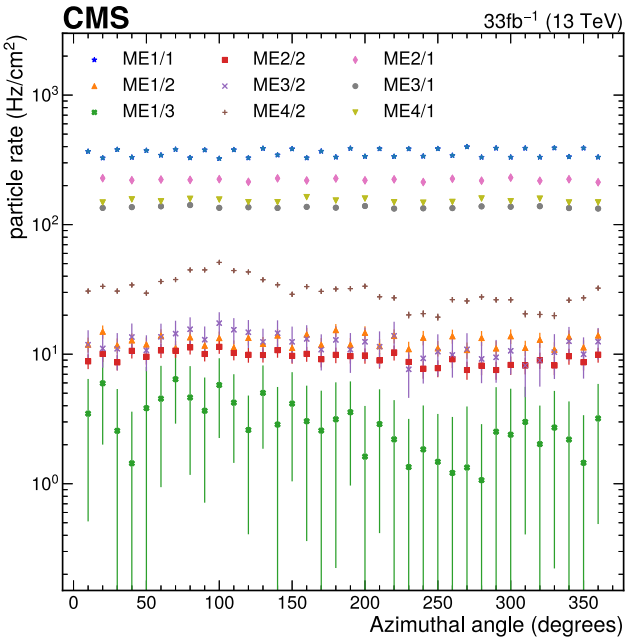

Fig. 19 Particle hit rate in the CSC as function of the azimuthal angle ϕ at an instantaneous luminosity of $\mathcal{L} = 10^{34}\,\mathrm{cm}^{-2}\,\mathrm{s}^{-1}$

polyethylene. During Long Shutdown 2 (LS 2), the shielding was extended to all accessible top MB4 chambers to preserve their longevity.

Figure 18 shows the rate in the barrel RPC chambers as a function of the azimuthal angle ϕ at an instantaneous luminosity of $\mathcal{L} = 10^{34}\,\mathrm{cm}^{-2}\,\mathrm{s}^{-1}$. Similar as to the DT chambers the highest rate are observed in the innermost chambers of the external wheels (Wheel ± 2/RB1in, $\sim 6\,\mathrm{Hz/cm}^2$) and the top chambers of the most outward chambers (RB4, $\sim 6\,\mathrm{Hz/cm}^2$). As a consequence of the radiation shielding of YB ± 2/MB4, the background drops with about 50% to $\sim 3\,\mathrm{Hz/cm}^2$. The background drops with a factor ∼4 from RB1in&out to RB2in&out and the lowest background is observed in the most shielded station RB3. RB4 shows the same asymmetry between top and bottom chambers as the DT chambers. The ϕ-distribution of the background rates is affected by irreducible noise in the RPC chambers of the order of $\mathcal{O}(1\,\mathrm{Hz/cm}^2)$. As we expect a uniform value of the background rate in all chambers except RB4, an uncertainty band with the width of the RMS is drawn around the mean value.

Figure 19 shows the rate in the CSC as function of the azimuthal angle ϕ. While the inner ring chambers MEx/1 have a symmetric ϕ-distribution, the outermost chambers ME1/3 and MEx/2 ($x = 2, 3, 4$) have a slight modulation in ϕ, that is most expressed in ME1/3 and ME4/2, with highest background at 90° and lowest background at 270°. This modulation is due to the distance to the cavern walls, with chambers being more shielded when close to the cavern floor, and less shielded when at large distance from the cavern ceiling, as we have seen for the DT system. The chambers with highest rate, ME1/1 can be distinguished between the odd and even chambers, which are staggered in the endcap nose: odd chambers are installed in the back and even chambers installed in front. While slightly further away from the interaction point, the odd chambers see slightly higher rates with respect to the even chambers. When analysing the single hit rate per layer, the hit rates are about 10% higher in the last layers of the chamber, which might points to some back-scatter flux from the steel elements of the return yoke.

Figure 20 shows the rate in the endcap RPC as function of the azimuthal angle ϕ. Also here the ϕ-distribution is slightly distorted by remaining irreducible detector noise. The highest rate are observed in RE4/2 (10–15 $\mathrm{Hz/cm}^2$). While background rates are rather uniform in ϕ for RPCs in RE1 and RE2, indicating that they are dominated by prompt background from the interaction point, the backgrounds in RE3 and RE4 are modulated in ϕ, illustrating that they are dominated by cavern background. The distribution of the rates in RE±3/3 and RE±4/2 & RE±4/3 confirm the pattern found in the CSC system for ME3/2 and ME4/2, with a peak at 90° and lowest value at 270°. Given the irreducible noise fluctuations, an uncertainty band with the width of the RMS is drawn around the mean value to guide the eye. A few lower fluctuations in the hit rate are attributed to chambers working in single-gap mode with a 10–25% lower efficiency.

6.3 Average hit rate per chamber

Table 2 shows the single hit rate and the segment rate measured in the DT chambers averaged over ϕ. To illustrate the

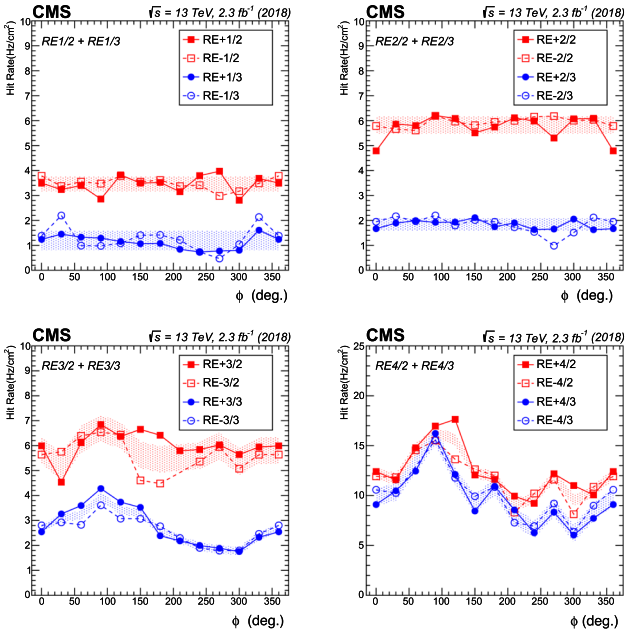

Fig. 20 Hit rate in the endcap RPC as a function of the azimuthal angle ϕ at an instantaneous luminosity of $\mathcal{L} = 10^{34}\,\mathrm{cm}^{-2}\,\mathrm{s}^{-1}$

effect of the background rate due to the radiation in the cavern, also the hit rate and segment rate in a non-shielded top sector of the outermost chambers, MB4/S05, has been shown. The segment rate is a good estimate for the rate of charged particles crossing the chamber, while the single hit rate per layer illustrates the overall rate. The rates are uniform in the chamber, with some exceptional hot spots in the innermost chambers of the outer wheels (W±2/MB1), corresponding to the calorimeter barrel/endcap interface where the material budget is reduced.

Tables 3 and 4 show the hit rate in the barrel and endcap RPC chambers averaged over ϕ. A noticeable reduction can be seen in the external wheels (W±2) between the two chambers belonging to the same station, W±2/RB1in and W±2/RB1out, the latter being shielded by the DT MB1 station that is installed between RB1in and RB1out. Noise in the RPC chambers gives rise to fluctuations in rate when not averaged over a set of chambers, visible when plotted as function of ϕ, see Fig. 18; therefore we use the RMS over all chambers in the same station to estimate the uncertainty. This averaging over ϕ leads to large RMS for RB4 as there is a natural modulation in the rate due to the cavern floor. The single hit rates in the DT and RPC barrel system have the same order of magnitude (few Hz/cm^2 to few tens of Hz/cm^2) and show the same trends: reduction from outer wheels to central wheels, reduction from inner station to third station, and drastic increase in the fourth station. Differences in the rates have to be attributed to the different sensitivity of the DT and RPC chambers to background hits as they are composed of different materials.

Table 5 shows the single hit rate and particle rate in the CSC chambers averaged over ϕ at an instantaneous luminosity of $\mathcal{L} = 10^{34}\,\mathrm{cm}^{-2}\,\mathrm{s}^{-1}$. The particle rate is a good estimate for the background flux, while the single hit rate makes it easier to compare to the single readout layer RPC technology. The particle rate is higher than the single hit rate, as the latter is averaged over 6 layers and only penetrating charged particles like pions and muons provide hits in all six layers, while interactions of neutrals, often giving rise to low-energy electrons result mostly in hits in few layers.

Whereas the RPC and DT chambers in the barrel are attached to each other, cover nearly the same area and are located at the same pseudorapidity, this is not the case for the CSC and RPC chambers in the endcap. Therefore, it is more difficult to compare the rates averaged over the chamber surface. Only RE1/2 and RE1/3 have near identical size and position of ME1/2 and ME1/3. In the second to fourth station, REx/2 and REx/3 correspond mostly with MEx/2, as can be seen in Fig. 1, while for the inner CSC chambers MEx/1, no RPC counterparts were installed. The single hit rates of ME1/2 (4.5 Hz/cm^2) and ME1/3 (1.3 Hz/cm^2) correspond rather well to the rates observed in RE1/2 (3.5 Hz/cm^2) and RE1/3 (1.2 Hz/cm^2). The average rates of the 2$^{\mathrm{nd}}$ and 3$^{\mathrm{rd}}$ ring chambers of the RPCs in the 2$^{\mathrm{nd}}$ to 4$^{\mathrm{th}}$ station have the same order of magnitude of the rates measured in the outer ring CSC chambers: RE2: 3.9 Hz/cm^2 vs ME2/2: 3.0 Hz/cm^2; RE3: 4.3 Hz/cm^2 vs ME3/2: 3.7 Hz/cm^2; and RE4: 12.3 Hz/cm^2 vs ME4/2: 10.3 Hz/cm^2. Considering the different materials and hence the different sensitivity to neutral backgrounds, there is good agreement between the different detection technologies.

Table 6 shows the average single hit rate in the individual layers of the CSC chambers. The hit rates in ME11 are highest for the last layers, which are the layers further away from the interaction point, but closer to the iron yoke of disk 1 (YE1). An increase of about 10 % is observed going from the first to the last layer. The same increase in rate is observed in the ME2/1 chambers that are mounted on the iron yoke of disk 2 (YE2), while for the other chambers, no such effect is observed.

These average single hit rates per chamber can be compared to linear extrapolations based on background measurements performed on Run 1 data taking in 2010. The estimates provided in [2] were based on data taken at a maximum instantaneous luminosity of $1.8 \times 10^{32}\,\mathrm{cm}^{-2}\mathrm{s}^{-1}$ and were scaled up with a factor more than 50. These estimates proved to be rather accurate for the outer ring CSC chambers and outer DT chambers, but were under estimating the rates in the inner ring CSC chambers by a factor 2–3.5. The different behaviour of the scaling can be attributed to changes in the detector geometry from Run 1 to Run 2: the installation of a new beam pipe has given rise to an increase of the rate in low-radius chambers in the endcap, while the shielding disks

Table 2 DT single hit rate and segment rate in the barrel chambers at $\mathcal{L} = 10^{34}\,\mathrm{cm}^{-2}\,\mathrm{s}^{-1}$

	Hit rate (Hz/cm^2)					Segment rate (Hz/cm^2)				
	MB1	MB2	MB3	MB4	MB4/S05	MB1	MB2	MB3	MB4	MB4/S05
W-2	3.37	0.62	0.11	1.69	3.46	5.64	0.63	0.08	1.58	3.71
W-1	1.46	0.27	0.07	1.55	3.18	1.65	0.23	0.05	1.49	3.32
W+0	0.52	0.14	0.06	1.44	3.24	0.67	0.13	0.04	1.40	3.43
W+1	1.39	0.26	0.07	1.63	3.52	1.59	0.22	0.05	1.58	3.78
W+2	3.29	0.61	0.12	1.88	4.13	5.66	0.64	0.08	1.88	4.86
Uncrt	±0.01	±0.01	±0.01	±0.01	±0.05	±0.04	±0.01	±0.01	±0.01	±0.07

Table 3 RPC hit rate in the barrel chambers at $\mathcal{L} = 10^{34}\,\mathrm{cm}^{-2}\,\mathrm{s}^{-1}$

Rate (Hz/cm^2)	RB1in	RB1out	RB2in	RB2out	RB3	RB4
W-2	5.4 ± 0.9	4.4 ± 0.7	1.2 ± 0.8	1.2 ± 0.2	0.3 ± 0.1	3 ± 2
W-1	2.6 ± 0.2	2.0 ± 0.4	0.5 ± 0.1	0.5 ± 0.2	0.1 ± 0.1	3 ± 2
W+0	0.9 ± 0.4	0.8 ± 0.2	0.5 ± 0.1	0.4 ± 0.2	0.3 ± 0.1	3 ± 2
W+1	3.6 ± 0.7	2.1 ± 0.6	0.9 ± 0.2	0.5 ± 0.1	0.3 ± 0.4	3 ± 2
W+2	6.1 ± 0.7	4.5 ± 0.9	1.1 ± 0.3	1.1 ± 0.3	0.4 ± 0.4	4 ± 3

Table 4 RPC hit rate in the endcap chambers at $\mathcal{L} = 10^{34}\,\mathrm{cm}^{-2}\,\mathrm{s}^{-1}$

Rate (Hz/cm^2)		RE1	RE2	RE3	RE4
Negative endcap	RE$-x$/2	3.5 ± 0.2	6.0 ± 0.2	5.6 ± 1.6	11.8 ± 2.4
	RE$-x$/3	1.3 ± 0.5	1.8 ± 0.4	2.6 ± 0.6	15.2 ± 3.2
Positive endcap	RE$+x$/2	3.4 ± 0.4	5.8 ± 0.4	6.0 ± 0.6	12.6 ± 2.8
	RE$+x$/3	1.1 ± 0.3	1.8 ± 0.2	2.8 ± 0.9	9.7 ± 3.1
Average	RE$\pm x$/2	3.5 ± 0.3	5.9 ± 0.3	5.8 ± 1.1	11.2 ± 2.6
	RE$\pm x$/3	1.2 ± 0.4	1.8 ± 0.3	2.7 ± 0.7	12.8 ± 3.1

Table 5 CSC single hit and particle rates for the different chamber types at $\mathcal{L} = 10^{34}\,\mathrm{cm}^{-2}\,\mathrm{s}^{-1}$

Rate (Hz/cm^2)	ME1/1	ME1/2	ME1/3	ME2/1	ME2/2	ME3/1	ME3/2	ME4/1	ME4/2
Single hit rate	145.74	4.54	1.25	70.72	3.00	47.15	3.72	60.8	10.33
Uncertainty	±0.14	±0.03	±0.04	±0.12	±0.02	±0.14	±0.02	±0.2	±0.02
Particle rate	378.1	13.1	3.9	233.4	9.8	143.6	13.1	163.1	34.2
Uncertainty	±0.5	±0.1	±0.2	±0.5	±0.1	±0.5	±0.1	±0.7	±0.1

Table 6 CSC Single hit rate (Hz/cm^2) for the various layers at $\mathcal{L} = 10^{34}\,\mathrm{cm}^{-2}\,\mathrm{s}^{-1}$

Layer	ME1/1	ME1/2	ME1/3	ME2/1	ME2/2	ME3/1	ME3/2	ME4/1	ME4/2
1	143.5	4.7	1.2	66.2	3.03	45.0	3.87	59.0	10.67
2	145.5	4.7	1.2	67.4	3.01	46.1	3.89	59.9	10.59
3	146.5	4.5	1.3	67.5	3.08	45.2	3.77	58.5	10.32
4	151.4	4.5	1.6	67.0	2.91	46.2	3.58	58.3	10.27
5	153.5	4.4	1.5	71.2	3.08	45.4	3.62	57.9	10.08
6	158.9	4.5	1.4	73.3	2.90	45.3	3.58	57.6	10.03
Uncrt	±0.3	±0.1	±0.1	±0.2	±0.05	±0.3	±0.04	±0.4	±0.05

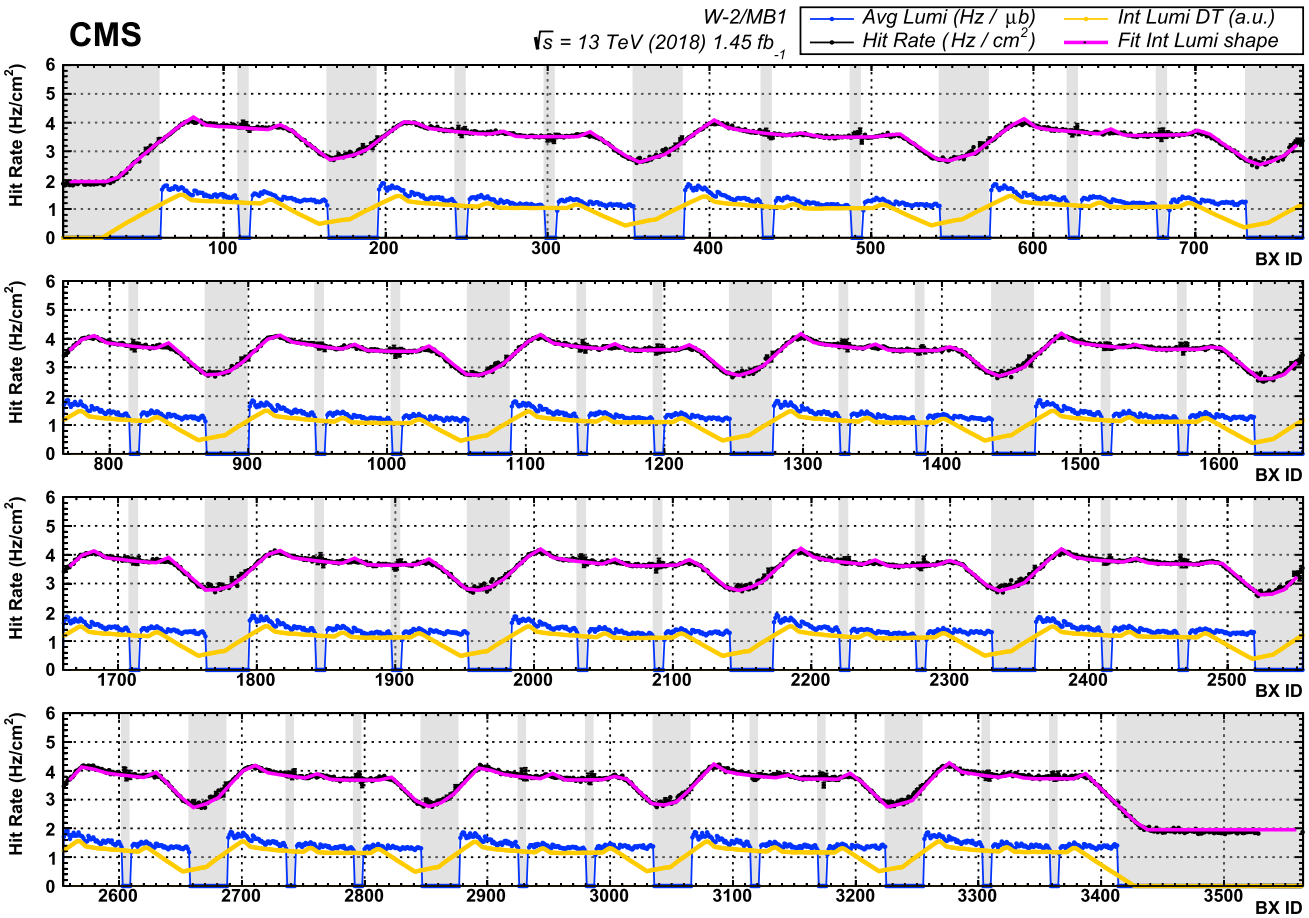

Fig. 21 Hit rate in the MB1 chambers in Wheel -2 as a function of bunch crossing along the LHC orbit (black markers) at an instantaneous luminosity of $\mathcal{L} = 10^{34}\,\mathrm{cm}^{-2}\,\mathrm{s}^{-1}$. The instantaneous luminosity per BX (in Hz/μb) averaged over the entire fill period is shown with blue markers. The yellow line (L_{DT}) shows the (normalised) integral of this luminosity over the 50 BX wide readout window. The observed hit rate (black markers) are fitted (magenta) with the (yellow) function $L_{DT}(BX)$

YE4 have reduced the rates in the high-radius chambers of the endcap.

7 Hit rate analysis

Given the pattern of colliding and non-colliding proton bunches of the LHC, the rates in the detectors are not expected to be constant during the orbit. One would expect to observe higher rates during colliding bunches, due to particles born in the collisions and prompt background, while in the gaps between colliding bunches one expect to observe the delayed background due to collisions happened few μs to hundreds of ms earlier. This picture however is altered by the instrumental effects such as detector time resolution or the lack of bunch crossing assignment to individual hits in the DT system.

7.1 Drift tubes

In the DT system signals are discriminated and characterised by the wire number and the TDC timestamp. The drift time range corresponds to ∼16 BX, and, in order to collect all the hits belonging to a track, a readout window of 50 BX is used. Therefore any single DT hit cannot be uniquely assigned to any bunch crossing. However, the hits produced by a same track in several layers are fitted with a linear function that includes a third free parameter: this is used to determine the track crossing time with respect to the triggering BX.

The effect of the readout window is visible in the structure of the DT rate as function of time (BXid within the LHC orbit), smearing the expected sharp rise in rate from non-colliding bunches to colliding bunches (fast rising/falling edges in the blue curve) over a time of roughly 50 BX (slow rising/falling edges in the yellow curve). Figure 21 shows the rate observed in DT chambers of Wheel -2 inner station (W-2/MB1) that are mostly subject to prompt background,

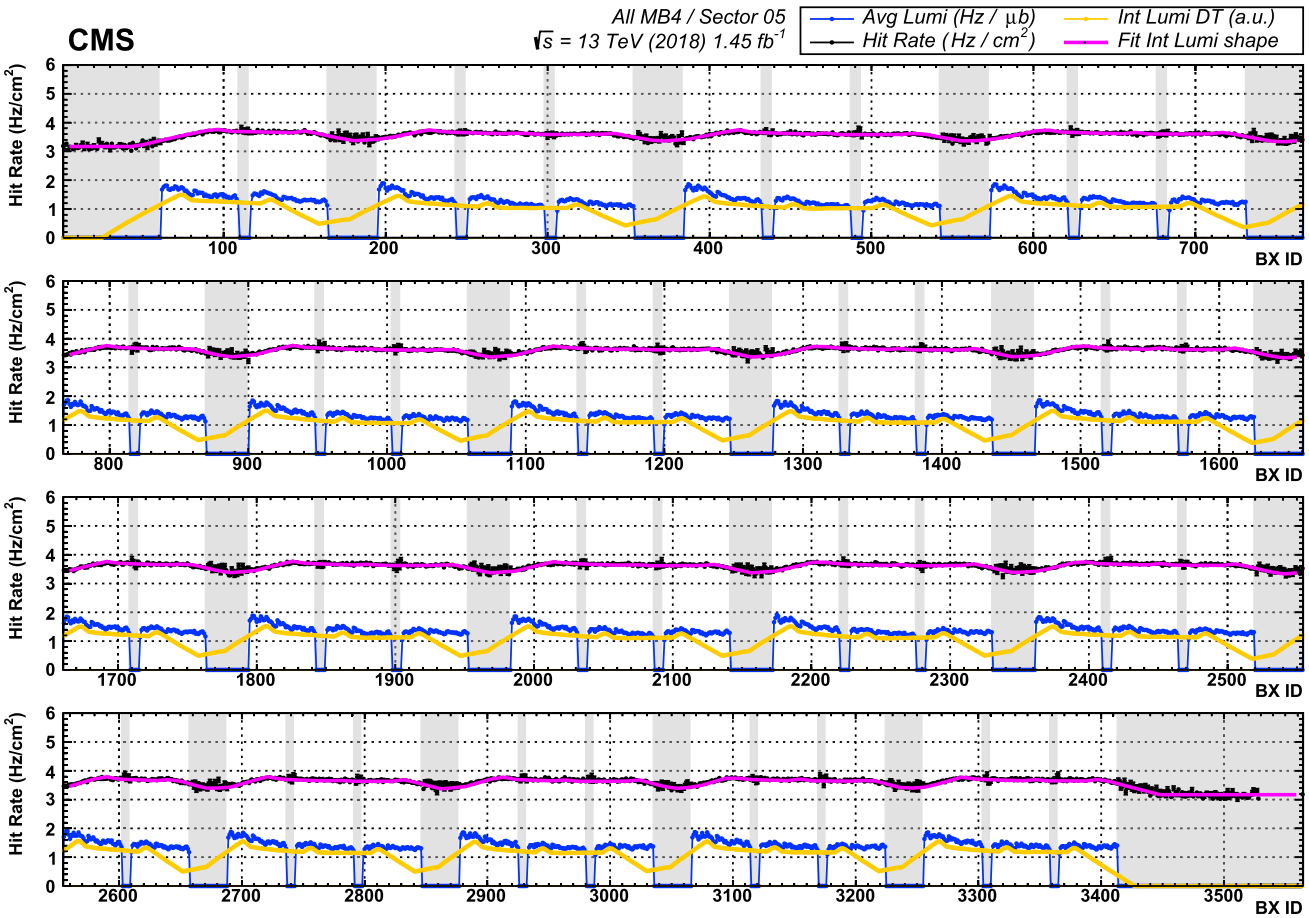

Fig. 22 Hit rate in the MB4/S05 top sector chambers of all five wheels as a function of bunch crossing along the LHC orbit (black markers) at an instantaneous luminosity of $\mathcal{L} = 10^{34}\,\mathrm{cm}^{-2}\,\mathrm{s}^{-1}$. The instantaneous luminosity per BX (in Hz/μb) averaged over the entire fill period is shown with blue markers. The yellow line (L_{DT}) shows the (normalised) integral of this luminosity over the 50 BX wide readout window. The observed hit rate (black markers) are fitted (magenta) with the (yellow) function $L_{DT}(BX)$

while Fig. 22 shows the rate observed in the DT chambers of a top sector of the outer station (MB4/S05) which is dominated by delayed background. For technical reasons (alignment of optical links) no triggers are allowed in BX 3529-3563. Therefore, there are no hit rate measurement for those 35 BXs at the end of the orbit (the entire orbit is 3564 BX, see Sect. 2).

In Fig. 21 the structure of the colliding trains of proton bunches is clearly visible, while this is not the case anymore for outermost DT, see Fig. 22, where the background is dominated by the long-lived neutron background. Both figures show the average instantaneous luminosity for each BX id (blue curve) as measured by the CMS luminosity monitors as well as the integrated luminosity seen in a moving 50 BX readout window (yellow curve, arbitrary units) and the actual hit rate in the DT chambers (black markers). The curve of the integrated luminosity seen in a moving 50 BX window around the BX-id of the trigger provides a good shape to describe the observed hit rate in the detector. The function used is:

$$R(i) = p_0 + p_1 \cdot L_{DT}(i - p_2) \tag{6}$$

with

$$L_{DT}(i) = \sum_{j=-13}^{+36} \mathcal{L}(i+j). \tag{7}$$

$L_{DT}(i)$ is the *"effective luminosity"* that contributes to the total amount of hits readout at that given bunch crossing, $\mathcal{L}(i)$ is the instantaneous luminosity delivered by the LHC and measured with the various CMS luminometers (see Sect. 2), and i is the bunch crossing in the LHC orbit, ranging from 1 to 3564. One can see in Figs. 21 and 22 that the instantaneous luminosity (blue curve) is not equal in all colliding bunches.

The instantaneous luminosity is highest in the first colliding bunch after a series of non-colliding bunches. The reduced luminosity in subsequent colliding bunches is due to the electron-cloud effects that increases the emittance (ε)

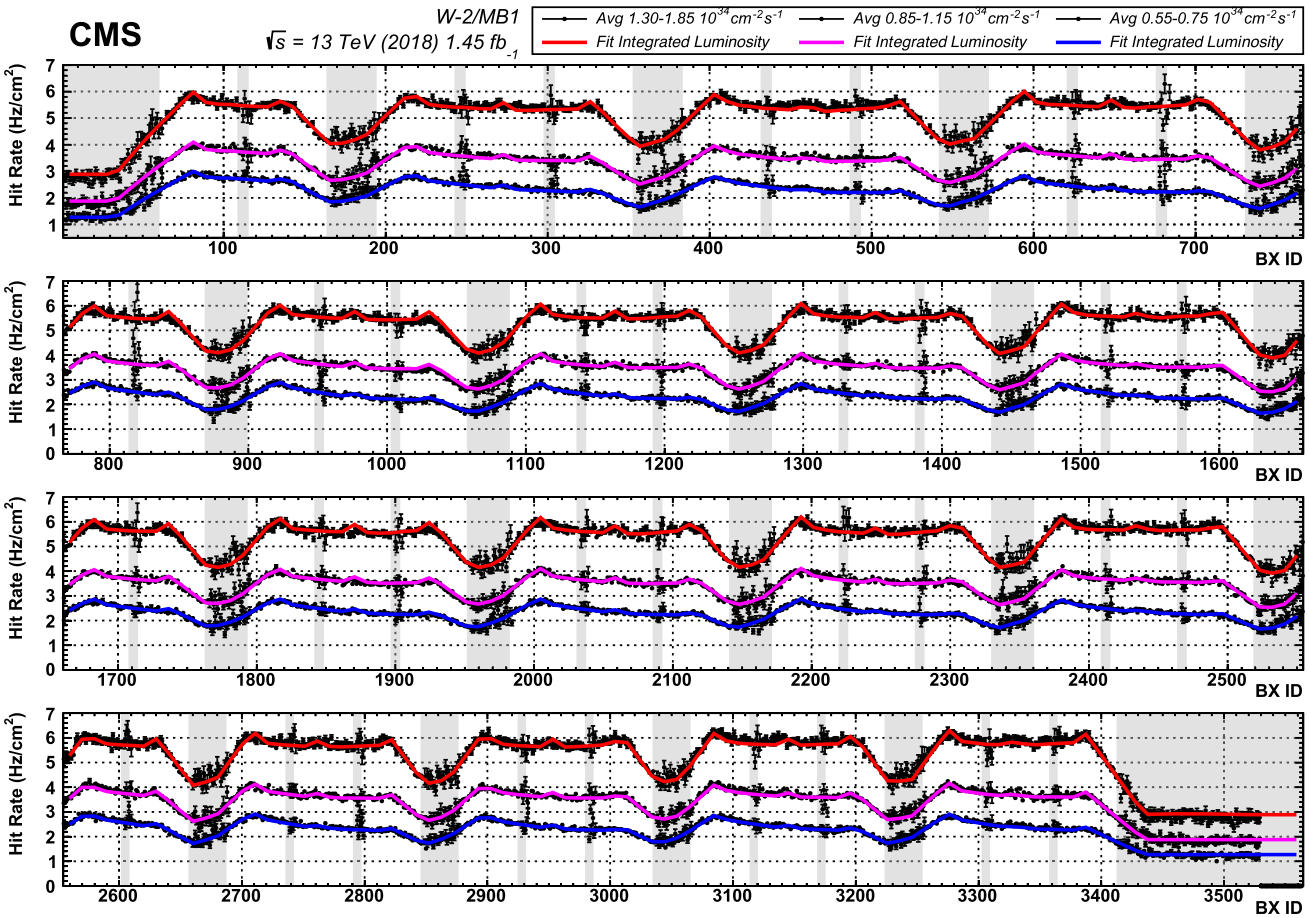

Fig. 23 Hit rate in the MB1 chambers in wheel-2 as a function of bunch crossing along the LHC orbit in three different intervals with instantaneous luminosity $1.30 < \mathcal{L} < 1.85 \cdot 10^{34}\,\mathrm{cm}^{-2}\,\mathrm{s}^{-1}$ (begin of fill—red fit), $0.85 < \mathcal{L} < 1.15 \cdot 10^{34}\,\mathrm{cm}^{-2}\,\mathrm{s}^{-1}$ (middle of fill—magenta fit) and $0.55 < \mathcal{L} < 0.75 \cdot 10^{34}\,\mathrm{cm}^{-2}\,\mathrm{s}^{-1}$ (end of fill—blue fit)

and reduces the number of protons (N_i) of those bunches (see Formula 1 in Sect. 2).

The resulting fit (magenta curve) to the observed hit rate is of high quality ($\chi^2/\mathrm{ndf} < 2$): from it the rates due to prompt background and delayed backgrounds can be extracted. The parameter p_0 represents the constant component of the hit rate (**D**, for the delayed background), while the average prompt component (**P**, for prompt background), is: $P = p_1 \cdot \langle L_{DT}(x) \rangle$, and the average is made over a lumi section. A small delay $p_2 = 8\,\mathrm{BX}$ is observed, which corresponds to the average drift time of randomly distributed hits in a DT cell.

Both the prompt component **P** as the delayed component **D** depend on the instantaneous luminosity $\mathcal{L}$. To compute $\mathbf{D}(\mathcal{L})$ and $\mathbf{P}(\mathcal{L})$, the rate was measured in three different intervals of $\mathcal{L}$, corresponding to the begin of the fill ($1.30 < \mathcal{L} < 1.85 \cdot 10^{34}\,\mathrm{cm}^{-2}\,\mathrm{s}^{-1}$), the middle of the fill ($0.85 < \mathcal{L} < 1.15 \cdot 10^{34}\,\mathrm{cm}^{-2}\,\mathrm{s}^{-1}$) and the end of the fill ($0.55 < \mathcal{L} < 0.75 \cdot 10^{34}\,\mathrm{cm}^{-2}\,\mathrm{s}^{-1}$). During a fill, electron-cloud effects cause the instantaneous luminosity per bunch to fall off more rapidly for proton bunches at the end of the bunch trains, therefore the average luminosity per bunch was calculated for each of the three luminosity intervals, leading to slightly different $L_{DT}(i)$ fit functions. Figure 23 shows the average hit rate in the DT chambers of Wheel -2 inner station (MB1) for the the thee different luminosity intervals, along with the fitted $L_{DT}(i)$ functions: red curve the fit to the hit rates at the beginning of the fill, magenta curve during the middle of the fill and blue curve at the end of the fill.

The fit parameters p_0 and p_1 were extracted for the three different instantaneous luminosity intervals, both for the hit rate in the inner station chambers of Wheel -2 (W-2/MB1) as for all outer station chambers of sector 5 (MB4/S05). For each fit $L_{DT}(i)$ was normalised to one ($\langle L_{DT}(i) \rangle = 1$), so that the dependence of **P** on the instantaneous luminosity, $\mathcal{L}$, is fully expressed by p_1: $\mathbf{P}(\mathcal{L}) = p_1(\mathcal{L})$ while $\mathbf{D}(\mathcal{L}) = p_0(\mathcal{L})$. As a consistency check of the method, the results for **D** and **P** can then be plotted as a function of $\mathcal{L}$ and compared with direct measurements of hit rate versus instantaneous luminosity.

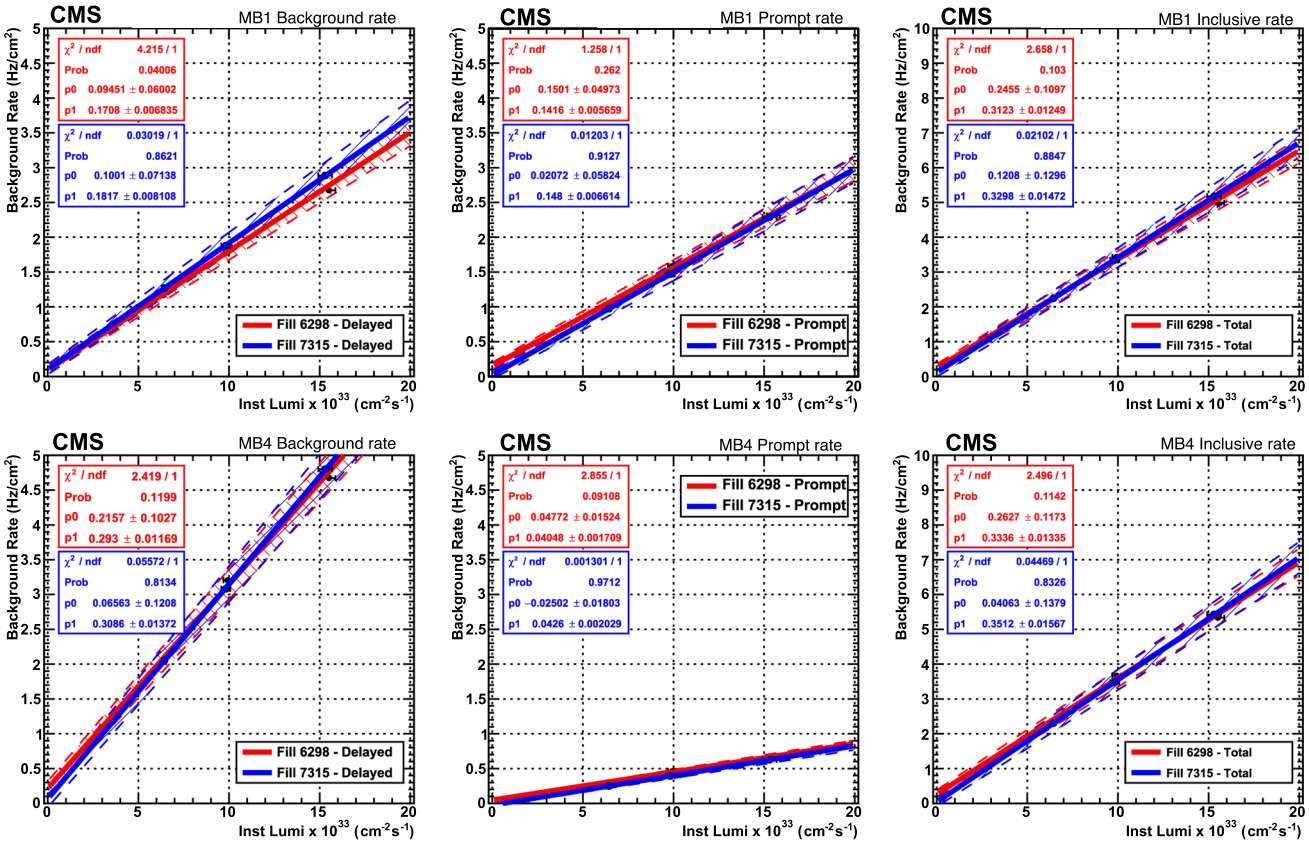

Fig. 24 Prompt and delayed components of DT background, as obtained from the fits of data to LHC per-BX luminosity. This figure shows two regions with high background: the MB1 chambers at high $|\eta|$ and the MB4 top sector (S05) chambers. Each point is the result of a fit. These points lay on a straight line with negligible intercept for both components. The prompt background (middle) dominates in the MB1 chambers, while the delayed background (left) dominates in the MB4/S05 chambers. The total rate is obtained through the sum of the two components (right)

Figure 24 shows the secondary/delayed background rate (left), the prompt rate (middle) and the total rate (right) for Wheel-2/MB1 chambers (top) and RB4/S05 chambers (bottom). Two fills with different filling schemes were analysed: Fill 6298 with 1866 colliding bunches ('8b4e-BCS scheme') recorded during 2017; and Fill 7315 with 2544 colliding bunches ('BCMS scheme') recorded during 2018. The figure shows that separate analysis of prompt and delayed background components naturally removes the effects created by the long readout window and by different fill schemes, in fact the fitted curves for Fill 6298 (red) and Fill 7315 (blue) agree within uncertainties. The figure shows us that, as expected, the secondary background is larger in MB4/S05 than in W-2/MB1; while primary background is larger in W-2/MB1 than in MB4/S05 chambers. Total rates are compatible with previous measurements: the slope of a linear fit to the MB4/S05 data is 0.35 (-), while the slope of a linear fit to the W-2/MB1 rate is 0.33 (-) and both have negligible intercepts. The prompt **P** contribution to the total MB4/S05 rate is ∼10%, the remaining 90% is due to delayed background, while the prompt **P** contribution to the total W-2/MB1 rate is ∼40%, and ∼60% is due to the delayed background.

7.2 Resistive plate chambers

RPCs have a time resolution of 1.5–2 ns. Therefore, they have excellent bunch crossing identification. The hits of the RPC system are registered in a time window of [-3,+2] BX around the central BX assigned to the trigger and can be deconvoluted to the original BX-id inside the orbit. Figure 25 shows the rate along the LHC orbit averaged over all Wheel-2/RB1in chambers at an instantaneous luminosity of $\mathcal{L} = 10^{34}\,\mathrm{cm}^{-2}\,\mathrm{s}^{-1}$.

The precise bunch crossing assignment shows variations in the hit rate in the detector by as much as 2 Hz/cm^2 in colliding bunches, which can be explained by bunch-to-bunch variations of the luminosity. To reduce the statistical uncertainty the hit rate in non-colliding bunches was averaged over multiple bunch crossings. The hit rate is studied separately in 4 different categories: colliding bunches, short and long non-

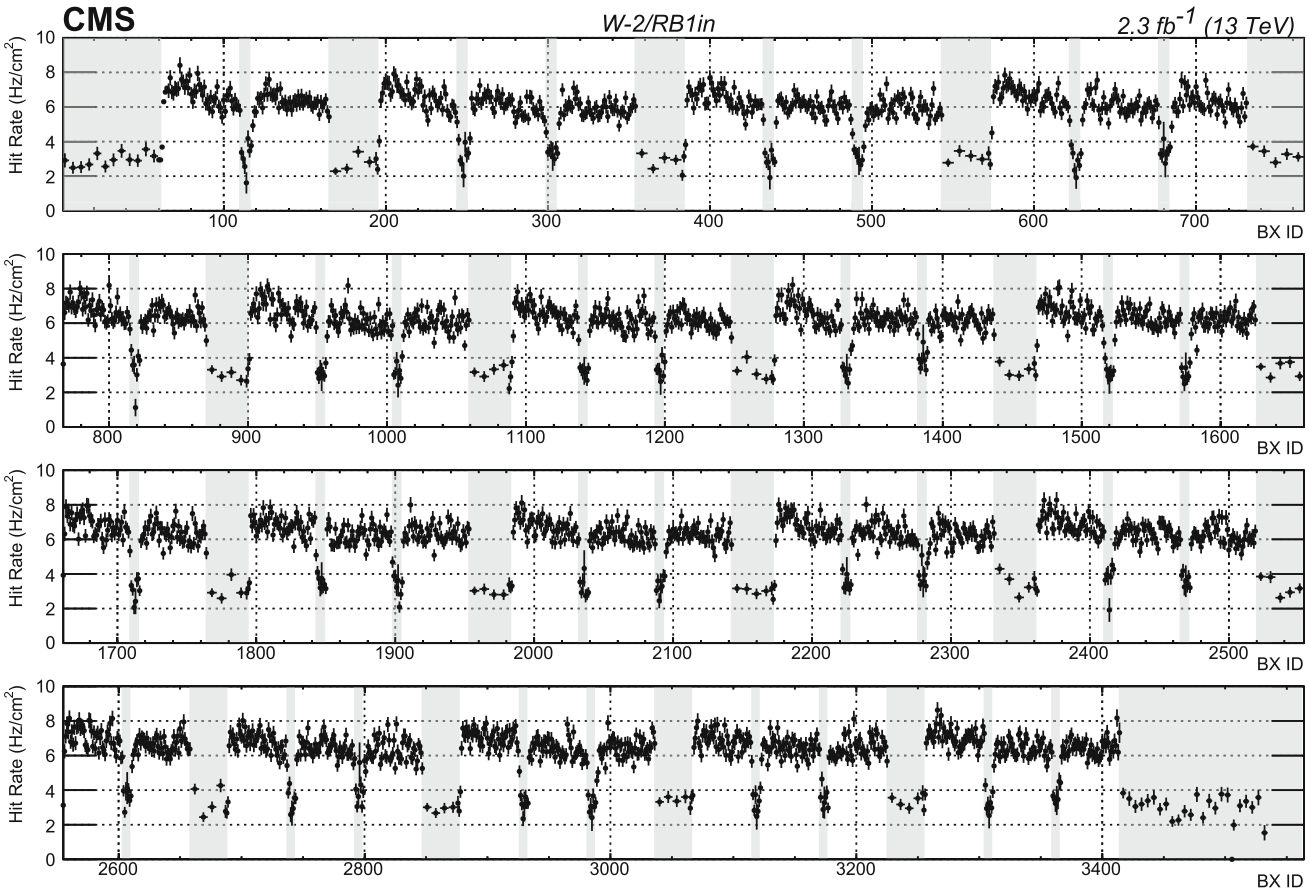

Fig. 25 Hit rate in RB1in of Wheel-2 as function of the bunch crossing within the LHC orbit

colliding bunch gaps (resp. 7 BX and 31 BX long) between the bunch trains, non-colliding bunches before the first colliding bunch in the orbit and non-colliding bunches in the abort gap. While the separation between the third and fourth category is arbitrary, and is populated by delayed background as for the non-colliding bunches between bunch trains, for the final analysis they are grouped in a single non-colliding bunches group.

Figure 26 (top) shows the hit rate in colliding bunches (R_{col}, green filled circles), non-colliding bunches between bunch trains (R_{gap}, red filled squares), non-colliding bunches in the abort gap (R_{a}, blue open circles) and non-colliding bunches before the first colliding bunch in the orbit (R_{pb}, cyan open squares, *pre-beam*). All components behave linear with respect to the instantaneous luminosity, with negligible offset. The background in colliding bunches is the highest as it measures both hits due to neutron background and promptly induced hits. There is a noticeable decay of the delayed background as the hit rate in 7-to-31 BX bunch train gaps is higher than the average hit rate in the abort and pre-beam gaps and the hit rate in the pre-beam gap is slightly lower with respect to the abort gap. Grouping all non-colliding bunches together a precise measurement of the delayed neutron background can be measured. Subtracting this delayed background from the hit rate observed in the colliding bunches one obtains the prompt component of the background. The inclusive, delayed and prompt rates are given by:

$$R_{\text{incl}} = \frac{N_{\text{col}} R_{\text{col}} + N_{\text{gap}} R_{\text{gap}} + N_{\text{a}} R_{\text{a}} + N_{\text{pb}} R_{\text{pb}}}{N_{\text{col}} + N_{\text{gap}} + N_{\text{a}} + N_{\text{pb}}} \tag{8}$$

$$R_{\text{delay}} = \frac{N_{\text{gap}} R_{\text{gap}} + N_{\text{a}} R_{\text{a}} + N_{\text{pb}} R_{\text{pb}}}{N_{\text{gap}} + N_{\text{a}} + N_{\text{pb}}} \tag{9}$$

$$R_{\text{promt}} = R_{\text{col}} - R_{\text{delayed}} \tag{10}$$

where, for the luminosity production fill scheme of 2018: $N_{\text{col}} = 2544$, the number of colliding bunches; $N_{\text{gap}} = 808$, the number of bunches in the various bunch train gaps; $N_{\text{a}} = 150$, the number of bunches in the abort gap; and $N_{\text{pb}} = 62$ the number of bunches in the orbit before the first colliding bunch. This figure can be simplified grouping all non-colliding bunches together. Figure 26 (bottom) shows the dependency of the prompt (yellow dot-dashed line) and delayed background (magenta dashed line) as function of the instantaneous luminosity, together with the total background hit rate weighted over the number of colliding bunches (black line). For the innermost chambers of the

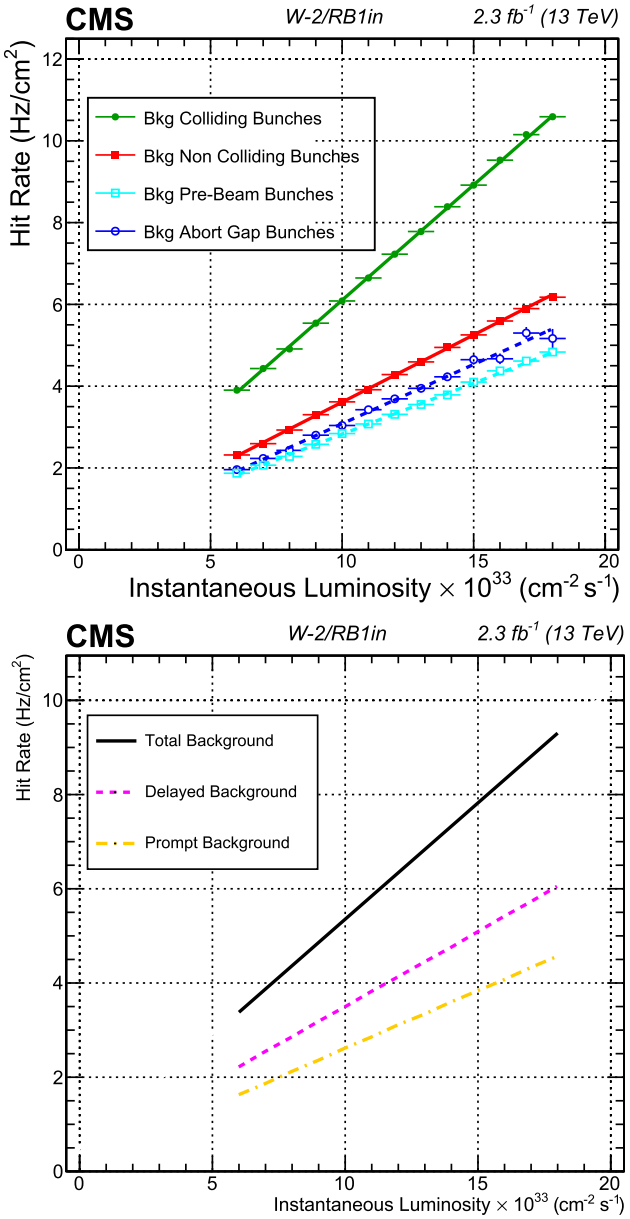

Fig. 26 Hit rate as function of instantaneous luminosity for RPC Wheel-2/RB1in chambers. Top: the rate in colliding bunches (green circles) and non-colliding bunches (red squares) in short and long bunch gaps as well as the rate in the first 61 BX of the orbit (*pre-beam gap*) and last 150 BX of the orbit (*abort gap*). Bottom: the total background (in colliding bunches) as function of the instantaneous luminosity, together with the contribution of primary background (yellow dashed line) and the delayed background (magenta dashed line)

barrel external wheels (Wheel -2/RB1in), the delayed background is measured to be ∼25% higher with respect to the prompt background, which is in line with what we observed in the DT chambers of Wheel-2/MB1 discussed earlier. This analysis is applied to all chamber types and results are presented in Sect. 7.4. The peak rate occurs during colliding bunches and it is about 15% higher w.r.t. the average rate over the entire orbit.

7.3 Cathode strip chambers

The CSCs have a wire spacing of 2.5–3.2 mm leading to an expected time resolution of ∼ 8 ns per layer. With this time resolution a bunch crossing can be assigned to each individual CSC wire hit, although a fraction of ∼10% of bin migration (in time particle assigned BX = −1 or +1) has to be expected. Figure 27 shows the particle hit rate in the ME1/1 chambers as function of the BX-id at $\mathcal{L} = 10^{34}\,\mathrm{cm}^{-2}\,\mathrm{s}^{-1}$. The measured rate in the first bunch and in the last bunch of each bunch train is lower with respect to the rest, which is caused by the smearing due to the time resolution of the detectors.

Examining the background rate in the abort gap, one can observe a slight decrease of the rate from ∼200 Hz/cm^2 to less than 150 Hz/cm^2 just before the first colliding bunches in the orbit. Since there are several interaction mechanisms for neutrons, no firm conclusions can be drawn from a fit with a single exponential decay. No data is read out for $3529 \leq$ BX-id ≤ 3563 and measurement of the background rate for those BX is missing. The chamber local trigger requirement to initiate detector readout produces a good statistical precision to measure the background in the colliding bunches. Sixteen BX wide readout window provides also a good precision to measure the background in the small 7 BX gaps between bunch trains and at the beginning and the end of the larger 31 BX gaps. The statistical precision in the middle of the 31 BX gaps as well as in the abort gap and in the non-filled bunch slots before the first bunch train, is reduced by this local trigger requirement. One can also observe that because of the finite time resolution (and hence bin migration) the measurement of the rate in the colliding bunches appears smoother with respect to the rates measured in the RPC system where precise BX-id is available.

Figure 28 shows the particle rate as function of the instantaneous luminosity for ME1/1 and ME4/2 chambers. For ME1/1 the rate in the colliding bunches (orange triangle markers) is about 20% higher than the inclusive rate (blue circle markers), which is the average over the orbit taking into account also the rate in the non-colliding bunches (green square markers).

The rate in the colliding bunches and in the non-colliding bunches are to a good extend proportional to the instantaneous luminosity. The rate in non-colliding bunches is delayed background and the prompt background in colliding bunches can be extracted from the data by subtracting the rate in the non-colliding bunches from the rate in the colliding bunches. As can be seen from Fig. 28 the CSC background rates are not exactly linear with respect to the instantaneous luminosity. Moreover, the extrapolation of the linear part of the curves shows a considerable intercept at zero luminos-

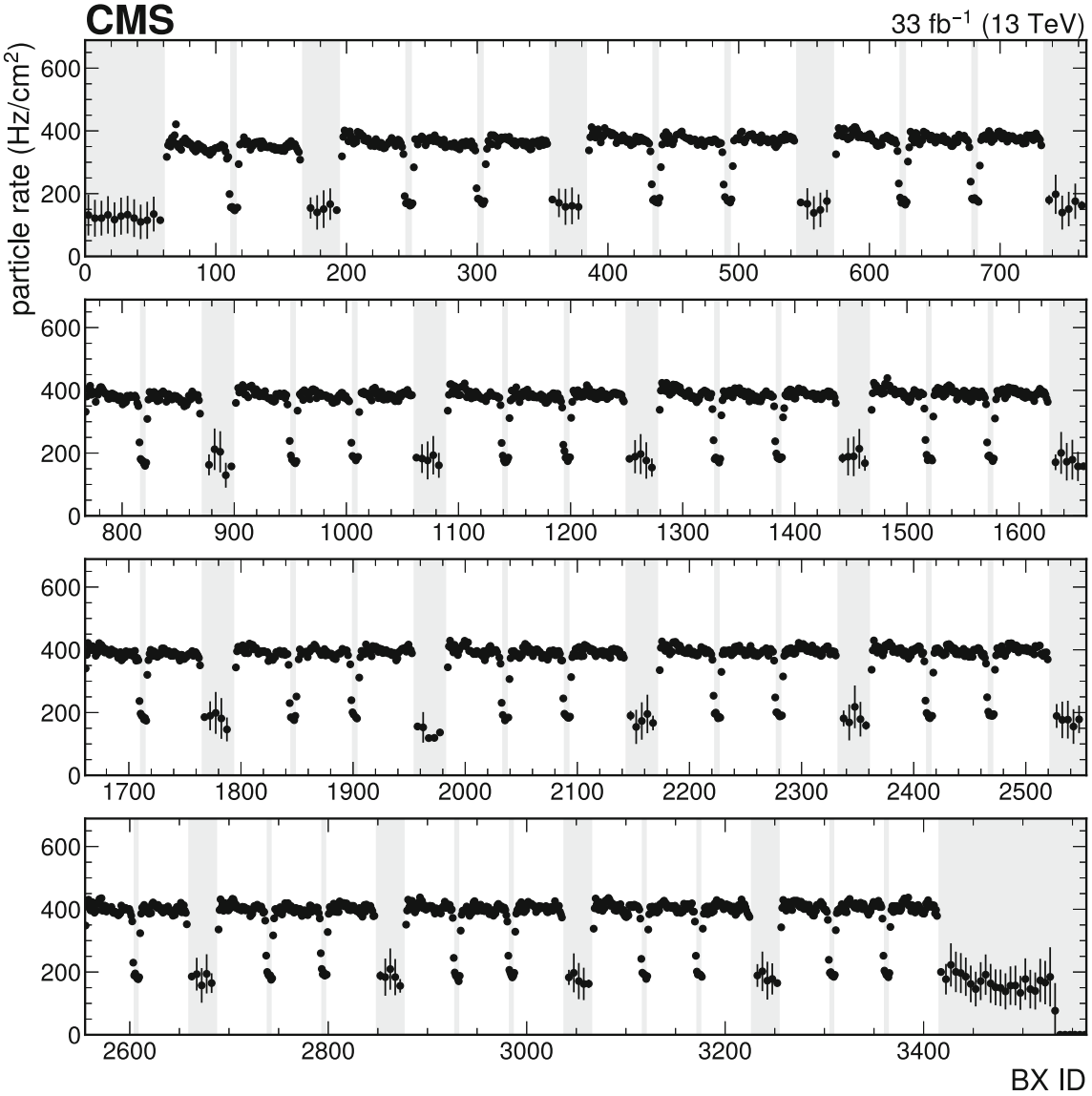

Fig. 27 Particle rate in the ME1/1 chambers as function of the bunch crossing within the LHC orbit at $\mathcal{L} = 10^{34}\,\mathrm{cm}^{-2}\,\mathrm{s}^{-1}$. To reduce the statistical uncertainty the particle rate in the non-colliding bunches was averaged over multiple bunch crossings. The grey shaded area indicate the non-colliding bunches of the LHC fill scheme

ity. This feature is likely caused by induced radioactivity of CMS structural components due to the harsh radiation environment. At the beginning of a new fill the level of induced radioactivity is usually smaller than at the end of a fill.

7.4 Prompt and delayed hit rate

In this paragraph we will present the prompt and delayed rate as function of the pseudorapidity and azimuthal angle in the muon detector. Figure 29 (top) shows the rate of prompt and delayed background as function of η, for all MB1 chambers (left) and for the five MB4 chambers of the non shielded sector 5 at the top of the muon spectrometer (right). In the MB1 chambers the prompt and neutron background have equal contribution to the total background in the central wheel, while for the external wheels the fraction of background due to neutrons is larger than the prompt background. In the MB4 chambers the background is dominated by the neutron background, the prompt background being only 0.5 Hz/cm^2 maximally. Where the prompt background is symmetric in η, the delayed neutron background is lower for the negative side, because the location of the shaft at the negative side reduces the neutron flux. Figure 29 (bottom) shows the rate of prompt and delayed background for RB1in (left) and RB1out (middle) chambers and for the five RB4 chambers of the non-shielded sector 3. For the RB4 chambers Sector

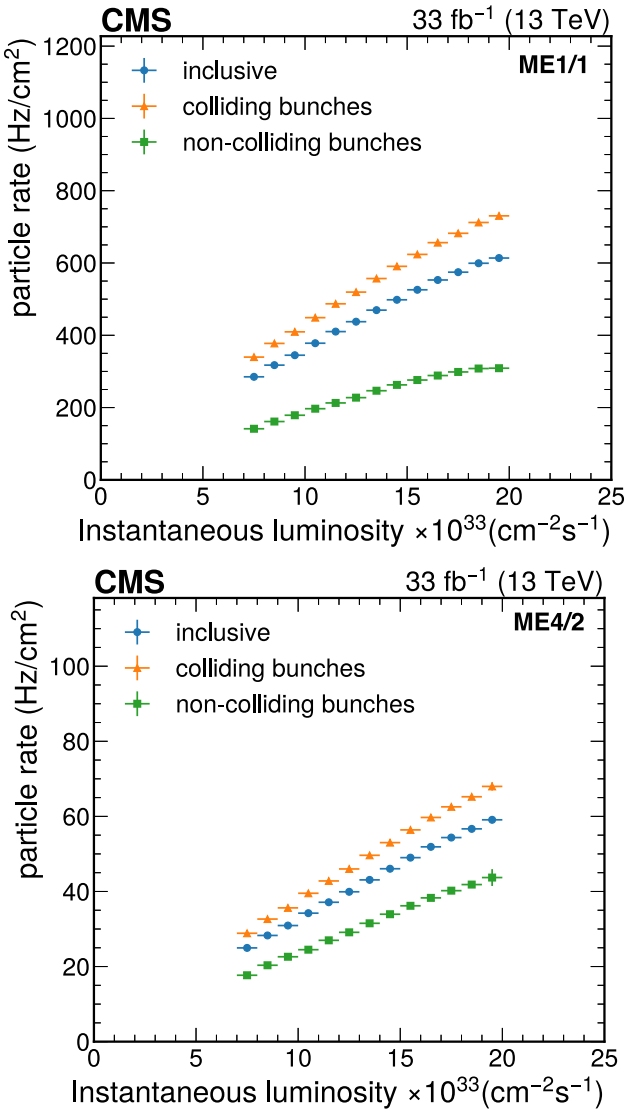

Fig. 28 Particle rate as function of the instantaneous luminosity for ME1/1 (left) and ME4/2 (right) chambers: rate in colliding bunches (orange triangles) and non-colliding bunches (green squares) and the inclusive rate when integrated over the entire LHC orbit (blue circles)

3 was preferred over sector 5 as a few RB4/S05 chambers were excluded from the analysis, while sector 3 is symmetric to sector 5 and both have the same rate. The analysis of the DT and RPC system are rather good agreement with each other, pointing to a ∼60 % delayed and ∼40 % prompt background contributions for MB1 and RB1 chambers, and ∼90 % delayed and ∼10 % prompt background contributions for the top MB4 and RB4 chambers.

Figure 30 shows the single layer hit rate in the various CSC chambers as function of $|\eta|$: the blue markers show the inclusive hit rate averaged over the entire orbit, while the orange and green markers show the prompt and delayed components of the background. The top plots show the background in the outermost CSC chambers, the bottom plots the background in the inner CSC chambers. In ME1/1 the background is completely dominated by the prompt component, whereas in ME2/1 and ME3/1 the prompt and delayed component have about equal contribution to the total background rate over the entire $|\eta|$ range. In ME4/1 the contribution of the prompt background increases with η, and only at $\eta = 1.85$ contributions from prompt and delayed are nearly equal. This picture is confirmed in the outer chambers of the fourth station, ME4/2, where prompt and delayed background have equal contribution at $\eta = 1.5$, after which the delayed component becomes dominating for decreasing η, where the chamber is more exposed to the background from the neutrons in the cavern. The delayed background is also dominant in the outermost chambers of the second and third station, ME2/2 and ME3/2, with significant increases towards the low-η side of the chambers that are exposed to the neutrons of the cavern, whereas in the first station the contribution of prompt and delayed background is about the same.

Figure 31 shows the inclusive, prompt and delayed background for both the CSC and RPC system. The top plots show the inclusive single-layer hit rate, while the second and third row show the the prompt and delayed background hit rate in a single layer. Overall one can observe that the backgrounds in the RPC and CSC system, although made of different materials, follow the same functional forms. The largest discrepancy is found in the fourth station, where the RE4/2 and RE4/3 RPCs are installed close to the concrete YE4 shielding disk, and observe larger delayed background and reduced prompt background with respect to their CSC ME4/2 neighbours.

8 Conclusions

Collision-induced backgrounds in the CMS experiment are constituting the dominant background in the muon detector. Data recorded during Run 2, at a centre-of-mass energy $\sqrt{s} = 13\,\text{TeV}$, has been analysed to understand the background rate in the various locations of the muon detector. The instantaneous luminosity during the LHC fills, varied from 0.6 to 2.2×10^{34} cm^{-2}s^{-1}, with an average of $\sim 1 \times 10^{34}\,\text{cm}^{-2}\text{s}^{-1}$. Background rates have proven to be linear in this luminosity range and rates in CSC, DT and RPC detectors have been reported at $\mathcal{L} = 10^{34}\,\text{cm}^{-2}\text{s}^{-1}$. The rates measured in the various detectors in the same location agree among each other, and the variation of the background rate as function of η and ϕ agree with the shapes found in simulations. Average rates for the different chamber types have been reported. The muon detectors in the barrel register a background rate of few Hz/cm^2, well in agreement with simulations and estimates made at the time of the design of CMS. The background rate in the muon detectors installed

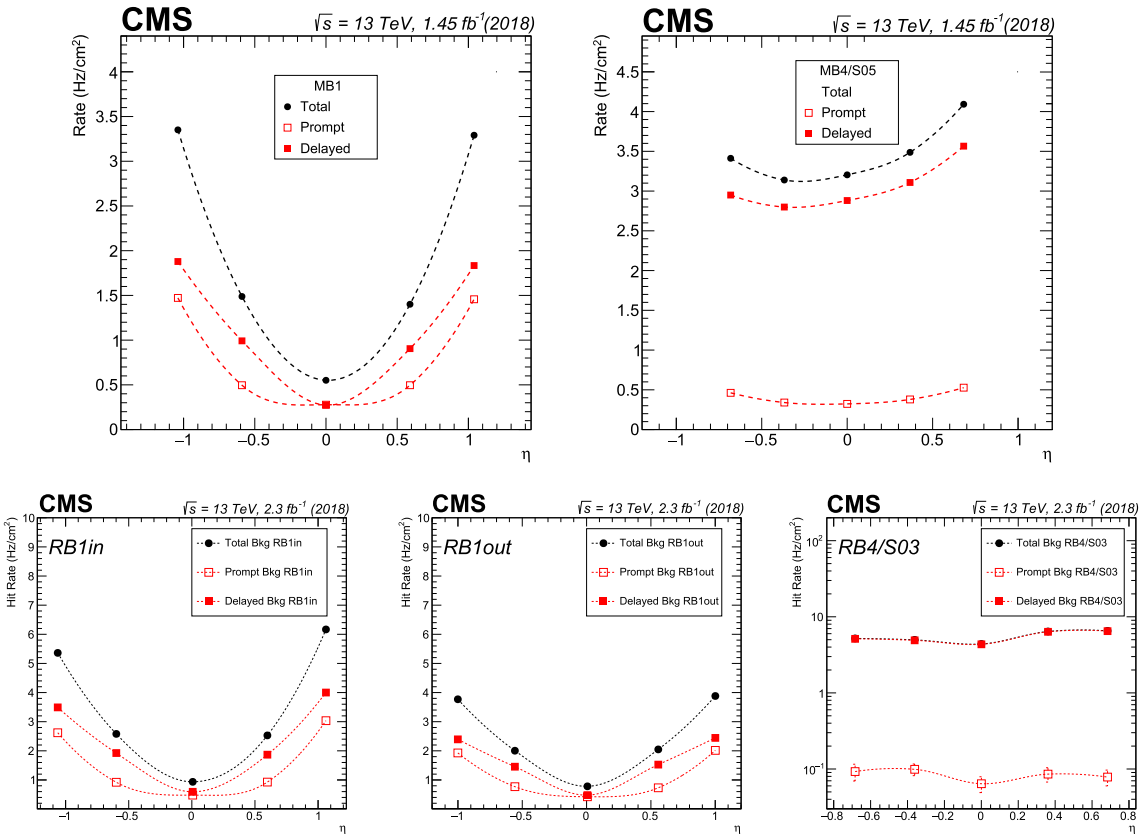

Fig. 29 Rates of prompt and delayed components, and total background, at $\mathcal{L} = 10^{34}\,\mathrm{cm}^{-2}\,\mathrm{s}^{-1}$, as a function of pseudorapidity. Top: all MB1 chambers (left) and the five MB4/S05 chambers (right). Bottom: RB1in (left), RB1out (middle), and five RB4/S03 chambers (right)

in the endcap ranges from few Hz/cm^2 to few hundreds of Hz/cm^2, a factor two to five higher with respect to the simulation predictions made during the design. These rates justify the ongoing efforts to upgrade the muon detector for HL-LHC and the efforts to improve the shielding in the forward region of CMS.

Analysing the rates as function of bunch crossing identification within the LHC orbit has allowed the separation of the "*prompt*" component, that consists of hadron punch through and shower leaks, from the "*delayed*" component that originates from the thermal neutron gas that is built up during collisions in the experimental cavern. The external muon chambers in the barrel (MB4, RB4) are most affected and about 90% of the background rate can be attributed to thermal neutrons. The external muon chambers in the endcap (ME4/2 and RE4/3) are similarly affected, but have also a "*prompt*"contribution from high-energy particles emitted from the forward shielding. The highest rates are observed in the endcap chambers that are closest to the beamline.

Muon detector ageing is driven by the total rate seen by the detectors. A deep and coherent understanding of the background origins and evolution is necessary to predict the rates to be expected at High-Luminosity LHC, both in terms of detector longevity, rate-capability and muon detection and reconstruction performance. The Phase-2 upgrade will drastically change the CMS experiment, with a new beampipe, tracker and endcap calorimeters. The instantaneous luminosity will be increased with a factor 2.5–4. However, background rates cannot be scaled up from the measurements of Run 2 data, because of changes in the CMS construction components. The combination of the Run 2 measurements with Run 2 and Phase-2 simulations will increase the confidence in background predictions for High-Luminosity LHC. Furthermore measurement techniques have been explored that will be used for precise measurement and monitoring of the background during Run 3.

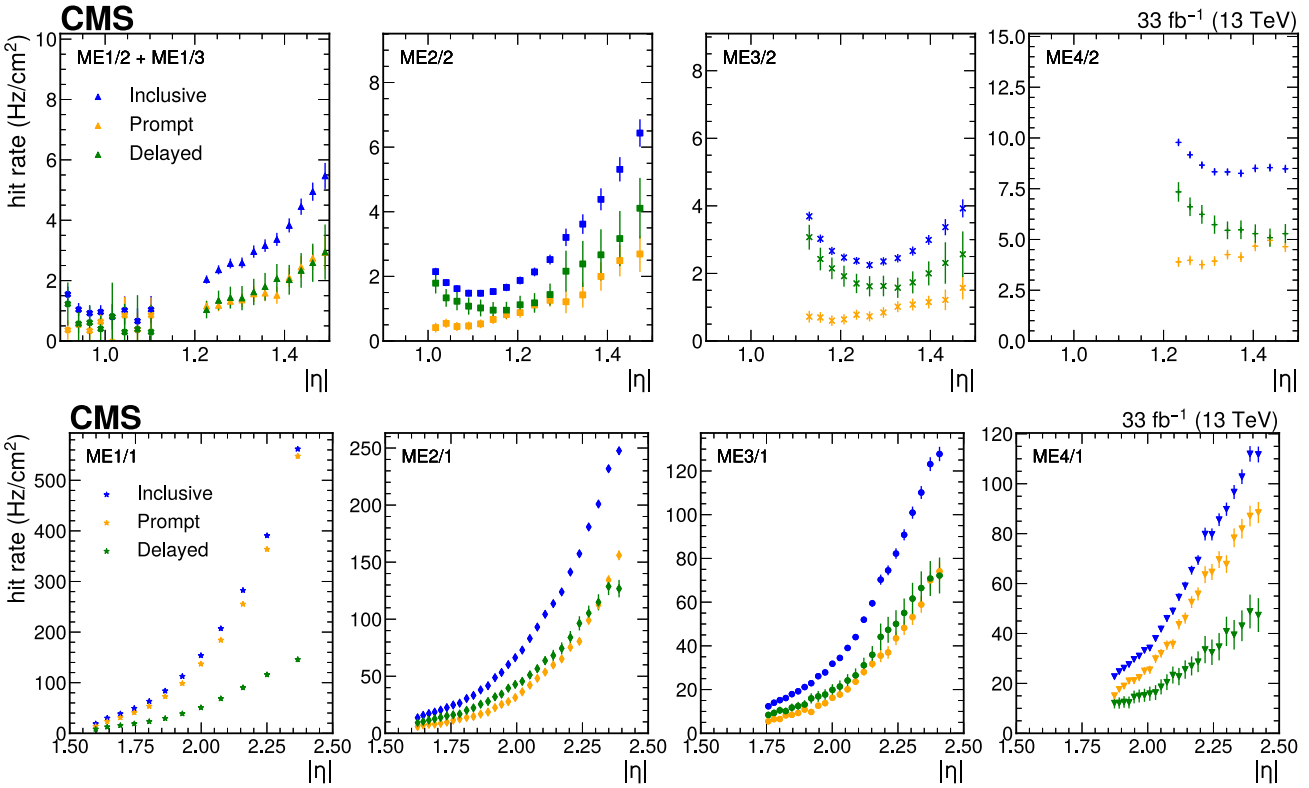

Fig. 30 Hit rate per layer in the CSC chambers of prompt and delayed components, as well as inclusive background at $\mathcal{L} = 10^{34}\,\mathrm{cm}^{-2}\,\mathrm{s}^{-1}$, as a function of pseudorapidity, for the outermost chambers MEx/2,3 (top) and innermost chambers MEx/1 (bottom)

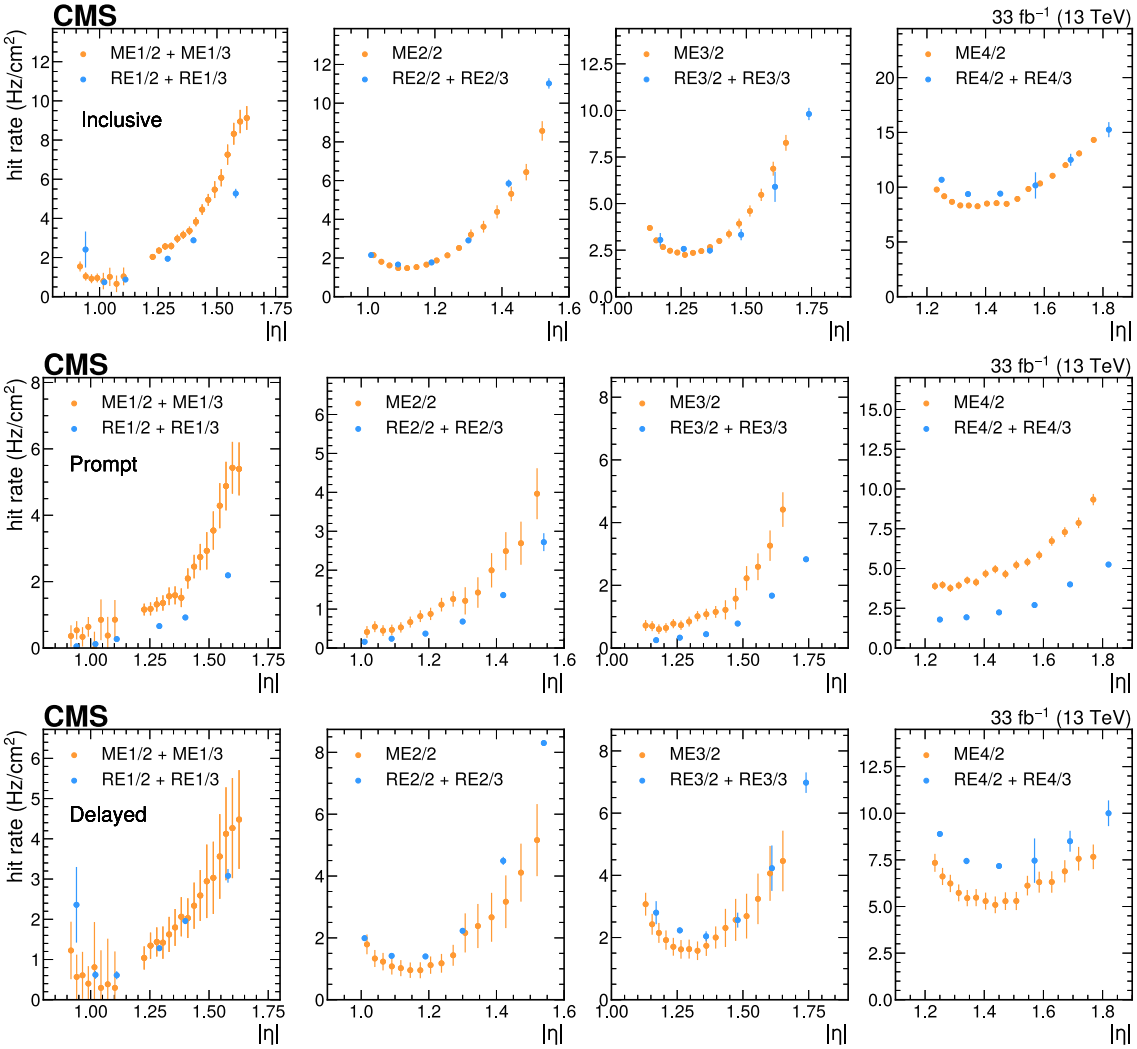

Fig. 31 Comparison of the hit rate per layer in the CSC and RPC system at $\mathcal{L} = 10^{34}\,\mathrm{cm}^{-2}\,\mathrm{s}^{-1}$ as function of the pseudorapidity. Top row: inclusive background averaged over the entire LHC orbit. Middle row: prompt background. Bottom row: delayed background

Funding We congratulate our colleagues in the CERN accelerator departments for the excellent performance of the LHC and thank the technical and administrative staffs at CERN and at other CMS institutes for their contributions to the success of the CMS effort. In addition, we gratefully acknowledge the computing centres and personnel of the Worldwide LHC Computing Grid and other centres for delivering so effectively the computing infrastructure essential to our analyses. Finally, we acknowledge the enduring support for the construction and operation of the LHC, the CMS detector, and the supporting computing infrastructure provided by the following funding agencies: SC (Armenia), BMBWF and FWF (Austria); FNRS and FWO (Belgium); CNPq, CAPES, FAPERJ, FAPERGS, and FAPESP (Brazil); MES and BNSF (Bulgaria); CERN; CAS, MoST, and NSFC (China); MINCIENCIAS (Colombia); MSES and CSF (Croatia); RIF (Cyprus); SENESCYT (Ecuador); MoER, ERC PUT and ERDF (Estonia); Academy of Finland, MEC, and HIP (Finland); CEA and CNRS/IN2P3 (France); BMBF, DFG, and HGF (Germany); GSRI (Greece); NKFIH (Hungary); DAE and DST (India); IPM (Iran); SFI (Ireland); INFN (Italy); MSIP and NRF (Republic of Korea); MES (Latvia); LAS (Lithuania); MOE and UM (Malaysia); BUAP, CINVESTAV, CONACYT, LNS, SEP, and UASLP-FAI (Mexico); MOS (Montenegro); MBIE (New Zealand); PAEC (Pakistan); MES and NSC (Poland); FCT (Portugal); JINR (Dubna); MON, RosAtom, RAS, RFBR, and NRC KI (Russia); MESTD (Serbia); MCIN/AEI and PCTI (Spain); MOSTR (Sri Lanka); Swiss Funding Agencies (Switzerland); MST (Taipei); MHESI and NSTDA (Thailand); TUBITAK and TENMAK (Turkey); NASU (Ukraine); STFC (United Kingdom); DOE and NSF (USA).

Data Availability Statement This manuscript has no associated data or the data will not be deposited. [Authors' comment: Release and preservation of data used by the CMS Collaboration as the basis for publications is guided by the CMS policy as stated in the CMS data preservation, re-use and open access policy [54]. Data cannot be made available for reasons disclosed in the data availability statement].

Code Availability Statement This manuscript has no associated code/software.

Declarations

Conflict of interest The authors declare that they have no conflict of interest.

Funded by SCOAP[3].

A FLUKA model of the CMS experiment and experimental cavern

The FLUKA Run 2 model of CMS experiment is tagged internally as v4.0.1.0 and consists of the CMS detector, the experimental cavern and the interface to the LHC: beampipe, vacuum equipment, collimator and magnets. Figure 32 shows a quarter of the CMS FLUKA model as a vertical slice in the X-Z plane, while Table 7 lists the colour scheme used to indicate some important volumes and materials used in the geometry model.

The CMS detector is implemented as a cylindrically symmetric volume. Barrel muon detectors are modeled as cylinders, consisting of aluminium (DT) or high-pressure laminate (HPL), commonly refered to as *"bakelite"* (RPC) layers with two gas layers in between. Endcap muon detectors are modeled as disks, with CSCs composed of alternating layers of gas and fiberglass laminate (polycarbonate honeycomb sandwiched with a thin FR4 layer) and RPCs as HPL with two gas layers in between. Important features directly visible in Fig. 32 are the big volumes of brass in the barrel (dark magenta) and endcap (teal) calorimeters, the aluminium stabiliser of the Niobium-Tin superconductor of the solenoid (grey) and the magnet flux return yoke in construction steel (olive). Yoke elements in construction steel are finalised with a thin layer of pure iron (yellow) to reduce the effects of activation of the yoke due to trace elements in the steel. Construction elements that are subjected to large stresses are made in stainless steel (green): the solenoid vacuum tank and part of the first endcap disk that mounts the endcap calorimeter (HE) and allows for the insertion of the most forward CSCs in the endcap (ME11). The YE4 shielding disk is implemented as a stainless steel container filled with borated concrete (mint).

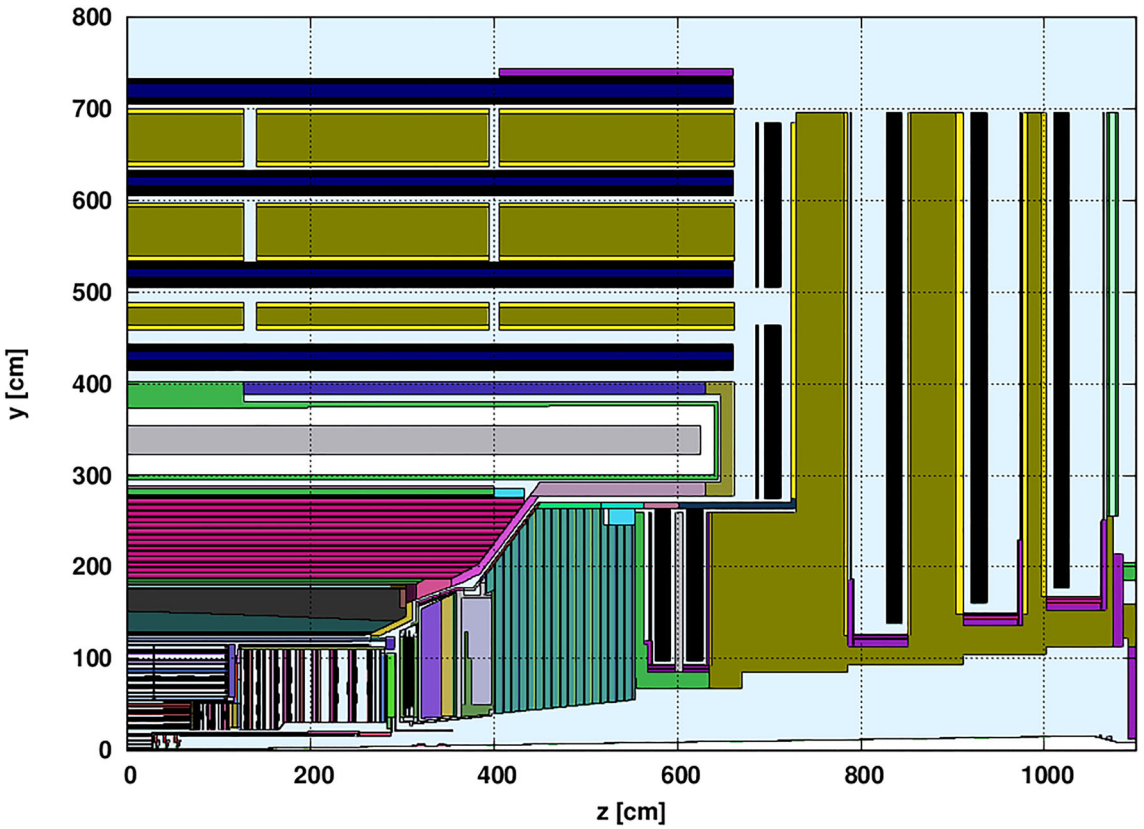

Fig. 32 The CMS FLUKA model (v4.0.1.0) used for simulations of the Run 2 background. A vertical slice in the X–Z plane, showing a quarter of the CMS experiment

Table 7 Color scheme of the CMS Run 2 geometry (v4.0.1.0) used in the FLUKA simulations

Aluminium	Borated Concrete	High-Pressure Laminate (HPL)
Construction Steel	Borated Concrete	Aluminium Honeycomb (DT)
Iron (pure ^{55}Fe)	Borated Concrete YE4	Polycarb Honeycomb (CSC)
Stainless Steel	Borated Polyethylene	DT Gas (Ar:CO2)
Copper	Antimony-doped Lead	CSC Gas (Ar:CO2:CF4)
Brass (HB)	Brass (HE)	Steel and Quartz fibers (HF)
Air	Concrete (Cavern)	Molasse rock

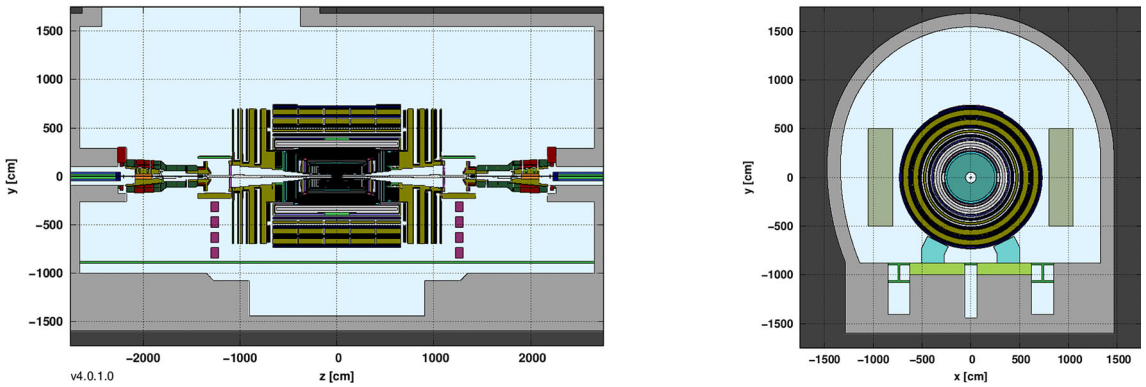

Fig. 33 The CMS FLUKA model (v4.0.1.0) used for simulations of the Run 2 background. Left: A vertical slice at X = 0 through the CMS detector and experimental cavern. The shaft, cavern walls and floor are clearly visible. Right: a vertical slice in the X–Y plane at z = 0. Visible are the electronics racks on each side of the detector and the barrel wheels (YB) feet

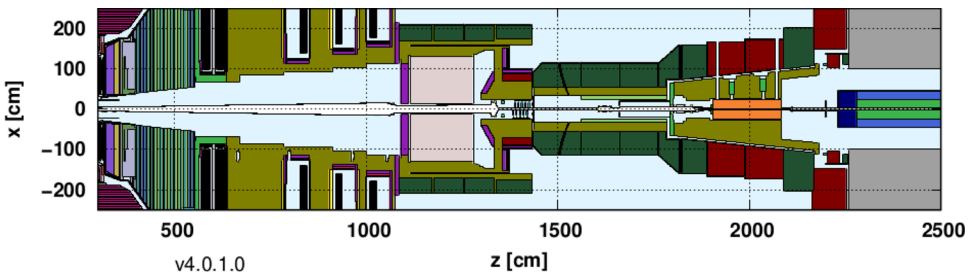

Fig. 34 The CMS FLUKA model used for simulations of the Run 2 background. Detail showing the endcap beampipe, the forward calorimeter, the rotating shielding housing the collimator, and the first LHC quadrupole

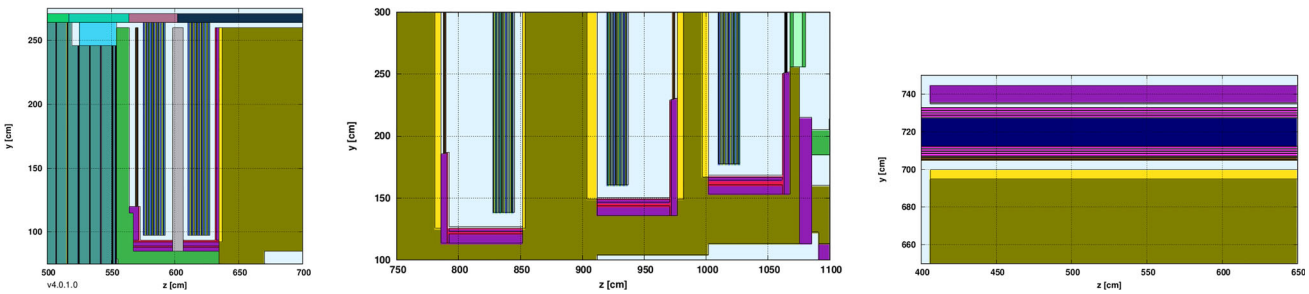

Fig. 35 The CMS FLUKA model used for simulations of the Run 2 background. Detail showing the shielding of the muon chambers: Left: ME11; Middle: ME21, ME31 and ME41; Right: RB4 and MB4 of YB2

Figure 33 illustrates the location of CMS inside the experimental cavern in a vertical slice at X = 0 (left) and transversal slice in the X–Y plane (right). The cavern is implemented according to design drawings, with concrete walls inside the molasse rock, the steel floor, the magnet yoke feet and electronics cabinets in the detector periphery. While the geometry volumes are approximate, the reliability of the simulation is driven by correct implementation of material density, therefore electronics volumes are filled with an appropriate average material.

Figure 34 shows a detail of the forward area, starting with the beampipe that runs under the endcap muon chambers, the forward calorimeter (HF), followed by the rotating shielding that houses the TAS collimator. The material used for the endcap muon shielding is borated polyethylene and antimony doped lead. To prevent neutron albedo (back-scattering) the front of HF has been shielded with borated polyethylene. The forward shielding and the interface between the detector and the machine is implemented in steel and borated concrete. It is modelled with a high level of details, such as cracks, as they are the sources of the radiation leak to the cavern.

Figure 35 (left and middle) shows a detail of the materials and volumes of the endcap muon chambers that are closest to the beampipe: ME1/1 (left) and ME2/1, ME3/1 and ME4/1 (middle). In the left figure one can see the stainless steel element connecting HCAL endcap (HE) to the iron return yoke. The CSC chambers have been shielded by a sandwich of borated polyethylene (magenta) and lead doped with antimony (red). Also visible are the YE4 shielding disk (mint) and the borated polyethylene shielding between muon endcap and HF. Figure 35 (right) shows a detail of the outermost barrel muon detectors (Wheel +2/MB4 and RB4), for which on the top chambers a 10 cm thick borated polyethylene shield (magenta) has been installed. Visible are the 1 cm thick gas layers of the DT chamber (pink) and the aluminium honeycomb structure (navy). Under the DT chamber, the high-pressure laminate (HPL) of the RPC chamber is visible (brown).

References

1. CMS Collaboration, The CMS experiment at the CERN LHC. JINST **3**, S08004 (2008). https://doi.org/10.1088/1748-0221/3/08/S08004
2. CMS Collaboration, The performance of the CMS muon detector in proton-proton collisions at $\sqrt{s} = 7$ TeV at the LHC. JINST **8**(11), P11002 (2013). https://doi.org/10.1088/1748-0221/8/11/P11002
3. CMS Collaboration, Performance of CMS muon reconstruction in pp collision events at $\sqrt{s} = 7$ TeV. JINST **7**(10), P10002 (2012). https://doi.org/10.1088/1748-0221/7/10/P10002
4. CMS Collaboration, Performance of the CMS muon detector and muon reconstruction with proton-proton collisions at $\sqrt{s} =$ 13 TeV. JINST **13**(06), P06015 (2018). https://doi.org/10.1088/1748-0221/13/06/p06015
5. CMS Collaboration, Performance of the reconstruction and identification of high-momentum muons in proton-proton collisions at $\sqrt{s} = 13$ TeV. JINST **15**(02), P02027 (2020). https://doi.org/10.1088/1748-0221/15/02/P02027
6. CMS Collaboration, Performance of the CMS muon trigger system in proton-proton collisions at $\sqrt{s} = 13$ TeV. JINST **16**, P07001 (2021). https://doi.org/10.1088/1748-0221/16/07/P07001
7. CMS Collaboration, Performance of CMS muon reconstruction from proton-proton to heavy ion collisions. 4 (2024). Submitted to JINST, https://doi.org/10.48550/arXiv.2404.17377
8. CMS Collaboration, Development of the CMS detector for the CERN LHC Run 3. JINST **19**, P05064 (2024). https://doi.org/10.1088/1748-0221/19/05/P05064
9. CMS Collaboration, Performance of the CMS Level-1 trigger in proton-proton collisions at $\sqrt{s} = 13$ TeV. JINST **15**, P10017 (2020). https://doi.org/10.1088/1748-0221/15/10/P10017
10. CMS Collaboration, The CMS trigger system. JINST **12**, P01020 (2017). https://doi.org/10.1088/1748-0221/12/01/P01020
11. CMS Collaboration, CMS luminosity measurement for the 2018 data-taking period at $\sqrt{s} = 13$ TeV. Technical Report CMS-PAS-LUM-18-002, Geneva, Switzerland, (2019). http://cds.cern.ch/record/2676164
12. Alan. J. Bell. Beam & Radiation Monitoring for CMS. in *2008 IEEE Nuclear Science Symposium Conference Record*, pages 2322–2325, (2008). https://doi.org/10.1109/NSSMIC.2008.4774822
13. CMS Collaboration, The Phase-2 Upgrade of the CMS Muon Detectors. Technical Report CERN-LHCC-2017-012, CMS-TDR-016, CERN, Geneva, (2017). https://cds.cern.ch/record/2283189
14. CMS Collaboration, Technical proposal for the upgrade of the CMS detector through 2020. Technical Report CERN-LHCC-2011-006, CMS-UG-TP-1, LHCC-P-004, CERN, Geneva, (2011). https://cds.cern.ch/record/1355706
15. O. Brüning et al., LHC design report. Technical Report CERN-2004-003-V-1, Geneva, Switzerland, (2004). https://cds.cern.ch/record/782076
16. J. Wenninger, LHC status and performance. PoS, CHARGED2018:001, (2019). https://doi.org/10.22323/1.339.0001
17. H. Damerau et al. RF manipulations for Higher Brightness LHC-Type Beams. Technical Report CERN-ACC-2013-0210, Geneva, Switzerland, (2013). https://cds.cern.ch/record/1595719
18. R. Steerenberg et al. Operation and Performance of the CERN Large Hadron Collider During Proton Run 2. In Proc. 10th International Particle Accelerator Conference (IPAC'19), pp. 504–507 (2019). https://doi.org/10.18429/JACoW-IPAC2019-MOPMP031
19. M. Giovannozzi, F.F. Van der Veken, Description of the luminosity evolution for the CERN LHC including dynamic aperture effects. Part I: the model. Nucl. Instrum. Meth. A, **905**, 171–179, (2018). [Erratum: Nucl.Instrum.Meth.A 927, 471–471 (2019)], https://doi.org/10.1016/j.nima.2018.07.063
20. M. Giovannozzi, F.F. Van der Veken, Description of the luminosity evolution for the CERN LHC including dynamic aperture effects. Part II: application to Run 1 data. Nucl. Instrum. Meth. A **908**, 1–9 (2018). https://doi.org/10.1016/j.nima.2018.08.019
21. J. Wenninger, Operation and Configuration of the LHC in Run 2. Technical Report CERN-ACC-NOTE-2019-0007, Geneva, Switzerland, (2019). https://cds.cern.ch/record/2668326
22. CMS Collaboration. CMS, the Compact Muon Solenoid: Technical proposal. Technical Report CERN-LHCC-94-38, CERN-LHCC-P-1, Geneva, Switzerland, (1994). https://cds.cern.ch/record/290969
23. CMS Collaboration. The CMS muon project: Technical Design Report. Technical Report CERN-LHCC-97-032, CMS-TDR-3, Geneva, Switzerland, (1997). https://cds.cern.ch/record/343814

24. M. Huhtinen, P.A. Aarnio, Neutron and photon fluxes and shielding alternatives for the cms detector at lhc. Nucl. Instrum. Meth. A **363**, 545–556 (1995). https://doi.org/10.1016/0168-9002(95)00444-0
25. A. Ageev et al., A full-acceptance detector at the LHC (FELIX). J. Phys. G: Nucl. Part. Phys. **28**(6), R117 (2002). https://doi.org/10.1088/0954-3899/28/6/201
26. A.I. Drozhdin, M. Huhtinen, N.V. Mokhov, Accelerator related background in the CMS detector at LHC. Nucl. Instrum. Meth. A **381**, 531–544 (1996). https://doi.org/10.1016/S0168-9002(96)00807-8
27. R. Bruce et al., Sources of machine-induced background in the ATLAS and CMS detectors at the CERN Large Hadron Collider. Nucl. Instrum. Meth. A **729**, 825–840 (2013). https://doi.org/10.1016/j.nima.2013.08.058
28. S.M. Gibson et al. Beam-Gas Background Observations at LHC. In Proc. of International Particle Accelerator Conference (IPAC'17), Copenhagen, Denmark, 14-19 May, 2017, number 8 in International Particle Accelerator Conference, pages 2129–2132, Geneva, Switzerland, (May 2017). JACoW. https://doi.org/10.18429/JACoW-IPAC2017-TUPVA032
29. ATLAS Collaboration, Characterisation and mitigation of beam-induced backgrounds observed in the ATLAS detector during the, proton-proton run. JINST **8**(P07004), 2013 (2011). https://doi.org/10.1088/1748-0221/8/07/P07004
30. ATLAS Collaboration, Beam-induced and cosmic-ray backgrounds observed in the ATLAS detector during the LHC, proton-proton running period. JINST **11**(P05013), 2016 (2012). https://doi.org/10.1088/1748-0221/11/05/P05013
31. R. Bruce et al., Collimation-induced experimental background studies at the CERN Large Hadron Collider. Phys. Rev. Accel. Beams **22**, 021004 (2019). https://doi.org/10.1103/PhysRevAccelBeams.22.021004
32. CMS collaboration. Missing transverse energy performance of the CMS detector. JINST **6**(09), P09001, (2011). https://doi.org/10.1088/1748-0221/6/09/P09001
33. I. Azhgirey et al. Beam-induced Background Simulations for the CMS Experiment at the LHC. In 27th Russian Particle Accelerator Conference, pages 225–227, (2021). https://doi.org/10.18429/JACoW-RuPAC2021-MOPSA55
34. T. Sjostrand, S. Mrenna, P.Z. Skands, PYTHIA 6.4 physics and manual. JHEP **05**, 026 (2006). https://doi.org/10.1088/1126-6708/2006/05/026
35. T. Sjostrand et al., An introduction to PYTHIA 8.2. Comput. Phys. Commun. **191**, 159 (2015). https://doi.org/10.1016/j.cpc.2015.01.024
36. S. Agostinelli et al., GEANT4—a simulation toolkit. Nucl. Instrum. Meth. A **506**, 250–303 (2003). https://doi.org/10.1016/S0168-9002(03)01368-8
37. J. Allison et al., GEANT4 developments and applications. IEEE Trans. Nucl. Sci. **53**, 270–278 (2006). https://doi.org/10.1109/TNS.2006.869826
38. J. Allison et al., Recent developments in GEANT4. Nucl. Instrum. Meth. A **835**, 186–225 (2016). https://doi.org/10.1016/j.nima.2016.06.125
39. S. Banerjee, Validation of physics models of using data from CMS experiment. J. Phys: Conf. Ser. **898**(4), 042005 (2017). https://doi.org/10.1088/1742-6596/898/4/042005
40. A. Dasgupta. Search for Long-Lived Particles Decaying to Displaced Dimuons at 13 TeV and Study of Neutron-Induced Background Hits in the Muon System of the Compact Muon Solenoid. PhD thesis, UCLA, Los Angeles, (2019). CERN-THESIS-2019-129, https://cds.cern.ch/record/2690341
41. C. Schnaible. Search for high-mass dimuon resonances and study of endcap muon system neutron-induced background hits with the Compact Muon Solenoid detector. PhD thesis, UCLA, Los Angeles, (2019). CERN-THESIS-2019-121, https://cds.cern.ch/record/2689948
42. G. Battistoni et al., Overview of the FLUKA code. Ann. Nucl. Energy **82**, 10–18 (2015). https://doi.org/10.1016/j.anucene.2014.11.007
43. C. Ahdida et al., New capabilities of the FLUKA multi-purpose code. Front. Phys. **9**, 788253 (2022). https://doi.org/10.3389/fphy.2021.788253
44. S. Roesler, R. Engel, J. Ranft. The monte carlo event generator DPMJET-III. In International Conference on Advanced Monte Carlo for Radiation Physics, Particle Transport Simulation and Applications (MC 2000), pp. 1033–1038, 12 (2000). https://doi.org/10.1007/978-3-642-18211-2_166
45. CMS Collaboration. Technical Proposal for the Phase-II Upgrade of the CMS Detector. Technical Report CERN-LHCC-2015-010, LHCC-P-008 ; CMS-TDR-15-02, Geneva, Switzerland, (2015). https://cds.cern.ch/record/2020886
46. I. Azhgirey et al. Physical design of the radiation shielding for the CMS experiment at LHC. JACoW, IPAC2021:2246–2248 (2021). https://doi.org/10.18429/JACoW-IPAC2021-TUPAB320
47. I. Azhgirey et al. Benchmarking of the radiation environment simulations for CMS experiment at LHC. JACoW, IPAC 2021:2235–2238, (2021). https://doi.org/10.18429/JACoW-IPAC2021-TUPAB320
48. A. Ferrari, P.R. Sala, A. Fassó, J. Ranft. FLUKA: A multi-particle transport code (program version 2005), volume 10/2005 of CERN Yellow Reports: Monographs. CERN, Geneva, Switzerland, (2005). https://cds.cern.ch/record/898301
49. I. Dawson, editor. Radiation effects in the LHC experiments: Impact on detector performance and operation, volume 1/2021 of CERN Yellow Reports: Monographs. CERN, Geneva, Switzerland, (2021). https://doi.org/10.23731/CYRM-2021-001
50. F. Gasparini et al., Bunch crossing identification at LHC using a mean timer technique. Nucl. Instrum. Meth. A **336**, 91–97 (1993). https://doi.org/10.1016/0168-9002(93)91082-X
51. CMS Collaboration, Transverse-momentum and pseudorapidity distributions of charged hadrons in pp collisions at $\sqrt{s} = 7$ TeV. Phys. Rev. Lett. **105**, 022002 (2010). https://doi.org/10.1103/PhysRevLett.105.022002
52. CMS Collaboration, Measurement of charged particle spectra in minimum-bias events from proton-proton collisions at $\sqrt{s} =$ 13 TeV. Eur. Phys. J. C **78**, 697 (2018). https://doi.org/10.1140/epjc/s10052-018-6144-y
53. CMS Collaboration. CMS TriDAS project: Technical Design Report, Volume 1: The Trigger Systems. Technical Report CERN-LHCC-2000-038, CMS-TDR-6-1, Geneva, Switzerland, (2010). https://cds.cern.ch/record/706847
54. CMS Collaboration. CMS data preservation, re-use and open access policy. CERN Open Data Portal, https://doi.org/10.7483/OPENDATA.CMS.1BNU.8V1W

CMS Muon Group

Vrije Universiteit Brussel, Brussel, Belgium
M. Tytgat[1]

Université Libre de Bruxelles, Bruxelles, Belgium
A. Muhammad, G. De Lentdecker, J. Jaramillo[2], L. Moureaux, L. Pétré[3], Y. Yang

Universiteit Gent, Gent, Belgium
C. Rendón, G. Gokbulut, Y. Hong, A. Samalan

Centro Brasileiro de Pesquisas Fisicas, Rio de Janeiro, Brazil
G. A. Alves, F. Marujo da Silva, E. Alves Coelho

Universidade do Estado do Rio de Janeiro, Rio de Janeiro, Brazil
M. Barroso Ferreira Filho, E. M. Da Costa, D. De Jesus Damiao, B. C. Ferreira, S. Fonseca De Souza, K. Mota Amarilo, H. Nogima, A. Santoro, M. Thiel

Institute for Nuclear Research and Nuclear Energy, Bulgarian Academy of Sciences, Sofia, Bulgaria
A. Aleksandrov, L. Dimitrov, R. Hadjiiska, P. Iaydjiev, M. Misheva, G. Mitev, L. Ratchev, G. Rashevski, M. Shopova, G. Sultanov

University of Sofia, Sofia, Bulgaria
A. Dimitrov, L. Litov, B. Pavlov, P. Petkov, A. Petrov, E. Shumka

Instituto De Alta Investigación, Universidad de Tarapacá, Arica, Chile
S. Keshri, S. Thakur

Institute of High Energy Physics of the Chinese Academy of Sciences, Beijing, China
M. Chen, X. Dong, W. Gong, Q. Hou, C. Jiang, H. Kou, Z.-A. Liu, W. Luo, J. Song, L. Sun, N. Wang, Y. Wang, Z. Wang, C. Zhang, Y. Zhang, H. Zhang, J. Zhao

State Key Laboratory of Nuclear Physics and Technology, Peking University, Beijing, China
A. Agapitos, Y. Ban, A. Levin, Q. Li, S. J. Qian, D. Wang, K. Wang

Sun Yat-Sen University, Guangzhou, China
Z. You

Universidad de Los Andes, Bogota, Colombia
C. Avila, D. A. Barbosa Trujillo, A. Cabrera, C. A. Florez, J. Fraga, J. A. Reyes Vega

Universidad de Antioquia, Medellin, Colombia
F. Ramirez, M. Rodriguez, J. D. Ruiz, N. Vanegas

Academy of Scientific Research and Technology of the Arab Republic of Egypt, Egyptian Network of High Energy Physics, Cairo, Egypt
H. Abdalla[4], A. A. Abdelalim[5,6], Y. Assran[7,8], A. Radi[9,10]

Center for High Energy Physics (CHEP-FU), Fayoum University, El-Fayoum, Egypt
I. Crotty, M. A. Mahmoud

Institut de Physique des 2 Infinis de Lyon, Villeurbanne, France
L. Balleyguier, X. Chen, C. Combaret, G. Galbit, M. Gouzevitch, G. Grenier, I. B. Laktineh, A. Luciol, L. Mirabito, W. Tromeur

Georgian Technical University, Tbilisi, Georgia
I. Bagaturia, I. Lomidze, O. Kemularia, Z. Tsamalaidze[11]

RWTH Aachen University, III. Physikalisches Institut A, Aachen, Germany
U. Böttger, D. Eliseev, T. Hebbeker, K. Hoepfner, M. Merschmeyer, F. Ivone, S. Mukherjee, F. Nowotny, B. Philipps, H. Reithler, A. Sharma, F. Torres Da Silva De Araujo[12], S. Wiedenbeck, S. Zaleski, F. P. Zantis

Karlsruher Institut für Technologie, Karlsruhe, Germany
M. Abbas[13], S. Mallows

Institute of Nuclear Research ATOMKI, Debrecen, Hungary
G. Bencze, N. Beni, J. Molnar, Z. Szillasi, D. Teyssier

Institute of Physics, University of Debrecen, Debrecen, Hungary
B. Ujvari[14], G. Zilizi

Panjab University, Chandigarh, India
J. Babbar, S. Bansal, V. Bhatnagar, S. Chauhan, A. Kaur, H. Kaur, A. Kaur Sahota, S. Kumar, T. Sheokand, J. Singh

University of Delhi, Delhi, India
B. C. Choudhary, A. Kumar, M. Kumar Saini, M. Naimuddin

Saha Institute of Nuclear Physics, Kolkata, India
N. Majumdar, S. Mukhopadhyay, P. Rout

Institute for Research in Fundamental Sciences, Teheran, Iran
V. Amoozegar, B. Boghrati, M. Ebraimi, M. Mohammadi Najafabadi, E. Zareian

INFN Sezione di Bari[a], Università di Bari[b], Politecnico di Bari[c], Bari, Italy
M. Abbrescia[a,b], R. Aly[a,b,5], M. Buonsante[a,b], A. Colaleo[a,b], N. De Filippis[a,c], D. Dell'Olio, G. De Robertis[a], W. Elmetenawee[a,b], N. Ferrara[a,b], M. Franco, G. Iaselli[a,c], N. Lacalamita, F. Licciulli[a], F. Loddo[a], M. Maggi[a], S. Martiradonna, S. Nuzzo[a,b], L. Longo[a], A. Pellecchia[a,b], G. Pugliese[a,c], R. Radogna[a,b], D. Ramos[a], A. Ranieri[a], F. M. Simone[a,b], A. Stamerra[a], D. Troiano[a,b], R. Venditti[a,b], P. Verwilligen[a], A. Zaza[a,b]

INFN Sezione di Bologna[a], Università di Bologna[b], Bologna, Italy
G. Abbiendi[a], C. Baldanza[a], C. Battilana[a,b], A. Benvenuti[a,†], L. Borgonovi[a,15], V. Cafaro[a], F. R. Cavallo[a], A. Crupano[a], M. Cuffiani[a,b], G. M. Dallavalle[a], F. Fabbri[a], A. Fanfani[a,b], D. Fasanella[a], P. Giacomelli[a], V. Giordano[a], C. Guandalini[a], L. Guiducci[a,b], S. Lo Meo[a,16], L. Lunerti[a], S. Marcellini[a], G. Masetti[a], F. L. Navarria[a,b], G. Paggi[a,b], A. Perrotta[a], F. Primavera[a,b], A. M. Rossi[a,b], T. Rovelli[a,b], G. Torromeo[a]

INFN Laboratori Nazionali di Frascati, Frascati, Italy
L. Benussi, S. Bianco, R. Campagnola, M. Caponero, S. Colafranceschi[17], S. Meola[18], L. Passamonti, D. Piccolo, D. Pierluigi, G. Raffone, A. Russo, G. Saviano

INFN Sezione di Napoli[a], Università di Napoli 'Federico II'[b], Napoli, Italy; Università della Basilicata[c], Potenza, Italy; Università G. Marconi[d], Rome, Italy
S. Buontempo[a], A. Cagnotta[a,b], F. Carnevali[a,b], F. Cassese, N. Cavallo[a,c], A. De Iorio[a,b], F. Fabozzi[a,c], A. O. M. Iorio[a,b], L. Lista[a,b,19], P. Paolucci[a,20], G. Passeggio, B. Rossi[a]

INFN Sezione di Padova[a], Università di Padova[b], Padova, Italy; Università di Trento[c], Trento, Italy
L. Barcellan[a], M. Bellato[a], M. Benettoni[a], A. Bergnoli[a], A. Bragagnolo[a,b], R. Carlin[a,b], L. Castellani[a], P. Checchia[a], L. Ciano[a], A. Colombo[a], D. Corti[a], F. Gasparini[a,b], U. Gasparini[a,b], F. Gonella[a], A. Gozzelino[a,21], A. Griggio[a], G. Grosso[a], M. Gulmini[a,21], R. Isocrate[a], E. Lusiani[a], G. Maron[a,21], M. Margoni[a,b], A. T. Meneguzzo[a], M. Migliorini[a,b], L. Modenese[a], F. Montecassiano[a], M. Negrello[a], M. Passaseo[a], J. Pazzini[a,b], L. Ramina[a], M. Rampazzo[a], M. Rebeschini[a], P. Ronchese[a,b], R. Rossin[a,b], F. Simonetto[a,b], M. Toffano[a], N. Toniolo[a,21], A. Triossi[a,b], S. Ventura[a], M. Zanetti[a,b], P. G. Zatti[a], P. Zotto[a,b], A. Zucchetta[a,b]

INFN Sezione di Pavia[a], Università di Pavia[b], Pavia, Italy
S. AbuZeid[a,9], C. Aimè[a,b,22], A. Braghieri[a], S. Calzaferri[a,b], D. Fiorina[a,b,23], S. Gigli, P. Montagna[a,b], C. Riccardi[a,b], P. Salvini[a], I. Vai[a,b], P. Vitulo[a,b]

INFN Sezione di Torino[a], Università di Torino[b], Torino, Italy; Università del Piemonte Orientale[c], Novara, Italy
N. Amapane[a,b], G. Cotto[a], D. Dattola[a], P. De Remigis[a], B. Kiani[a,b], C. Mariotti[a], S. Maselli[a], M. Pelliccioni[a], F. Rotondo[a], A. Staiano[a], D. Trocino[a], G. Umoret[a,b]

Hanyang University, Seoul, Korea
E. Asilar, T. J. Kim, J. A. Merlin

Korea University, Seoul, Korea
S. Choi, B. Hong, K. S. Lee

Kyung Hee University, Department of Physics, Seoul, Korea
J. Goh

Seoul National University, Seoul, Korea
J. Choi, J. Kim, U. Yang, I. Yoon

University of Seoul, Seoul, Korea
W. Jang, J. Heo, D. Kang, Y. Kang, D. Kim, S. Kim, B. Ko, J. S. H. Lee, I. C. Park, I. J. Watson, S. Yang

Sungkyunkwan University, Suwon, Korea
Y. Jeong, Y. Lee, I. Yu

College of Engineering and Technology, American University of the Middle East (AUM), Dasman, Kuwait
G. Alasfour, T. Beyrouthy, Y. Gharbia, Y. Maghrbi, M. Otkur

Centro de Investigacion y de Estudios Avanzados del IPN, Mexico City, Mexico
H. Castilla-Valdez, H. Crotte Ledesma, R. Lopez-Fernandez, A. Sánchez Hernández

Universidad Iberoamericana, Mexico City, Mexico
M. Ramírez García, E. Vazquez, M. A. Shah, N. Zaganidis

Benemerita Universidad Autonoma de Puebla, Puebla, Mexico
I. Pedraza, C. Uribe Estrada

National Centre for Physics, Quaid-I-Azam University, Islamabad, Pakistan
A. Ahmad, W. Ahmed, M. I. Asghar, H. R. Hoorani, S. Muhammad, A. Wajid

Centro de Investigaciones Energéticas Medioambientales y Tecnológicas (CIEMAT), Madrid, Spain
J. Alcaraz Maestre, A. Álvarez Fernández, Cristina F. Fernandez Bedoya, L. C. Blanco Ramos, E. Calvo, C. A. Carrillo Montoya[24], J. M. Cela Ruiz, M. Cepeda, M. Cerrada, N. Colino, S. Cuadrado Calzada, J. Cuchillo Ortega, B. De La Cruz, C. I. de Lara Rodríguez, D. Fernández Del Val, J. P. Fernández Ramos, M. C. Fouz, D. Francia Ferrero, J. García Romero, O. Gonzalez Lopez, S. Goy Lopez, M. I. Josa, J. León Holgado, O. Manzanilla Carretero, I. Martín Martín, J. J. Martínez Morales, E. Martín Viscasillas, D. Moran, Á. Navarro Tobar, R. Paz Herrera, J. C. Puras Sánchez, J. Puerta Pelayo, S. Pulido Ferrero, I. Redondo, D. D. Redondo Ferrero, V. Salto Parra, S. Sánchez Navas, J. Sastre, L. Urda Gómez, J. Vazquez Escobar

Universidad Autónoma de Madrid, Madrid, Spain
J. F. de Trocóniz, F. Frias Garcia-Lago, R. Reyes-Almanza

Universidad de Oviedo, Instituto Universitario de Ciencias y Tecnologías Espaciales de Asturias (ICTEA), Oviedo, Spain
B. Alvarez Gonzalez, J. Cuevas, J. Fernandez Menendez, S. Folgueras, I. Gonzalez Caballero, P. Leguina López, E. Palencia Cortezon, C. Ramón Álvarez, J. Prado Pico, V. Rodríguez Bouza, A. Soto Rodríguez, A. Trapote, C. Vico Villalba

University of Colombo, Colombo, Sri Lanka
B. Kailasapathy[25], K. Malagalage, D. U. J. Sonnadara, D. D. C. Wickramarathna

University of Ruhuna, Department of Physics, Matara, Sri Lanka
W. G. D. Dharmaratna, K. Liyanage, N. Perera, N. Wickramage

CERN, European Organization for Nuclear Research, Geneva, Switzerland
P. Aspell, M. Bianco, D. Bozzato, S. Brachet, A. Conde Garcia, A. Dabrowski, R. De Oliveira, F. Fallavollita[26], P. Kicsiny, A. Sharma

Boston University, Boston, MA, USA
E. Hazen, S. May, A. Peck, K. Salyer, I. Suarez

University of California, Davis, Davis, CA, USA
S. Abbott, J. Bonilla, R. Breedon, H. Cai, P. T. Cox, R. Erbacher, O. Kukral, C. McLean[27], G. Mocellin, M. Mulhearn, B. Regnery[28], M. Tripathi, G. Waegel, Y. Yao[29]

University of California, Los Angeles, CA, USA
J. Carlson, R. Cousins, A. Dasgupta[30], A. Datta, J. Hauser, M. Ignatenko, M. A. Iqbal, C. Lo, D. Saltzberg, C. Schnaible[31], V. Valuev

University of California, Riverside, Riverside, CA, USA
R. Clare, M. Gordon, G. Hanson

University of California, Santa Barbara-Department of Physics, Santa Barbara, CA, USA
N. Amin, J. Bradmiller-Feld, C. Campagnari, T. Danielson, A. Dishaw, A. Dorsett, J. Kim, B. Marsh, H. Mei[32], M. Oshiro, J. Richman, F. Setti, M. F. Sevilla, P. Siddireddy, S. Wang

University of Florida, Gainesville, FL, USA
C. Aruta, V. Barashko, V. Cherepanov, M. Dittrich, A. Korytov, E. Kuznetsova, A. Madorsky, G. Mitselmakher, A. Muthirakalayil Madhu, N. Rawal, N. Terentyev, J. Wang

Florida Institute of Technology, Melbourne, FL, USA
B. Alsufyani, S. Butalla, T. Elkafrawy[9], M. Hohlmann, E. Yanes

Massachusetts Institute of Technology, Cambridge, MA, USA
J. Eysermans

Northeastern University, Boston, MA, USA
E. Barberis, Y. Haddad, Y. Han, G. Madigan, D. M. Morse, V. Nguyen, D. Wood

Northwestern University, Evanston, IL, USA
S. Bhattacharya, J. Bueghly, Z. Chen, K. A. Hahn, Y. Liu, Y. Miao, D. G. Monk, M. H. Schmitt, A. Taliercio, M. Velasco

The Ohio State University, Columbus, OH, USA
B. Bylsma, M. Carrigan, R. De Los Santos, L. S. Durkin, C. Hill

Rice University, Houston, TX, USA
K. Banicz, J. Liu, M. Matveev, B. P. Padley

Texas A&M University, College Station, TX, USA
D. Aebi, M. Ahmad, T. Akhter, A. Bolshov, O. Bouhali[33], R. Eusebi, J. Gilmore, T. Huang, E. Juska, T. Kamon[34], H. Kim, M. Kizlov, S. Malhotra[33], R. Mueller, R. Rabadan, D. Rathjens, A. Safonov

Wayne State University, Detroit, MI, USA
P. E. Karchin

University of Wisconsin-Madison, Madison, WI, USA
A. Aravind, K. Black, I. De Bruyn, P. Everaerts, C. Galloni, M. Herndon, A. Lanaro, R. Loveless, J. Madhusudanan Sreekala, S. Mondal, D. Teague, W. Vetens, A. Warden

Authors affiliated with an institute or an international laboratory covered by a cooperation agreement with CERN, Geneva, Switzerland
I. Azhgirey, V. Borshch, L. Chtchipunov, A. Egorov, G. Gavrilov, V. Golovtcov, M. Ivanov, V. Ivantchenko, Y. Ivanov, V. Karjavine, A. Khodinov, V. Kim, I. A. Kurochkin, P. Levchenko[35], V. Murzin, S. Nasybulin, V. Oreshkin, V. Palichik, V. Perelygin, A. Riabchikova, D. Sosnov, V. Sulimov, L. Uvarov, S. Vavilov, A. Vorobyev[†]

[†] **Deceased**

1: Also at Ghent University, Ghent, Belgium
2: Now at Universidad de Antioquia, Medellin, Colombia
3: Now at University of Wisconsin-Madison, Madison, Wisconsin, USA
4: Also at Cairo University, Gizah, Egypt
5: Also at Helwan University, Cairo, Egypt
6: Now at Zewail City of Science and Technology, Zewail, Egypt
7: Also at Suez University, Suez, Egypt
8: Now at British University in Egypt, Cairo, Egypt
9: Also at Ain Shams University, Cairo, Egypt
10: Also at Sultan Qaboos University, Muscat, Oman
11: Also at an institute or an international laboratory covered by a cooperation agreement with CERN, Geneva, Switzerland
12: Also at The University of the State of Amazonas, Manaus, Brazil
13: Now at Institute for Research in Fundamental Sciences, Teheran, Iran
14: Also at Faculty of Informatics, University of Debrecen, Debrecen, Hungary
15: Now at CERN, European Organization for Nuclear Research, Geneva, Switzerland
16: Also at Italian National Agency for New Technologies, Energy and Sustainable Economic Development, Bologna, Italy
17: Also at Eastern Mennonite University, Harrisonburg, VA, USA
18: Also at Università degli Studi Guglielmo Marconi, Rome, Italy
19: Also at Scuola Superiore Meridionale, Università di Napoli 'Federico II', Naples, Italy
20: Also at CERN, European Organization for Nuclear Research, Geneva, Switzerland
21: Also at Laboratori Nazionali di Legnaro dell'INFN, Legnaro, Italy
22: Now at INFN Sezione di Pisa e Università di Pisa, Pisa, Italy
23: Now at Gran Sasso Science Institute, L'Aquila, Italy
24: Now at Imperial College, London, UK
25: Also at Trincomalee Campus, Eastern University, Nilaveli, Sri Lanka
26: Now at Max Planck Institute for Physics (Werner Heisenberg Institute), Munich, Germany
27: Now at Argonne National Laboratory, Lemont, IL, USA
28: Now at Karlsruhe Institute of Technology, Karlsruhe, Germany
29: Now at Purdue University, West Lafayette, IN, USA
30: Now at Activision, Santa Monica, CA, USA
31: Now at HRL Laboratories, Malibu, CA, USA
32: Now at Tsung-Dao Lee Institute, Shanghai, China
33: Also at Texas A&M University at Qatar, Doha, Qatar
34: Also at Kyungpook National University, Daegu, Korea
35: Also at Northeastern University, Boston, MA, USA